HOST UNIVERSITY: The University of Edinburgh

FACULTY: School of Engineering

DEPARTMENT: Civil and Environmental Engineering

Academic Year 2013-2014

**Assessment of the thermal response
of concrete by inverse modeling**

Davood Zeinali

Promoter(s): Prof. Luke Bisby and Dr. Stephen Welch

Master thesis submitted in the Erasmus Mundus Study Programme

**International Master of Science in Fire Safety Engineering**

# Disclaimer

This thesis is submitted in partial fulfillment of the requirements for the degree of The International Master of Science in Fire Safety Engineering (IMFSE). This thesis has never been submitted for any degree or examination to any other University/program. The author declares that this thesis is original work except where stated. This declaration constitutes an assertion that full and accurate references and citations have been included for all material, directly included and indirectly contributing to the thesis. The author gives permission to make this master thesis available for consultation and to copy parts of this master thesis for personal use. In the case of any other use, the limitations of the copyright have to be respected, in particular with regard to the obligation to state expressly the source when quoting results from this master thesis. The thesis supervisor must be informed when data or results are used.

*April 30 of 2014*

*Read and approved*

# Abstract

This thesis utilizes an innovative inverse modeling technique to associate the thermal behavior of concrete with its basic thermal properties. The practice employs the free open-source Gpyro pyrolysis modeling program to arrive at the necessary thermal properties and reproduce the thermal behavior of concrete. This task has been accomplished using a component of this generalized model which utilizes genetic algorithm to optimize and facilitate the estimation of the material properties from laboratory test results. The experimental results were obtained by assessing the thermal response of several concrete samples in the Cone Calorimeter. Accordingly, samples were exposed to different radiant heat flux levels while their mass loss evolution and their through-thickness temperatures were measured. The inverse modeling practice identified the basic thermal properties successfully, and it was shown that the estimated material properties could be used to predict the thermal behavior at different heat flux levels with reasonable accuracy. It was also discovered that testing the concrete samples in heating regimes based on 'heat flux' rather than 'heating rate' offered a marked advantage. Namely, the obtained mass loss rates followed a distinctive exponential shift in their peaks which could allow decent replication of the cumulative loss of mass for other heating regimes.

# Abstract in Persian (چکیده)

این پایان نامه شیوه‌ی شبیه سازی وارونه‌ی نوینی را به کار می‌گیرد تا به کمک ویژگی‌های دمایی بتن رفتار دمایی آن را پیش بینی کند. شیوه‌ی یاد شده به کمک نرم‌افزار مدل‌سازی پیرولیز رایگان و منبع–باز «جی پایرو» یا «Gpyro»، ویژگی‌های مورد نیاز بتن را هویدا ساخته و دوباره‌سازی رفتار دمایی آن را فراهم می‌سازد. این کار با کمک بخشی از این نرم‌افزار گسترده امکان‌پذیر است که به روش بهینه‌سازی ژنتیکی ویژگی‌های اساسی بتن را از روی نتیجه‌های آزمایشگاهی هویدا می‌سازد. به این هدف، نتیجه‌های آزمایشگاهی مورد نیاز با آزمایش چند نمونه بتن در دستگاه «کالری‌سنج مخروطی» یا «Cone Calorimeter» به دست آورده شد. در این آزمایش‌ها، دمای درون نمونه‌های بتن و جرم آن‌ها در زیر تابش‌های گرمایی متفاوت مورد سنجش قرار گرفت. مدل‌سازی وارونه در پایان توانست ویژگی‌های اساسی یاد شده را با پیروزی هویدا سازد و نشان داده شد که می‌توان رفتار دمایی بتن را با دقت مناسبی به کمک این ویژگی‌های اساسی پیش‌بینی کرد. همچنین پی برده شد که آزمایش بتن در رژیم‌های گرمایی متفاوت بر اساس تغییر اندازه شار یا «فلاکس تابش» به جای «نرخ گرمادهی» برتری برجسته‌ای دارد. این برتری از آنجایی سرچشمه می‌گیرد که بیشینه‌ها یا ماکسیم‌های نرخ‌های تغییر جرم به دست آمده از آزمایش‌های صورت گرفته به کمک روش اول از روند نمایی بسیار خوبی پیروی می‌کنند، و این روند نمایی می‌تواند دوباره‌سازی نرخ‌های تغییر جرم را برای رژیم‌های گرمایی دیگر به آسانی امکان‌پذیر سازد.

# Table of contents

# List of figures and tables

# 1. Introduction

Concrete is the most common building material and the study of its thermal behavior is of significance for various reasons. In construction of energy efficient buildings, for instance, it is vital optimizing the thermal properties of concrete in order to effectively minimize power consumption and to enhance thermal comfort within the buildings (Vangeem *et al.*, 2013; and Wadsö *et al.*, 2012). It is particularly highly essential in design of concrete structures that sufficient functionality is maintained at fire conditions as past fires have already highlighted the vulnerability of concrete structures in such conditions. In fact, building regulations today require different members of the structure to meet specific load-bearing capacity, integrity and insulation requirements under fire conditions for this reason (Approved Document B, UK Building Regulations, 2007). In presence of such important motivations, the modeling of the thermal performance of concrete has been an important research subject during the last two decades as part of an essential means to predict and control the behavior of concrete structures in elevated temperatures. Similarly, it has been critically sought to realize modeling technics which could enable assessment of the thermal behavior of concrete in an efficient and affordable manner.

In view of the above incentives, the main goal of this thesis has been to assess the basic thermal response of several reinforced concrete samples using an innovative inverse modeling technique which involves utilization of a 'genetic algorithm'. As the purpose of any inverse modeling task is to identify modeling parameters which can best reproduce and reflect the observed results, this study aimed to pinpoint near-optimal fundamental parameters such as density, conductivity or permeability that could yield through-thickness temperature and mass loss evolution outcomes best reflecting the results observed at the laboratory tests. The rationale behind this practice is that a direct measurement of each of these unknown properties is cumbersome or not accurately possible, if viable at all. This normally depends on the available technology and its cost. For example properties such as enthalpy are not readily available from basic experiments such as cone calorimetry.

The significance of the followed inverse modeling practice can also be highlighted by acknowledging that most of the models that are proposed and are available in the literature for prediction of the thermal behavior of concrete either rely on generic concrete properties or are based on specific properties from case(s) for which they have been verified; however

concrete is always changing and new admixture materials are developed for concrete rapidly and nonstop. These developments alter the properties of concrete as we know it. As such, concrete cannot be generically treated with certain material properties. Through this work, the fundamental thermal properties of the concrete samples were optimized without including any generic material properties and only the measured density, dimensions and thermal response at several radiative heat fluxes were used to estimate the thermal properties. On the above vantage point, this is highly rewarding; although it must be acknowledged that lower and upper bounds of the problem still need to be defined.

The modeling task was accomplished using a 'pyrolysis model'. A pyrolysis model in general is capable of simulating the gasification or so called 'pyrolysis' of solids in elevated temperatures through assessment of heat transfer and chemical degradation mechanisms; thus effectively a pyrolysis model can predict the thermal response of materials under fire conditions which in turn can empower CFD software such as Fire Dynamic Simulator (developed by NIST in USA) to predict the growth of fire.

Since concrete is an incombustible material, the only gasification relevant to concrete structures at elevated temperatures corresponds to its drying and dehydration which consist of two different phases: respective evaporation of capillary, gel, and interlayer water, and then decomposition of hydration products and release of chemically combined water (Mehta & Monteiro, 2006). As the first phase involves only evaporation, it is merely a physical phenomenon, whereas the second phase involves chemical reactions of decomposition. From a practical standpoint, nevertheless, both these phenomena can be modelled using a pyrolysis model with finite rate chemistry. This study strives to fulfill this promise in effect.

The pyrolysis model that was used in this work for accomplishing the task of modeling is 'Gpyro', a generalized pyrolysis model that can be used for simulating the gasification of a variety of solids. The model is 'generalized' in the sense that it can be set to be used for different problems, including simulations of porous reactive or nonreactive, charring or noncharring, as well as intumescent or non-intumescent solids in different heating environments. Problems can similarly be outlined in 0D to 3D, or they may comprise any number of heterogeneous or homogenous reactions, each of which may follow a different kinetic model that can be optimized separately. Another important advantage that implementation of this pyrolysis model possesses in this work is that it encompasses an integrated and similarly 'generalized' property estimation component. That is, if results from

laboratory tests such as Thermo Gravimetric Analysis (TGA) or flammability tests from the Cone Calorimeter are available, the thermal properties of the material and the involved kinetics can be estimated through solving an inverse problem using this component of the model at a very low cost. For instance, this model has been used to determine the kinetics of the smoldering combustion of polyurethane foam through TGA experiments in less than 10 hours on a 3.0 GHz Pentium system of 2004 (Rein *et al*., 2006). Now, in 2014, that is workable in less than one hour on a typical quad-core laptop.

A precise outline of the scope of this work is provided in the following section. The next sections will also expand upon the literature around the behavior of concrete in elevated temperatures as well as the previous modeling works in this area. A short review will also be provided over Gpyro and particularly how its implementation of a genetic algorithm proved invaluable in this work.

# 1.1. Scope and limitations

This inverse modeling work strives to reflect the basic thermal response of concrete in accordance with the modeling characteristics summarized in Table 1[1]. The modeling goal has been to reproduce the thermal response in terms of through-thickness temperature evolution as well as mass loss in a simple and affordable manner.

This work could not provide insights into prediction of the evolution of complex phenomena such as spalling or cracking which are needed for reliable assessment of the behavior of concrete structures in elevated temperatures. Prediction of these phenomena requires more complex mathematical models that are not (yet) present in Gpyro, namely comprehensive consideration of the mutual interactions and couplings among the mechanical, thermal, hygral as well as degradation processes (Gawin *et al*., 2011). The scope of this study is therefore limited to the basic response of concrete at elevated temperatures and is useful only when the abovementioned complex phenomena are not sources of concern, e.g. in energy efficient designs, in modeling of basic isothermal drying, or in cases where it is needed to optimize the thermal properties of concrete for specific heating regimes.

---

[1] Orange texts in the electronic format of this document are links to other pages. It is similarly possible to get back and forth to previous points by pressing 'Alt key + left or right arrow key' as many times as desired.

Along this work, the Gpyro software and its functionality have been gradually refined in cooperation with its maker; however there still remain some unresolved issues that have inhibited perfect realization of all the capabilities of Gpyro in this work, e.g. problem with simulation of condensation (see Appendix A.1 for a list of the persisting as well as resolved issues). Taking into account the partial realization of the capabilities of Gpyro in this study, the work is still flexible for further improvements as these issues are resolved in the future. Correspondingly, a summary of what further modeling or experimental considerations can supplement a similar work in the future has been presented in the conclusions section.

**Table 1.   The main modeling characteristics of this study**

| Feature | | Presence |
|---|---|---|
| General | Gaseous species | air (nitrogen and oxygen) and water vapor |
| | Material phases | vapor (with no critical point) and solid |
| | Geometry | 2D |
| | Properties nonlinearity | - nonlinear thermal variation in the density, the specific heat and the conductivity of concrete<br>- stepwise permeability and pore size change in concrete<br>- nonlinear thermal porosity variation in concrete |
| Thermal | Conduction | yes |
| | Convection | yes |
| | Surface radiation | yes (front face only) |
| | Latent heats | vaporization and dehydration (no condensation) |
| Chemical | Dehydration | yes (simulated with two finite rate reactions, corresponding to the respective decomposition of Calcium Hydroxide and Calcium Silicate Hydroxides) |
| | Tracking of species | yes |
| Hygral | vaporization | yes (simulated within the first dehydration reaction) |
| | condensation | no (needs to be resolved in Gpyro; see Appendix A.1) |
| | Diffusion of gases | yes (water vapor and air) |
| | Moisture migration and clogging | no (the released chemically combined water vaporizes instantly and the corresponding latent heat is considered in the dehydration enthalpy) |
| Mechanical | Temperature induced damages | no |
| | Load induced damages | no |
| | Over-pressure | yes |

# 1.2. About concrete

Concrete is a composite material composed of a filling matter, i.e. coarse granular aggregates, hold together by a binding material, i.e. cement. Thus the aggregates are simply glued together in the hard matrix of the cement that fills the space among them. Accordingly, the main ingredients of concrete are water, cement, aggregates and admixtures (Advanced Concrete Technology, 2011). For instance, Portland cement concrete can be obtained as follows:

Portland cement + water (+ admixtures) $\longrightarrow$ cement paste

+ fine aggregates $\longrightarrow$ mortar

+ coarse aggregates $\longrightarrow$ concrete
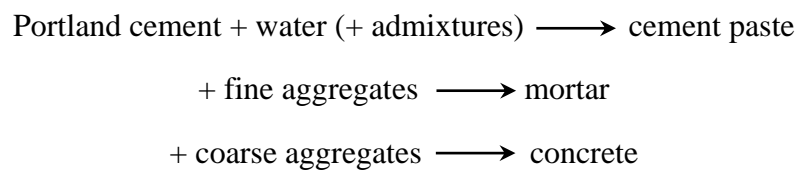
As water reacts with cement, hydrated cement paste is formed. The hydrated cement paste is a compound with various phases, most importantly the Calcium Silicate Hydrate gel (C-S-H phase or the cement gel) which is responsible for strengthening the paste, and also Calcium Hydroxide crystals (C-H phase) which add to the alkalinity of cement (Mehta & Monteiro, 2006). As explained by Mehta & Monteiro, there are different voids present in the hydrated cement paste that are important for various reasons, mainly since they accommodate water or air. Air voids are created either purposefully by entraining small bubbles (size ranging from 10 to 300 μm) or inadvertently by the air entrapped in the mix during casting (with a maximum size of 3 mm). The entrapped air exists near the surface where it is born between concrete mix and its formwork while the entrained air is formed homogeneously (EFCAA, 2006). On top of the air voids, there are two other voids present in the paste, namely capillary voids and gel pores. The gel pores exist in the C-S-H phase and accommodate the gel water which is physically adsorbed. The capillary voids are created by the external water that is neither consumed by the hydration reactions nor adsorbed by the gel pores.

Water within the cement paste can be present in five different forms: *water vapor*; *capillary water*; *gel water*; *interlayer water*; as well as *chemically combined water* (Karhunen, 2013; Chaube *et al.*, 1999; and Schroeder, 1999). These are illustrated in Figure 1 and will be further explained.

As explained by Mehta & Monteiro, *water vapor* occupies the empty or partially filled voids in the cement paste where it exists in equilibrium with the environmental humidity.

*Capillary water* is present in voids larger than about 5 nm. In capillaries larger than 50 nm, the capillary water contained by the void is 'free/unbound water' since it can be dried out easily and without causing any change in volume; whereas in smaller capillaries (5 to 50 nm), the capillary water cannot be completely free as it is contained by capillary action and its removal might cause shrinkage. *Gel water* or 'physically bonded/adsorbed water' is adsorbed as water molecules to the solid surfaces in the C-S-H phase (shown in Figure 1), removal of which results in shrinkage of the hydrated cement paste. *Interlayer water* resides in the extremely small space between the C-S-H sheet layers which can be a space as small as a single (or a few) water molecules (Chaube *et al*., 1999). Removal of this water requires strong drying which results in substantial shrinkage of the C-S-H structure. *Chemically combined water* or 'bound water' is a chemical part of the different hydration products such as C-H crystals, $Ca(OH)_2$, which can only be taken away through decomposition by rigorous heating.
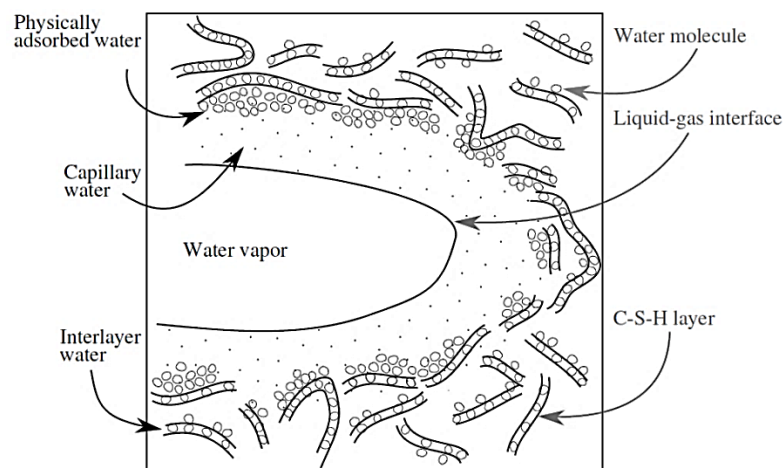


**Figure 1.** **Schematic illustration of how water occupies the voids in the cement paste (based on a model proposed by Feldman & Sereda, 1970; figure from Karhunen, 2013)**

There are numerous types of concrete. These can be classified into four categories based on their density, as shown in Table 2. The main component that defines this density is the type and the density of the incorporated aggregate (Vangeem *et al*., 2013).

It is similarly possible to classify different mixes of concrete based on their compressive strength (Table 3). The most commonly used concretes in construction of buildings, bridges, and similar structures are normal-strength concretes.

**Table 2. Classification of concrete based on density (Li, 2011)**

| Classification | Density of concrete (kg/m³) |
|---|---|
| Ultra-lightweight concrete | < 1200 |
| Lightweight concrete | 1200 – 1800 |
| Normal-weight concrete | ~ 2400 |
| Heavyweight concrete | > 3200 |

**Table 3. Classification of concrete based on compressive strength (Li, 2011)**

| Classification | Application in construction | Compressive Strength (MPa) |
|---|---|---|
| Low-strength concrete | mass concrete structures, subgrades of roads, and partitions | < 20 |
| Moderate-strength concrete | buildings, bridges, and similar structures | 20 – 50 |
| High-strength concrete | tall building columns, bridge towers, and shear walls | 50 – 150 |
| Ultra-high-strength concrete | not widely used in structural constructions | > 150 |

## 1.2.1. Thermal properties

## 1.2.1.1. Density and mass change

The density and the mass of concrete reduce with increasing temperature as concrete loses moisture and dehydrates. The extent to which concrete can retain its mass is dominantly defined by the type of its aggregates (e.g. Kodur & Sultan, 1998; and Lie & Kodur, 1996) particularly beyond 600 ℃ as shown in Figure 2 (Kodur V. , 2014). Beyond 600 ℃, concretes with carbonate aggregates indicate a significant mass loss while concretes made with siliceous aggregates experience minor loss of mass even until 1000 ℃. This abrupt loss of mass in carbonate aggregate concretes has been ascribed to the dissociation of dolomite in carbonate aggregates at around 600 ℃ (Kodur & Harmathy, 2008 ). High-strength concretes exhibit similar mass loss as normal-strength concrete; therefore the strength of concrete is believed not to play a significant role in defining the percentage of mass loss (Kodur V. , 2014).

Figure 3 illustrates how the density of limestone aggregate concrete changes at elevated temperatures. Similar to what was explained above, the density drops at about 600 to 800 ℃, and the amount of the drop is most importantly dependent on the type of the incorporated

aggregates. Similarly, the temperature at which this significant drop occurs appears to be affected by the curing conditions, as described in Figure 3.
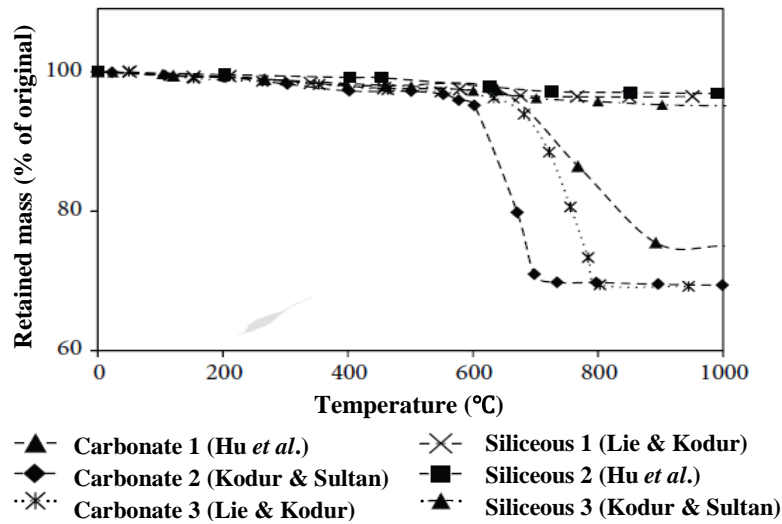


**Figure 2.** **Change in mass of concretes as a function of temperature (Kodur V. , 2014): concretes with the carbonate aggregates indicate a sudden loss of mass beyond 600 ℃ while the concretes with siliceous aggregates have been able to retain their original mass even until 1000 ℃.**



a : Harmathy & Allen, 1973
b : Cured in 20 ℃ and 65 percent RH (Schneider, 1982)
c : Water cured (Schneider, 1982)
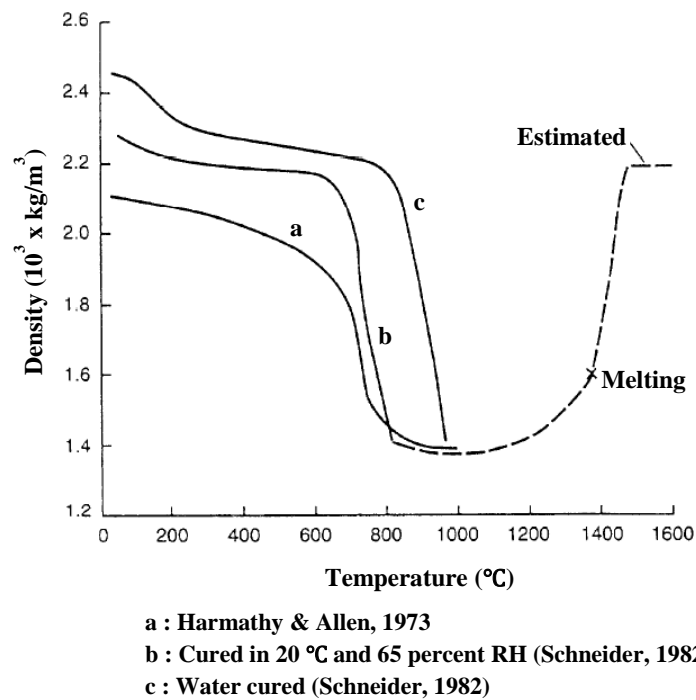
**Figure 3.** **Density of limestone aggregate concrete as a function of temperature (Schneider, 1982; in Bažant & Kaplan, 1996; figure taken from Flynn, 1999)**

## 1.2.1.2. Thermal conductivity

Concrete conducts heat slowly. The thermal conductivity of typical normal strength concrete often ranges between 1.4 and 3.6 W/m.K at room temperatures (Bažant & Kaplan, 1996). For high strength concrete this is between 2.4 and 3.6 W/m.K (Kodur V. , 2014). Generally, the thermal conductivity of concrete is variable upon many factors among which the type of aggregate, porosity and moisture content have been recognized as the key factors (Campbell-Allen & Thorne, 1963; Harmathy, 1970; Marshall, 1972; Khan & Bhattacharjee, 1995; and also Boulder Canyon Project Report, 1940); nevertheless, the thermal conductivity of concrete is primarily determined by the conductivity of its aggregates (Harmathy, 1970). It is also known that cementitious materials tend to indicate different thermal conductivities when assessed by different equipment (Nevile, 1995).

The thermal conductivity of concrete decreases as the moisture content is reduced (Khan, 2002); therefore concrete becomes less conductive as it dries. This translates to a gradual decrease in the thermal conductivity of concrete with temperature as shown in Figure 4 for normal-strength concrete.
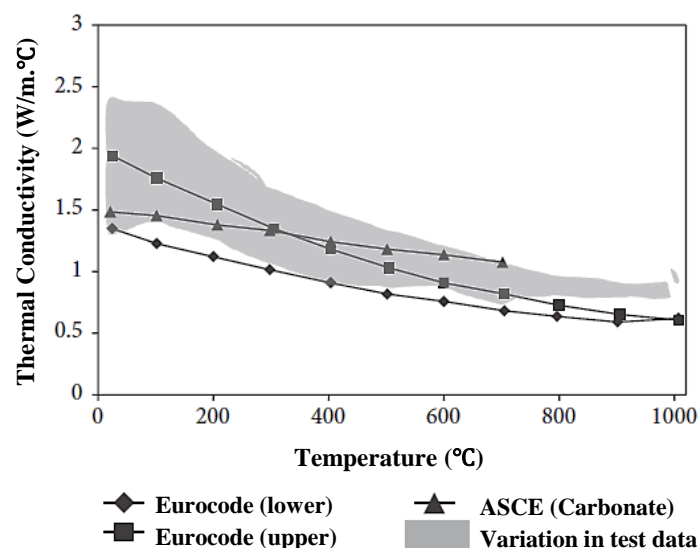


**Figure 4. Thermal conductivity of normal strength concrete as a function of temperature (Kodur V. , 2014): The test data is gathered by Khaliq (Khaliq, 2012) based on experimental data from different sources (Shin *et al.*, 2002; Harmathy & Allen, 1973; Kodur & Sultan, 1998; Harmathy, 1970; Lie & Kodur, 1996; and also Harada *et al.*, 1972) and also empirical relations from different standards (EN 1992-1-2, Eurocode 2, 2004; and also ASCE, Structural Fire Protection, 1992): The shaded area shows variation that existed in the measured test data.**
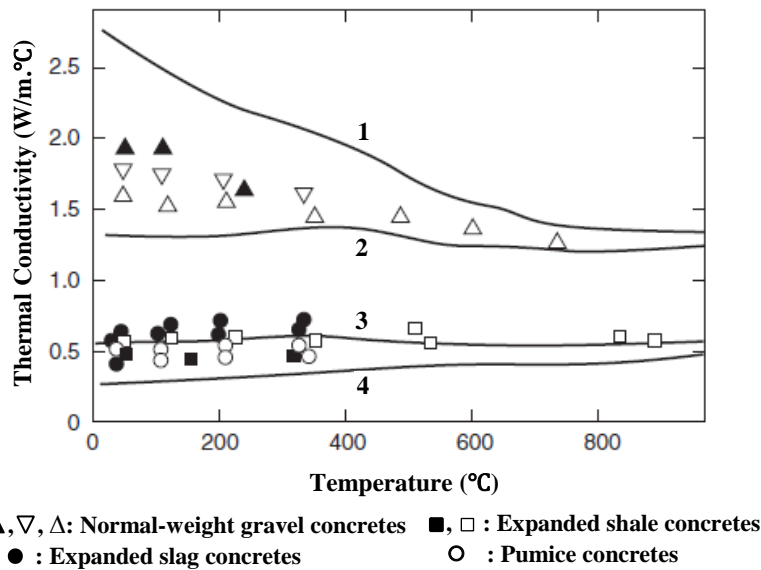
**Figure 5.** Theoretically derived (Harmathy, 1970) "limiting" thermal conductivity cases for normal-weight concretes (solid curves 1 and 2) as well as light-weight concretes (solid curves 3 and 4) along with some experimental data (figure from Kodur & Harmathy, 2008 ).

The solid curves in Figure 5 represent theoretically derived limiting cases among normal-weight as well as light-weight concretes which more or less confirm the upper and lower limits suggested by Figure 4 for the thermal conductivity of normal-weight concrete (try to compare the shaded area shown in Figure 4 with the area enclosed by solid curves 1 and 2 in Figure 5).

## 1.2.1.3. Specific heat

For different aggregate types, the specific heat of concrete varies approximately between 840 J/kg·K and 1800 J/kg·K at room temperature (Kodur V. , 2014) while this increases at higher temperatures as shown in Figure 6. The specific heat at elevated temperatures is highly dependent on the moisture content of concrete and increases significantly with greater ratios of water to cement (Kodur V. , 2014).
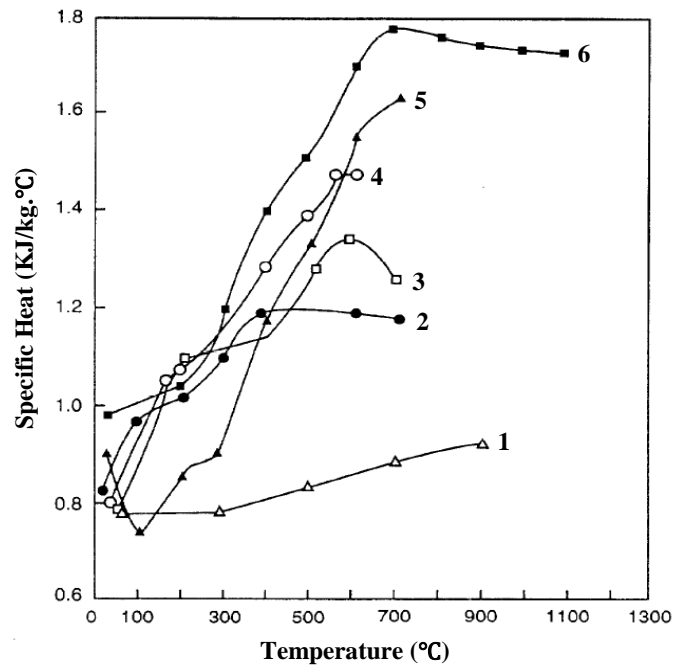
**1 : granite aggregate concrete (Ödeen, 1968)**
**2 : limestone aggregate concrete (Collet & Tavernier, 1976)**
**3 : limestone aggregate concrete (Harmathy & Allen, 1973)**
**4 : siliceous aggregate concrete (Harmathy & Allen, 1973)**
**5 : limestone aggregate concrete (Hildenbrand *et al*., 1978)**
**6 : siliceous aggregate concrete (Hildenbrand *et al*., 1978)**

**Figure 6. Specific heat of various concretes as a function of temperature (Bažant & Kaplan, 1996; figure taken from Flynn, 1999)**

## 1.2.2. Behavior in elevated temperatures

Numerous studies have previously reviewed the behavior of concrete in elevated temperatures (e.g. Mehta & Monteiro, 2006; Bažant & Kaplan, 1996; Khoury, 2000; and Fletcher *et al*., 2007). As temperatures exceed 100 ℃, first and foremost, it is water that vaporizes out of concrete and builds up pressure in the pores. This vaporized water emanates from the capillary water, the gel water, the interlayer water, the chemically combined water and the water vapor existing in the cement paste (refer to the explanations for Figure 1). As explained by Schroeder (Schroeder, 1999), the cement paste initially expands when exposed to elevated temperatures, until the capillary water is removed, whereas further heating causes shrinkage. This shrinkage will continue until all hydrated compounds are decomposed and the chemically combined water is completely removed.

11

The evaporation of capillary, gel, and interlayer water is merely a physical phenomenon whereas the decomposition of hydration products and release of chemically combined water involves chains of chemical reactions that follow particular kinetics (e.g. Peng *et al*., 2001; Zhang & Ye, 2012; and Mikhail *et al*., 1965). Other than water, the entrained and entrapped air, and also the products from the decomposition of the aggregates are able to find their way out of the concrete at elevated temperatures.

The main transformations in concrete at elevated temperatures can be summarized in terms of the following temperature timeline (Fletcher *et al*., 2007; Peng *et al*., 200; Zhang & Ye, 2012; Schroeder, 1999; and Deeny *et al*., 2009):

➢ First, water in concrete starts to boil and vaporize in temperatures approximately between 100 to 140 ℃ while concrete expands. Some of this vapor migrates to the interior of the concrete member where it cools and condenses. This results in an increasingly 'wet' zone, also referred to as 'moisture clog'.

➢ when the free water and the physically adsorbed water finish to vaporize out, concrete starts to shrink and lose its interlayer water at around 300 ℃;

➢ at about 400 to 550 ℃, the calcium hydroxide in the cement begins to dehydrate and release more water vapor, meanwhile at this stage the physical strength of the concrete deteriorates as it continues to shrink;

➢ Quartz-based aggregates experience a major phase change and expand at approximately 550 ℃ due to a mineral transformation that had started earlier around 300 ℃.

➢ the decomposition of C-S-H phase becomes substantial after 600℃ which coincides with a significant loss of compressive strength coming about at the same temperatures; concrete continues to shrink during this period;

➢ carbonate aggregates critically decompose just about 670 ℃ range;

➢ at about 800℃ limestone aggregates begin to decompose;

➢ the C-S-H structure achieves complete decomposition between 900 and 1000 ℃.

The most important consequences of the above physical and chemical transformations at high temperatures can be recognized as loss of compressive strength and also what is called 'spalling' of concrete (Fletcher *et al*., 2007). These are reviewed here briefly.

As summarized by Schroeder (Schroeder, 1999), the durability and strength of concrete in elevated temperatures is defined through many variable parameters including porosity,

aggregate characteristics, and transition zone which are best reviewed by Mehta & Monteiro (Mehta & Monteiro, 2006, Figure 3-13). First and foremost, the strength of concrete is compromised at high temperatures through development of cracks and micro-cracks in the transition zone of cement which reduces elastic stiffness. These (micro-)cracks are developd either by the thermally-induced shrinkage of the hydrated cement paste (Mehta & Monteiro, 2006), by the thermal stresses brought about by differential movements of the hydrated cement paste in contact with aggregates (Dougill, 1961) or possibly due to the rapid decomposition of calcium hydroxide (Lin *et al.*, 1996).

In effect, significant loss of strength is only observed above a critical temperature which largely depends on the type of the incorporated aggregates: sand light-weight concretes reach this temperature at about 650 ℃, carbonate aggregate concretes nearly after 660℃, and siliceous aggregate concretes just about 430 ℃ (Fletcher *et al.*, 2007).

Spalling, as described by Fletcher et al., 2007, is:

> *".. the phenomenon involving explosive ejection of chunks of concrete from the surface of the material, due to the breakdown in surface tensile strength. It is caused by the mechanical forces generated within the element due to strong heating or cooling, i.e. thermal stresses, and/or, by the rapid expansion of moisture within the concrete increasing the pore water pressure within the structure."*

Severe spalling can reduce the concrete cross-section necessary for carrying the imposed loads or remove the concrete cover provided on the reinforcements and expose them to high temperatures, comprising the strength of the structure as a whole either way (Fletcher *et al.*, 2007). Spalling is mostly believed to occur as a result of combined action of pore pressure, compression at the exposed surface, and internal cracking (Deeny *et al.*, 2009), as described in Figure 7. Nevertheless, numerous factors have been recognized to have influence on the spalling of concrete (Majorana *et al.*, 2010) including the moisture content, the permeability, the profile and the rate of heating, the size and the shape of section, the pore pressure, the presence of reinforcements and so forth.
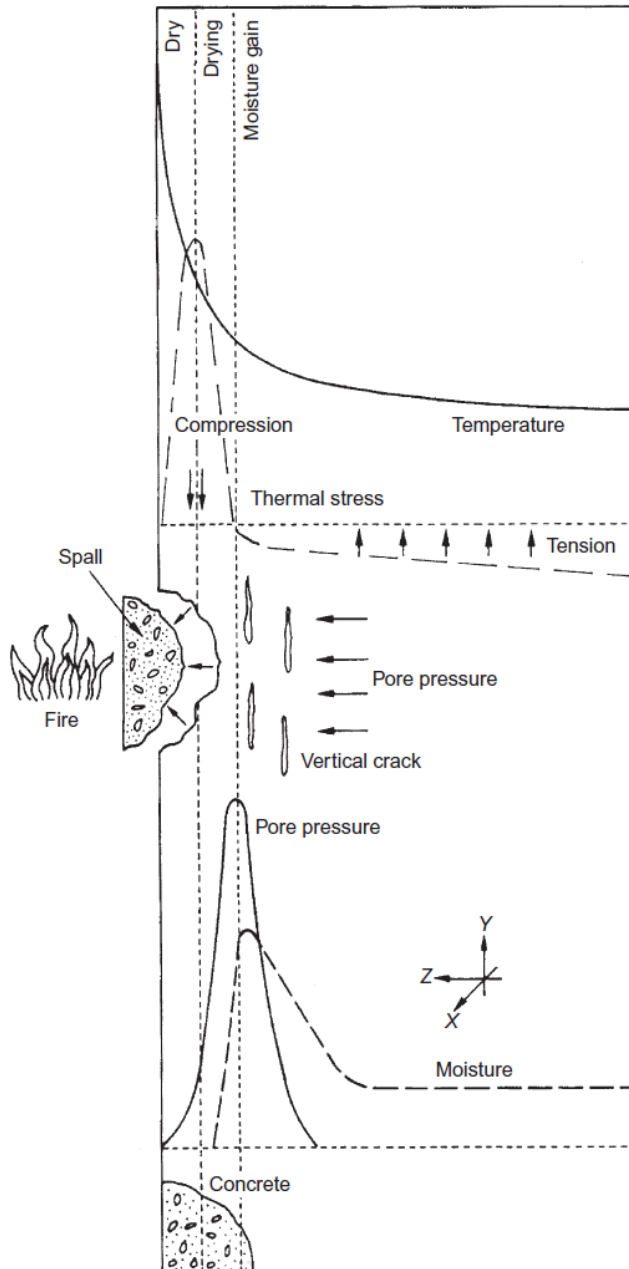
**Figure 7.** Spalling as a result of combined action of pore pressure and thermal stress (Khoury, 2008): a maximum pore pressure is achieved at a distance from the hot surface, namely at the interface between the vapor zone and the zone with moist gain (Ozawa *et al.*, 2012). The depth of this point will depend on the permeability. If the pressure is greater than the local tensile strength of the concrete, it will encourage pore-pressure spalling. On the other hand, thermal stress spalling develops as a result of the opposing compressive and tensile stresses, near the heated surface and in the cooler interior regions, respectively (Khoury, 2008).

## 1.2.3. State of the art in modeling

Commercial finite-element packages are available and have been used by different authors for assessment of the thermal response of concrete structures at elevated temperatures (e.g. Hawileha *et al.*, 2009; and Lim *et al.*, 2004). These are normally multipurpose software such as ANSYS (developed by ANSYS, Inc. in USA) or they are software exclusively for structures in fire such as SAFIR (developed at the University of Liege in Belgium: Franssen, 2005). However, these are typically considered unsophisticated as they over-simplify the

modeling problem; they particularly simplify thermal effects by assuming that material properties such as strength or stiffness are solely functions of temperature, which does not account for the irreversible changes these material properties may undergo (Fletcher *et al*., 2007). For instance SAFIR does not model moisture migration; therefore the effects of moisture on the temperature evolution have to be compensated by choosing appropriate thermal properties instead (Lim *et al*., 2004).

Apart from commercial codes, various numerical models with different levels of sophistication have been developed for simulation of concrete behavior at high temperatures; nevertheless, only a few models have been presented so far that catch the fully coupled nature of the complex phenomena involved, namely models by Gawin *et al*., 2011; Davie *et al*., 2010; Chung *et al*., 2006; Tenchev & Purnell, 2005; Khoury *et al*., 2002; Grasberger & Meschke, 2000; and Ulm *et al*., 1999. Other less sophisticated models have also been presented by Dwaikat & Kodur, 2009; Tenchev & Purkiss, 2001; Stabler, 2000; or Gawin *et al*., 1999;

Gawin *et al*., 2011 (part 1 and 2), investigated the importance of the main modeling features and parameters that influence the evolution of complex phenomena in concrete at high temperatures. They concluded that neglecting the vapor diffusion and the effect of damage on the material permeability caused the most serious numerical problems. Similarly, it has been generally recognized that in order to assess the thermal behavior of concrete members reliably, it is essential to take into account the mutual interactions and couplings among the thermal, hygral and degradation processes (Fletcher *et al*., 2007). Other important factors have also been identified as: the evolution of temperature along with the moisture content and gas pressure, the porous and multiphase nature of concrete, chemical and phase transformations, behavior of moisture above the critical temperature of water, material nonlinearities especially those due to temperature changes or material cracking and thermo-chemical degradation (Gawin *et al*., 2011).

Unsurprisingly, a solution that can embrace all the above mechanisms is too expensive and therefore very challenging in applications for large structures (Fletcher *et al*., 2007); however it must also be noted that an optimum level exists for inclusion of more complexity in a model. As Bal signifies (Bal, 2012), the implicit assumption that 'more complexity means more accuracy' has widely overshadowed the fact that 'more complexity brings in more uncertainty'. Since all the uncertainty brought in by new input parameters ultimately amass in the outcomes of the model, the overall accuracy of the model is always limited by the balance

between the parameters' uncertainty and the improvements which are gained by the added complexity. Hence, Bal concludes that sensitivity analyses must be carried out and verified experimentally prior to adding any higher levels of complexity to a model.

# 1.3. About Gpyro

Gpyro is a generalized pyrolysis model developed by Lautenberger at the University of California, Berkeley in 2007 (Lautenberger, 2007, *PhD Thesis*). Gpyro can be used for simulating the gasification of solids experiencing a particular heating environment. The model is 'generalized' in the sense that it can be set to be used for different problems, e.g. the solids can be reactive or nonreactive, single or multilayer, intumescent or non-intumescent; the problems can similarly be outlined in 0D to 3D or involve different kinetics for instance. Another important feature of this pyrolysis model is that it encompasses an integrated and similarly 'generalized' property estimation component. Therefore, if results from laboratory tests such as Thermo Gravimetric Analysis (TGA) or flammability tests from the Cone Calorimeter or the Fire Propagation Apparatus (FPA) are available, the thermal properties of the material as well as the involved reaction kinetics can be estimated through solving an inverse problem using this component of the model at a very low cost. For instance, the kinetics of the smoldering combustion of polyurethane foam have been previously established through TGA experiments with this model in less than 10 hours on a 3.0 GHz Pentium system of 2004 (Rein *et al*., 2006). Now, in 2014, that is workable in less than one hour on a typical quad-core laptop.

Separate conservation equations are solved at the heart of Gpyro for gaseous and condensed phase mass, species, and energy as well as gas phase momentum (Lautenberger, 2009, *Gpyro Technical Reference*). The user may specify any number of gas phase or condensed phase species, different thermal properties, or any number of heterogeneous (solid-gas) or homogeneous (gas-gas) reactions.

## 1.3.1. How it works

The user is free to include as much complexity in a simulation as they deem necessary. In its simplest form, Gpyro may comprise a 0D transient heat conduction simulation for a fixed-property nonreactive single cell solid being heated at a linear heating rate (i.e. for a

TGA/DSC experiment with an inert material for instance); whereas in its most sophisticated form, Gpyro can embrace multi-dimensional conjugate heat transfer, fluid flow/pressure evolution, gaseous species diffusion/convection in a multi-component, heterogeneous, reacting porous medium with temperature-dependent thermophysical properties, in-depth radiation absorption, radiation heat transfer across pores, multi-step heterogeneous decomposition kinetics of arbitrary order, and multi-step homogeneous gas-phase reactions (Lautenberger, 2009, *Gpyro Users' Guide*). Therefore, physical phenomena are available as options that can be enabled or disabled. Much similar to the modeler, the material property estimation routines require the user to specify parameter ranges as well as other variables/flags that define how the optimization should be conducted.

Technical explanations about the submodels implemented in Gpyro along with how they function, are available generally in the users' guide (Lautenberger, 2009, *Gpyro Users' Guide*) or more thoroughly in the technical guide (Lautenberger, 2009, *Gpyro Technical Reference*); however these guides need substantial updates as the model has evolved dramatically since 2009. In fact, major parts of this inverse modeling work have been made possible through improving or amending the functioning of the software in cooperation with Lautenberger (see Appendix A.1 for a list of the issues which were resolved and the ones still persisting).

In simple terms, the standalone Gpyro simulations require only a single text input file (ASCII) with the extension '.data'. This file will have to contain the thermal properties, the reaction kinetics, the boundary conditions, and so forth. The property estimation program requires a similar file, but only named 'gpyro.data', in addition to the supplementary Microsoft Excel input files that contain the experimental data needed for optimization.

The input files can be generated using a simple user interface (or front end) which is implemented through a Microsoft Excel spreadsheet. By making use of a Visual Basic macro which is embedded in the spreadsheet, the user can automatically generate ASCII input files needed for simulations with Gpyro (via the keystroke 'Ctrl + g'). The spreadsheet is therefore simply a template that can be copied from any previous simulation and be used to specify the thermal properties, the reaction kinetics, etc. without being concerned with the finished syntax of the final ASCII input files read in by Gpyro.

The ASCII input files which are produced by the spreadsheet-based front end simply contain several Namelist groups which can be found in Table 4. As the codes in the input files follow a particular syntax (based on C++), if the user knows the syntax, they can edit the ASCII input files directly and circumvent the spreadsheet-based front end altogether.

**Table 4. Gpyro Namelist groups as in the ASCII and the spreadsheet-based front end input files (Lautenberger, 2009, *Gpyro Users' Guide*)[*1]**

| Namelist group in the ASCII input files | Corresponding worksheet name | Descriptions |
|---|---|---|
| &GPYRO_GENERAL | General | Main parameters/flags defining the desired complexity/cost of the simulation |
| &GPYRO_OUTPUT | Output | Outputs definition in terms of the type, the frequency, the number and the location of dumps |
| &GPYRO_SPROPS | SProps | Definition of the thermophysical properties of each condensed phase (solid) such as conductivity, density and permeability. |
| &GPYRO_RXNS | Rxns | Parameters defining the heterogeneous reactions occurring to the condensed phases such as kinetic models, activation energies, enthalpies and orders of the reactions. |
| &GPYRO_GPROPS | GProps | Gaseous species and their properties, including their molecular weight and specific heat as well as their corresponding Lennard–Jones parameters. |
| &GPYRO_GYIELDS | GYields | The reaction coefficients for gaseous yields and reactants in the heterogeneous reactions. |
| &GPYRO_HGRXNS | HgRxns | Parameters defining the homogeneous reactions occurring to the gaseous species, such as activation energies and enthalpies. |
| &GPYRO_HGYIELDS | HgYields | The reaction coefficients for gaseous yields and reactants in the homogeneous reactions. |
| &GPYRO_IC | IC | Definition of initial conditions for each solid layer in different cases[*2] in terms of fractions of the condensed phases or the gaseous species, and also their temperatures and pressures. |
| &GPYRO_GEOM | Geom | Design of the overall geometry for each case (1D to 3D), width of every layer, number of the cells in different directions (x, y and z), as well as designation of the solid faces to which the boundary conditions are applied. |
| &GPYRO_ALLBC | BC | Set up of boundary conditions for the conservation equations that are solved[*3], i.e. solid energy, gas momentum, gas energy, and gas species. |
| &GPYRO_CASES | Cases | Designation of cases to run, and whether they are 0D. |
| &GA_GENINPUT | GA_GenInput | Parameters adjusting the type and the cost of optimization. |
| &GA_PHI | GA_Phi | Characterization of the variables that are desired to be optimized |
| &GA_VARS | GA_Vars | Specification of the range of the variables that are going to be optimized as well as their association with each other. |

[*1] The Namelist structure provided above is a representation of the current status of the model (April, 2014) and does not agree with the user's guide. Substantial updates are due for the users' guide as the model has evolved dramatically since 2009; therefore the structure of the worksheets in the new spreadsheet-based front end is greatly different from its initial implementation as in the users' guide.

[*2] In a single run, Gpyro can simulate several cases at the same time. For instance, a multilayer sample can be exposed to different heating environments and periods of time with different initial conditions for each layer.

[*3] The user has to specify in the 'General' worksheet, which conservation equations they need to be solved; that is to say, not all the equations or boundary conditions are going to be used. If the user is not interested in the pressure distribution inside the sample, for instance, they can choose not to solve for the gas momentum conservation equations; instead, Gpyro will use gaseous mass conservation to estimate the local convective mass flux (Lautenberger, 2009, *Gpyro Technical Reference*).

# 1.3.1.1. Optimization

There are currently three optimization algorithms available in Gpyro (as of version 0.798), namely 'genetic algorithm', 'shuffled complex evolution', and 'stochastic hill climber'. The latter two have been added lately and would naturally need much further improvements whereas the implementation of genetic algorithm has been evolving since Gpyro was born in 2007 and is greatly robust.

The inverse modeling optimization practice in this work involves utilization of the genetic algorithm to pinpoint the ranges as well as the associations of the key thermal parameters of the concrete samples which were experimented at the laboratory. Therefore, it deems rather necessary describing in short how the genetic algorithm functions and how it is helpful in this work.

As described by Rein *et al*. (Rein *et al*., 2006), a genetic algorithm is an investigative search scheme that mimics the principles of biological adaptation based upon the mechanisms of the Darwinian survival-of-the-fittest theory (Goldberg, 1989; and Foster, 2001). The procedure of a genetic algorithm begins with randomly generating several sets of values for the variables or *genes* that are desired to be optimized (such as conductivity or permeability). By applying each set of genes, a candidate solution is determined for a certain experimental quantity (e.g. the surface temperature of the material). A candidate solution is similar to an *individual*, and all the candidate solutions together can be thought of as a *population*. As the idea of Darwin's theory is that a population will always evolve in the nature, the individuals of this initial population need to be selected cautiously before they can breed new descendants to the upcoming population. Every upcoming population will be a *generation*, and what defines whether an individual can be selected to reproduce for the next generation is how well it matches the actual solution or the experimental result (e.g. surface temperature obtained from Cone Calorimetry). In other words, each individual is examined for its *fitness* to the experimental result. If an individual provides a solution that fits well with the actual solution, that individual will likely evolve to the next generation. This means that each time, only the best individuals of the population will be selected to reproduce for the next generation. Once the best individuals are selected, they form parents and produce new genes through a stochastic mutation mechanism to make up the next generation with new individuals. As each generation is evolved from the best individuals, the overall fitness from

generation to generation increases progressively. When no subsequent improvements occur, the procedure should have converged to the experimental result and be ceased.

The genetic algorithm utilizes stochastic components in the mutations and the selection operations to ensure wide exploration and to prevent becoming trapped. The larger the population size, the more spaces will be explored and the less generations will be needed for convergence. Population sizes between 100 and 500 are typically satisfactory if the ranges of the parameters are well established (Rein *et al*., 2006).

Compared to other classical non-linear optimization schemes such as Monte Carlo system, the genetic algorithm performs very well in high-dimensional problems, resists becoming trapped and is applicable to non-continuous objective-landscapes; however it is heuristic in nature, is not efficient for small problems and may not be the quickest system (Rein *et al*., 2006). Particularly, genetic algorithms can quickly pinpoint the whereabouts of the solution in huge spaces but might take a relatively long time to converge to a fine localized solution.

In optimization of the material properties, the genetic algorithm will yield ideally fitting results only if (Lautenberger, 2009, *Gpyro Technical Refrence*):

➢ the experimental data is sufficiently accurate;
➢ the data contains enough information to establish a unique set of model parameters;
➢ the pyrolysis model represents the underlying physical/chemical processes adequately;
➢ and the specified boundary and initial conditions are accurately representative of the experimental configuration.

Naturally, the final solution from the genetic algorithm is coupled with the used model and the experimental results, meaning that using it in a different model or a different experimental environment may bring about huge uncertainties due to the differences in the underlying methodologies and conditions (Bal, 2012). Similarly as important, the solution is not necessarily the absolute optimal solution, but it simply provides a near–optimal prediction of the experimental data given the constraints of the underlying model. It should be acknowledged, nevertheless, that the results are almost as good as those that would have been obtainable with the optimal solution (Lautenberger, 2009, *Gpyro Technical Refrence*).

It is rather of essence, in regard of the usability of the solutions from the genetic algorithm, to understand that the methodology should not be implemented as an unknown 'black box'. The user must be aware that the solutions obtained through this methodology would be usable and 'meaningful' only if the model represents the underlying physical/chemical processes adequately. Only then, it can be used reliably to predict the behavior of the material in a different heating environment.

Imagine a situation in which there is only a <u>minor</u> combination of parameters absent from a model. Consider that all these absent parameters together, in effect, will change the final solution as if they were a single variable (this may vary nonlinearly or it may simply be a fixed constant). Now by using the genetic algorithm, the user can tune the model and embed the effect of that unknown variable within the current formulation of the model, without the user being concerned with the values of that unknown variable. <u>However</u>, this can only be meaningful and reliable if the fundamental aspects of the problem are truly being described by the current model. If this is not the case, it means that the user has merely been lucky to obtain a good match for a <u>local environment</u>. That is to say, we <u>cannot</u> rely on the model to predict what will happen to the material in a different heating environment if we do not know how correctly the model represents the problem.

The following may portray the required awareness in the best way (Black box theory, 2014):

> *"Considering a black box that could not be opened to "look inside" and see how it worked, all that would be possible would be to guess how it worked based on what happened when something was done to it (input), and what occurred as a result of that (output). If after putting an orange in on one side, an orange fell out the other, it would be possible to make educated guesses or hypotheses on what was happening inside the black box. It could be filled with oranges; it could have a conveyor belt to move the orange from one side to the other; it could even go through an alternate universe. Without being able to investigate the workings of the box, ultimately all we can do is guess.*
>
> *However, occasionally strange occurrences will take place that change our understanding of the black box. Consider putting in an orange in and having a guava pop out. Now our "filled with oranges" and "conveyor belt" theories no longer work, and we may have to change our educated guess as to how the black box works."*

# 2. Methodology

The experimental as well as the modeling methodologies of this work are explained in this section. It is firstly described how two-way reinforced concrete samples were tested in the Cone Calorimeter to investigate their thermal response and then it is explained how a 2D modeling approach was implemented in Gpyro to perform the inverse modeling practice so that it could ensure proper reflection of the thermal behavior.

## 2.1. Experiments

Two-way reinforced concrete samples of the dimensions 100mm x 100mm x 25mm were tested in the Cone Calorimeter. These samples were cut from a reinforced normal-strength concrete slab which had been casted one year and 3 months earlier (454 days old). The concrete mix was an RC40/50 designated carbonate aggregate concrete with an average bulk density of 2250 kg/m$^3$ from Tarmac with fine aggregates of maximum size of 10mm. The average cylinder compressive strength at the time of experiments was 51 MPa and thus only slightly exceeded the designated strength. The steel reinforcement bars in the slab were of 4mm diameter size separated by 50mm spans; although after the cutting process the positioning of the bars inside the samples was not precisely the same for all the samples. Figure 8 shows one of the samples as well as the positioning of the bars inside it.

A total of 20 samples were exposed to different radiative heat flux levels in the Cone Calorimeter in order to assess their thermal response. An additional sample was also kept in oven at 105°C until its weight became constant and the amount of free water was estimated[2]. Figure 9 displays the set-up of the 20 experiments which were performed in the cone.

The radiative heat flux levels to which the samples were exposed are summarized in Table 5. The samples were exposed to heat fluxes as low as 10 kW/m$^2$ and as high as 85 kW/m$^2$. The heating was initiated in each experiment only when the heat flux had become stable at the desired level. Figure 10 shows an instance of how the heat flux was allowed to become steady before an experiment was carried out.

---

[2] This is the typical procedure for the estimation of free water inside concrete samples (Bordallo *et al*., 2006).
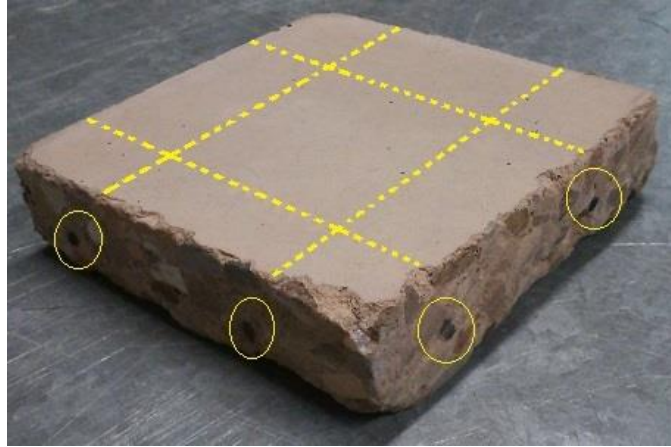
**Figure 8. One of the two-way reinforced concrete samples (100mm x 100mm x 25mm): The originating concrete was RC40/50 designated carbonate aggregate concrete with an average bulk density of 2250 kg/m$^3$ and fine aggregates of maximum size of 10 mm. The circles and the dotted lines display the approximate positioning of the steel reinforcement bars.**
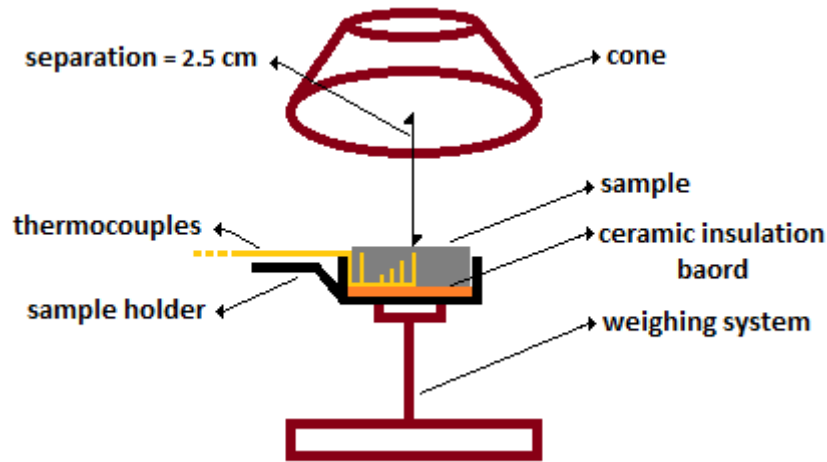


**Figure 9. Set-up of the experiments in the Cone Calorimeter: thermocouples were drilled from the back side of the samples at different points (at the center, near the sides or at the corner) and different depths (typically 7mm, 10mm, 15mm and 19mm). These were present only in the experiments with temperature measurement. Ceramic insulation was also put below the sample to prevent heat loss from its back side.**

<div align="center">

**Table 5. Experimental plan and the naming of the tests**

</div>

| Measurement in the test | Radiative heat flux level | | | | |
|---|---|---|---|---|---|
| | **10 kW/m$^2$** | **30 kW/m$^2$** | **50 kW/m$^2$** | **70 kW/m$^2$** | **85 kW/m$^2$** |
| **Mass loss rate measurement - primary (MLR)** | MLR@10-1 | MLR@30-1 | MLR@50-1 | MLR@70-1 | MLR@85-1 |
| **Mass loss rate measurement - replicate (MLR)** | MLR@10-2 | MLR@30-2 | MLR@50-2 | MLR@70-2 | MLR@85-2 |
| **Temperature measurement - primary (TMP)** | TMP@10-1 | TMP@30-1 | TMP@50-1 | TMP@70-1 | TMP@85-1 |
| **Temperature measurement - replicate (TMP)** | TMP@10-2 | TMP@30-2 | TMP@50-2 | TMP@70-2 | TMP@85-2 |
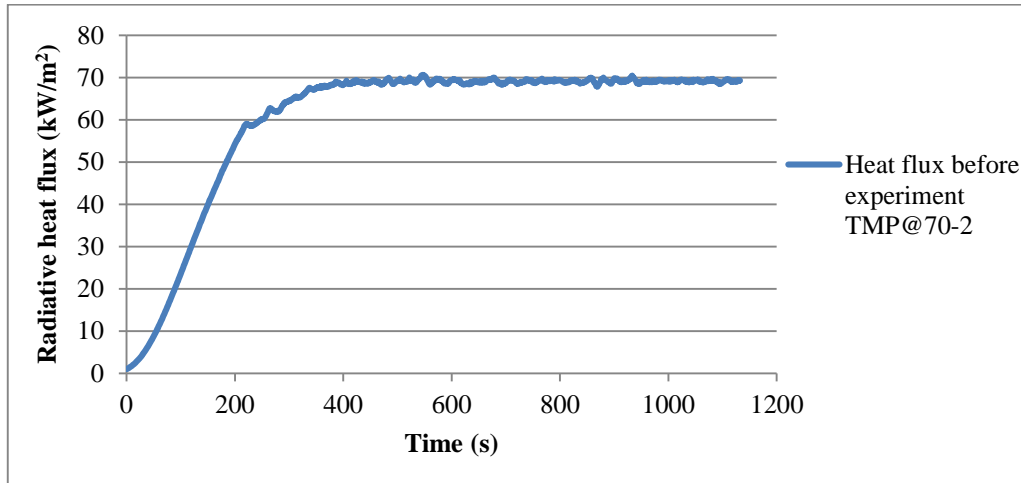
**Figure 10.** The stabilizing radiative heat flux of the cone <u>before</u> an experiment at 70 kW/m$^2$ (experiment TMP@70-2): The cone has reached a stable heat flux after only 400 seconds. The level of stability was nearly ideal.

In order to allow for measuring the mass and the temperatures accurately, separate experiments had to be repeated. The reason was that the thermocouples inside the samples tampered with the weighing system and introduced substantial inaccuracies in the mass measurements. In fact, the used metal-sheathed thermocouples were very rigid to allow the scale to move freely while the scale was highly sensitive (accurate down to milligrams). As a result, measuring the mass of the samples was not possible at the same time as the temperatures were measured. The experiment at each radiant heat flux level was performed for 4 times instead, i.e. twice for measuring the temperatures and twice for measuring the mass losses. The replicate experiments were allowed to facilitate verifying the repeatability and the accurateness of the measurements at each heat flux level.

Another major issue with testing the concrete samples in the cone was the risk of spalling particularly at the high heat flux levels. Avoiding this risk required careful observation of the samples at all times; although the spalling of the samples was likely to occur only in about the first 40 minutes (Majorana et al., 2010). As the samples were not fresh and did not contain considerable amount of water (less than 2% <u>free water</u> by weight as shown in Table 7), explosive spalling was mostly ruled out (Meyer-Ottens, 1974), but mitigation of non-explosive spalling risks was accounted for by having an additional gypsum insulation board readily available beside the apparatus so that it could be put over the sample and prevent further heating in such case. The temperature of the cone could also be dropped very quickly at the high heat flux levels which made it easier to stop the intense heating.

At the experiments with temperature measurements, metal-sheathed thermocouples of the diameter 1.5mm had been drilled from the back side of the samples inside holes with identical diameter size. These were positioned at different depths and points to fully enable investigating whether the temperature distributions within the samples are uniform or they possess 2D or 3D nature. Accordingly, 3 or 4 thermocouples were typically drilled to depths of 7, 10, 15 and 19mm (depth from the surface) near each other at the center of the sample with a spacing of 1 to 2cm, while another thermocouple was typically drilled 1 to 2cm away from the sides or from the corner.

A ceramic insulation board was also put below the samples to prevent heat loss from the back side, while the samples were exposed from their sides and could exchange heat with the ambient air. Similarly, at the experiments with mass loss measurements, the samples were put over the ceramic insulation board and their sides were exposed to the ambient air; however the samples were intact (not drilled) and there were no thermocouples present.

Overall, each experiment involved the following procedure:

- First the cone was heated up while the radiative heat flux level was monitored using a Gardon gage;
- once the radiative heat flux was stabilized at the desired level, the gage was taken out and the recording of the heat flux was ceased[3];
- before any test was done, the initial mass of the concrete sample was weighed using a separate scale;
- when the sample was prepared to be tested, the recording of mass/temperatures was initiated;
- then the sample holder containing the concrete sample and the insulation board was put in the cone and heated at the desired heat flux level;
- when the mass did not indicate significant changes, the recording of data was discontinued and the sample was taken out and allowed to cool down;
- later the sample was weighed for a second time to record its final mass.

---

[3] The radiative heat flux was calibrated only when the cone was heated up from ambient temperatures; so if an experiment was done right after a previous experiment had finished at the same heat flux, the heat flux was considered unchanged for the second experiment.

## 2.2. Modeling

The main characteristics of the model were already presented in Table 1 in Section 1.1. A corresponding 2D model was constructed in Gpyro with the geometry shown in Figure 11. The model consisted of a rectangular solid which had the same dimensions as the concrete samples, i.e. 100mm long and 25mm thick. The thickness was represented by 26 cells in the z-direction and the length was modelled with 3 cells in the x-direction (78 cells in total). Nevertheless, the solid was structured only by 50 cells in effect as the structure of the cells in Gpyro requires "extra" cells on the boundaries. These cells are "half" cells in fact and their nodes precisely overlap the boundary; therefore these half cells can represent the surfaces of the solid and provide quantities such as surface temperature (Lautenberger, 2009, *Gpyro Technical Reference*).
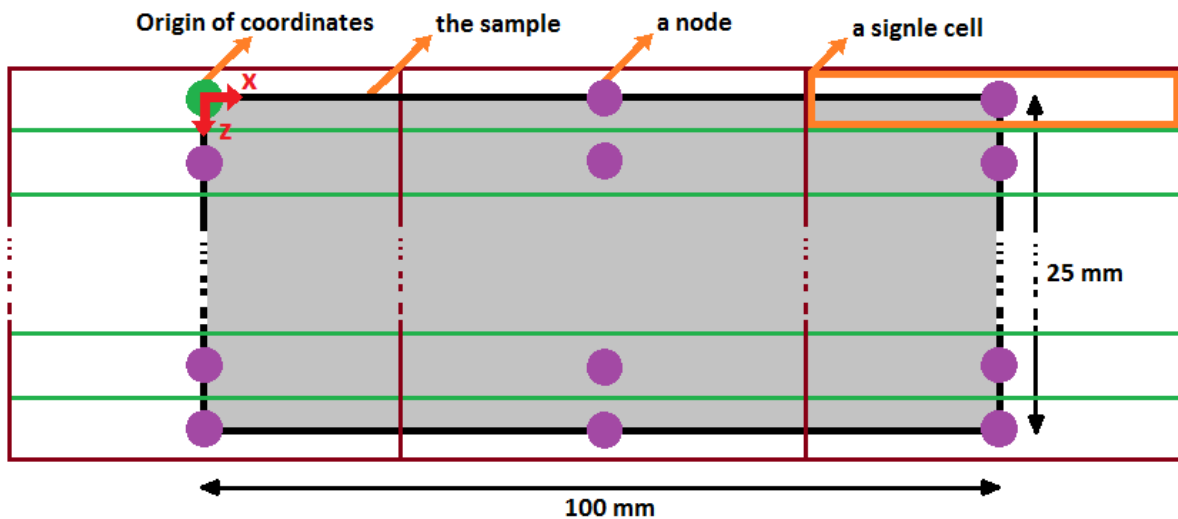


**Figure 11.** **Schematic geometry of the 2D model constructed in Gpyro: each concrete sample was represented as a rectangular solid which was 100mm long and 25mm thick. The thickness was modelled with 26 cells in the z-direction and the length was described by 3 cells in the x-direction, i.e. 78 cells in total (= 26 × 3); however only 50 cells construct the sample effectively since the structure of the cells in Gpyro is constructed such that "extra" cells are needed on the boundaries to correspond to the surface (see the text for explanations).**

The following two reactions were considered to represent the dehydration of the concrete samples in the Cone Calorimeter:

$$\text{Original concrete} \xrightarrow{\text{Heat}} \text{Dehydrated concrete 1 + water vapor} \qquad (1)$$

$$\text{Dehydrated concrete 1} \xrightarrow{\text{Heat}} \text{Dehydrated concrete 2 + water vapor} \qquad (2)$$
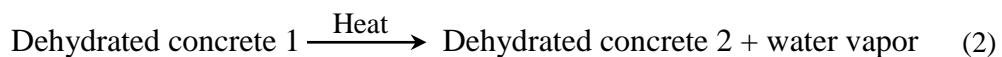
Reaction (1) corresponded to the initial drying as well as the dehydration of calcium hydroxide while the second reaction corresponded only to the decomposition of the C-S-H phase (see Section 1.2.2 for the different transformations). The initial drying process was merged with the decomposition of calcium hydroxide in the first reaction to keep the model as simple as possible and decrease the simulation cost instead. This also allowed evaluating how simple a 'working model' can be.

All the modeling assumptions and characteristics have been presented in Appendix A.3 in form of the template script of the ASCII input files which were used to perform the (inverse) modeling tasks; nevertheless, the main modeling assumptions can be summarized in a qualitative manner as follows[4]:

> The concrete samples possess identical chemical and physical properties since they originate from the same mix.

> The thermal response varies much more considerably with the depth than with the length (which is why the number of the cells is higher in the z-direction).

> Thermal equilibrium is considered between the (produced) gases and the solid concrete.

> The heat flux from the cone falls on the front face of the sample only and is absorbed at the surface (no in-depth absorption of radiation was considered).

> The back-face of the samples is fairly insulated by the insulation board (a convective heat transfer coefficient of 1 $kW/m^2.K$ was considered to account for the minor heat losses due to the separation caused by the thermocouples).

> The natural convective heat transfer which establishes near the sides of the samples is less efficient than the heat transfer above the sample due to the high temperature differences (heat transfer coefficients of 8 $kW/m^2.K$ versus 11 $kW/m^2.s$).

> The thermal properties of the different phases is isotropic, meaning that they are uniform and do not vary in the x- or the z-direction.

> All the gaseous species possess a constant and identical specific heat capacity (1860 kJ/kg.K) which is more biased towards the specific heat of the water vapor (simply because it is more prevalent in the sample).

---

[4] It was recognized during the inverse modeling task that there was occasionally minor consequence to neglecting particular phenomena in the model other than reducing the number of adjustable parameters and the computational cost; therefore certain assumptions are solely in place to keep the 'working model' as simple as possible while these assumptions may not be entirely accurate.

- Each of the dehydration reactions follows a separate 'n-th order' kinetic model, orders to be chosen between 0.9 and 1.1 for the first reaction and between 0.7 and 1.3 for the second reaction (these are usually assumed to be unity, e.g. see Zhang & Ye, 2012).

- The initial mass fraction of water vapor inside the concrete is negligible compared to air (initial gaseous mass fractions of 0.01, 0.23 and 0.76 are considered for water vapor, oxygen and nitrogen, respectively).

- The front face re-radiates and loses heat through radiation whereas the sides do not re-radiate significantly because of their negligible surface area and their lower temperature.

- The boundary conditions consider only presence of water vapor at the front face and only air at the sides and the backside.

- The gas diffusions from/to the sides and the backside of the sample are negligible.

- Porosity is treated as a property of the concrete which relates to its conductivity and density (Lautenberger, 2009, *Gpyro Technical Reference*).

- The boundary conditions do not change over time.

- The enthalpy is assumed to be constant.

- The ambient conditions do not change over time.

Even though not all the above assumptions may be entirely accurate, the number of the parameters that need to be estimated and optimized is still fairly considerable, i.e. 38 parameters, including the material properties of each phase as well as the reaction parameters such as the orders of the reactions and the activation energies. Table 6 indicates the ranges of the main thermal properties which were implemented through the inverse modeling practice based on the values reported in the literature.

In setting up the optimizer, a population size of 1000 was found to be efficient and only the expressive portion of the data from each experiment was used. Temperature and mass loss rate measurements were also coupled from the primary experiments only (see Table 5) and the replicates were only used to verify the repeatability/certainty of the measurements at each radiative heat flux.

After the temperature and mass loss rate data from each primary experiment were coupled, they were used in an inverse modeling simulation using the property estimation component of

Gpyro to estimate and optimize the thermal properties. Consequently, a separate set of thermal properties was discovered for experiments at each heat flux level.

**Table 6.  Ranges of the main thermal properties implemented through the property estimation procedure**

| Parameter | Range | | | |
|---|---|---|---|---|
| | As implemented | | As in the literature*[1] | |
| | min | max | min | max |
| Initial conductivity*[2] (W/m.K) | 0.5 | 3.0 | 0.5 | 3.6 |
| Initial bulk density*[2] (kg/m³) | 2100 | 2400 | 2250 kg/m³ (as measured) | |
| Initial specific heat*[2] (J/kg.K) | 1000 | 2000 | 800 | 1800 |
| Emissivity | 0.8 | 0.95 | 0.85 *[3] | 0.95 *[3] |
| Initial permeability*[2] (m²) | $10^{-18}$ | $10^{-15}$ | $10^{-22}$ *[4] | $10^{-14}$ *[4] |
| Initial pore diameter*[2] (m) | $10^{-11}$ | $10^{-4}$ | $5\times10^{-10}$ *[5] | $3\times10^{-3}$ *[5] |
| Pre-exponential factor (first reaction) (s⁻¹) | 10 | $10^9$ | $10^8$ *[6] | $10^{11}$ *[6] |
| Activation energy (first reaction) (kJ/mol) | 20 | 150 | 59 *[6] | 160 *[6] |
| Enthalpy (first reaction) (J/kg) | $10^2$ | $10^7$ | $1.3\times10^6$ *[7] | $1.4\times10^6$ *[7] |
| Pre-exponential factor (second reaction) (s⁻¹) | $10^7$ | $10^8$ | $10^3$ *[6] | $10^{17}$ *[6] |
| Activation energy (second reaction) (kJ/mol) | 90 | 160 | 83 *[6] | 372 *[6] |
| Enthalpy (second reaction) (J/kg) | $10^5$ | $10^8$ | $2.5\times10^6$ *[7] | $7.5\times10^6$ *[7] |

*[1] References related to the upper and lower bounds of conductivity, specific heat and density of concrete were already presented in Section 1.2.1. Only the rest of the properties are referenced here.

*[2] In an isotropic simulation, all these parameters had to be optimized in their y- and z- direction as well but with identical values. The conductivity and the density of the subsequent phases were also allowed to decrease between 0.95 and 0.99 times the previous phase each time (see Section 1.2.1). Similarly, the specific heat of each phase was allowed to increase between 1.01 and 1.1 times the previous phase, the permeability values were specified to decrease between 1 and $10^{-4}$ times the previous phase each time (since the dried concrete phases are more permeable as explained by Ozawa *et al.*, 2012), and the pore diameters were allowed to increase between 1 and 1.05 times the previous phase every time (since the pore volume must increase by dehydration, as explained by Ichikawa & England, 2004). The according nonlinear dependencies were also defined so that they had minimal effects and did not change the overall behavior.

*[3] Emissivity values are reported from ASHRAE Handbook, 2009; and the Engineering ToolBox, 2014; nevertheless, emissivity values of down to 0.63 have also been reported at temperatures as high as 1000°C (e.g. refer to Table 2.7 in Drysdale, 2011).

*[4] These refer to ranges of intrinsic permeability as reported in Ebensperger & Torrent, 2010; Zhang & Davie, 2013; and also Davie *et al.*, 2010.

*[5] The pore diameters refer to air voids, capillary pores, and gel pores as reported in Karhunen, 2013; and Kumar & Bhattacharjee, 2003.

*[6] The pre-exponential factor and the activation energy of the first reaction (decomposition of calcium hydroxide) are available from two different references, namely Zhang & Ye, 2012; and Mikhail *et al.*, 1965. These are also available for the second reaction (decomposition of calcium silicate hydroxides) from Zhang & Ye, 2012. The implemented ranges were chosen wider to allow for sensitivity analysis mainly.

*[7] The enthalpy of the first reaction (decomposition of calcium hydroxide) is available from Mikhail *et al.*, 1965; whereas the enthalpy of the second reaction (decomposition of calcium silicate hydroxides) could not be found anywhere in the literature and has been reported for the enthalpy of the corresponding hydration reactions instead (Kurtis, 2010).

To verify if the results from the inverse modeling practice are reliable, the estimated material properties at each radiative heat flux level were used to replicate the experimental results at the other heat flux levels. This best allowed evaluating how well the estimated properties could predict the response in other environments, and more precisely, how 'meaningful' or 'usable' the results from the followed inverse modeling methodology could generally be in the practice of thermal behavior prediction. It needs to be emphasized here once more that the estimated thermal properties from the genetic algorithm optimization are not necessarily the absolute optimal properties, neither they are 'unique', but they are sets of properties that simply provide a near–optimal prediction of the experimental data given the constraints of the underlying model. Nevertheless, the results that are obtained with these near-optimal properties are as good as those that would have been obtainable if optimal material properties were used in a fully sophisticated model.

As the temperatures in the experiments at 10 and 30 kW/m$^2$ were not as high as the other experiments to fully instigate the second dehydration reaction, the simulations for these experiments were performed once with the first dehydration reaction only and once with both of the dehydration reactions to investigate the effects of including/excluding the second decomposition reaction.

# 3.  Results

This section provides an overview of the most important information which was obtained during the experiments and from the inverse modeling practice. The complete results can be found in Appendix A.2.

## 3.1. Experimental results

The typical behavior above 50 kW/m$^2$ was that water vapor initially vaporized out so quickly that clouds of vapor could be seen above the surface for several minutes (see Figure 12). Consistently, a major part of the overall mass loss belonged to these and the next few minutes. None of the samples spalled, excluding one sample which had a very minor loss of surface concrete cover under 85 kW/m$^2$; however all of the samples did develop cracks upon heating. These phenomena are illustrated in Figure 13.

Figures 14 & 15 display the mass loss rates as well as the mass loss percentages measured at different heat flux levels during the primary experiments. Ranges of the overall mass loss percentage during the first 4000 seconds period varied between 2.10% and 4.53% (of original mass), corresponding respectively to experiments MLR@10-1 and MLR@85-1.



**Figure 12.  Two samples being heated under the cone at 85 kW/m$^2$: the left picture shows an experiment for measurement of mass only (note the cloud of water vapor which is visible at the top of the sample); the right picture shows the counterpart experiment with thermocouples connected for recording the temperatures.**
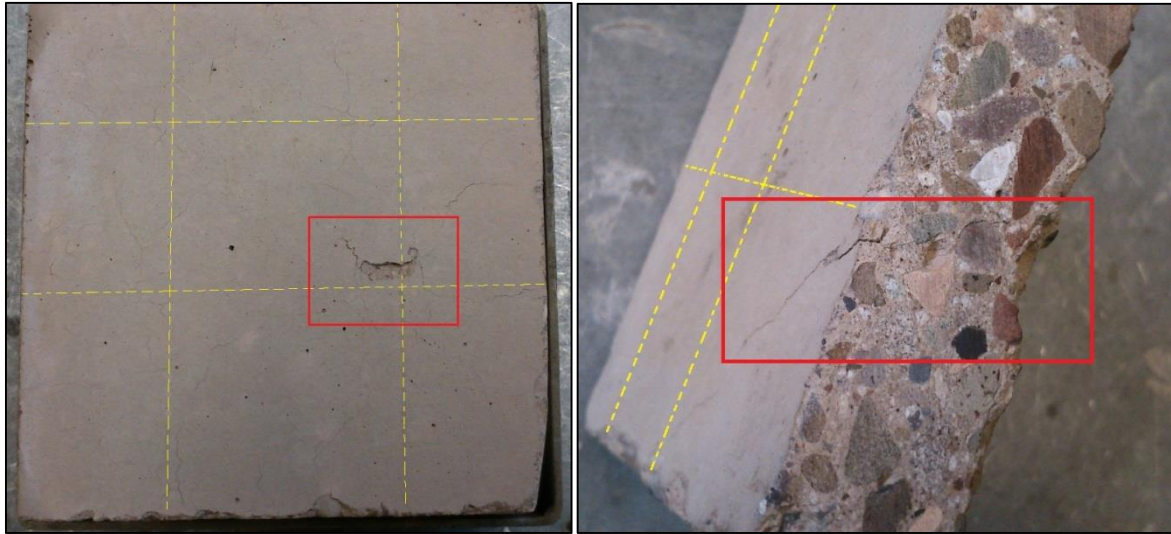
**Figure 13.** Minor loss of concrete cover and also development of cracks in the concrete samples: the concrete sample tested in experiment MLR@85-1 (shown on the left) was the only sample to have a noticeable loss of concrete cover. Cracks, however, developed in almost all the samples but varied in size and length. The cracks were considerable near the reinforcement bars (shown on the right) and frequently developed wider along the bars. The dotted lines indicate the positioning of the bars.
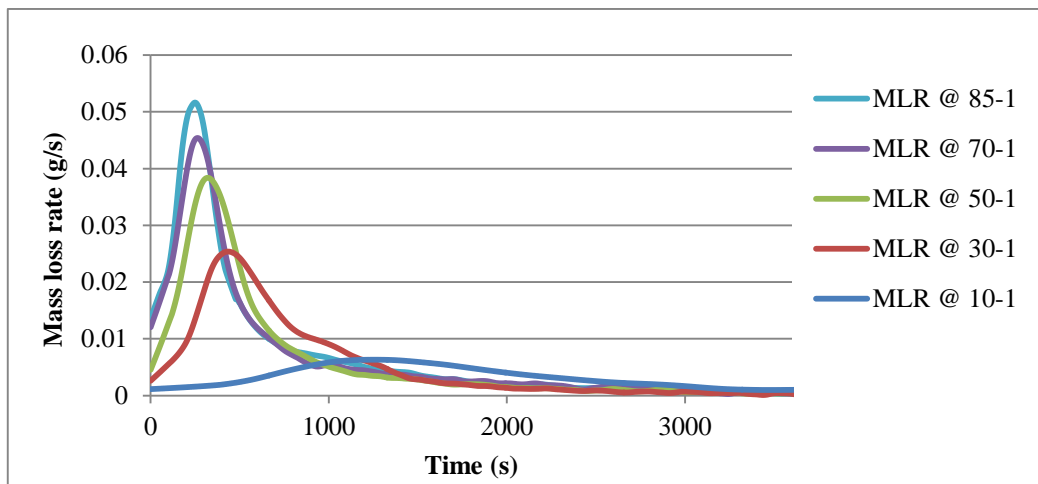


**Figure 14.** Mass loss rates measured at different heat flux levels during the primary experiments: the mass loss rates have been determined using the five-point numerical differentiation method suggested by ISO 5660-1 document for cone calorimetry (ISO5660-1:2002(E), 2002) and were normalized using LOESS Utility (Peltier, 2014). The overall loss of mass in each experiment was calibrated so that it matched the value measured in the experiment.
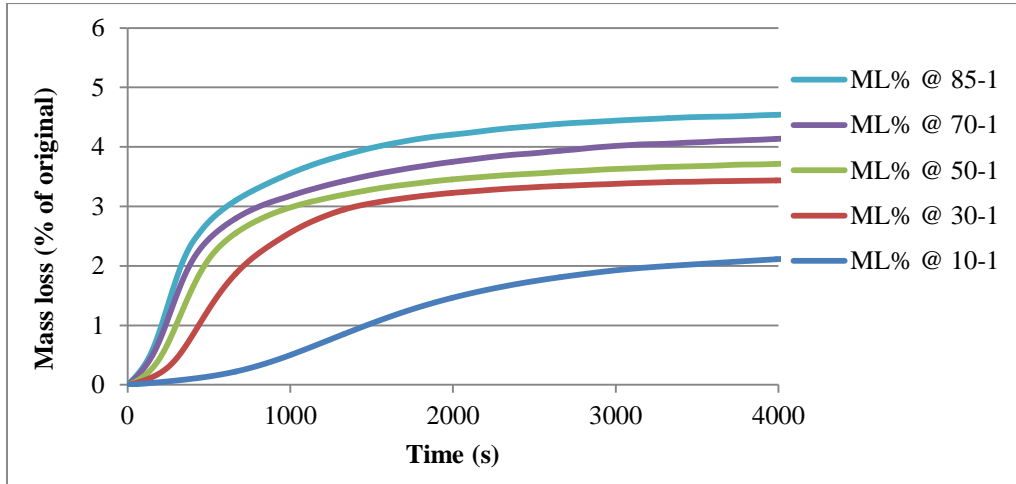
**Figure 15. Mass loss (% of original) at different heat flux levels during the primary experiments: the cumulative mass loss has been calculated from the normalized mass loss rate data shown in Figure 14.**

The repeatability of the mass loss rates is portrayed in Figure 16 which illustrates the results from two replicate experiments along with their counterpart primary experiments. The shown curves correspond to the best and the worst agreements achieved in the mass loss rate data. In a consistent manner, the mass loss rates in the replicate experiments were marginally higher than their counterparts from the primary experiments.
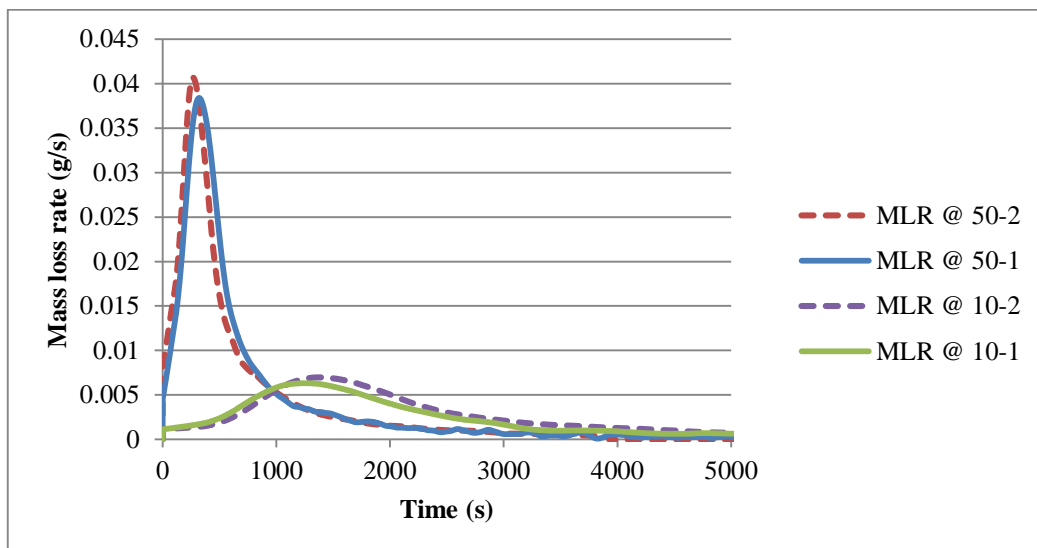


**Figure 16. The best and the worst agreement achieved in mass loss rate data: repeatability was worst at experiments under 50 kW/m² while it was best at experiments under 10 and 70 kW/m². The solid curves correspond to the primary experiments and the broken curves correspond to the replicate experiments under 10 and 50 kW/m². Consistently, the mass loss rates from all the replicate experiments were slightly higher than their counterparts from the primary experiments.**

With only one exception, the thermocouples at every depth indicated somewhat higher temperature measurements at the replicate experiments than in the primary experiments. For instance, Figure 17 demonstrates the evolution of temperatures at the depth of z = 7mm for all the experiments. Primary and replicate TMP@50 experiments crossed over each other with the worst agreement (~ 25 to 30℃ difference) while TMP@10 featured the best conformity. Three outliers were present in total, namely thermocouples at z = 19mm for experiments TMP@50-2 and TMP@70-1 and also at z = 15mm for TMP@85-1 at the corner.
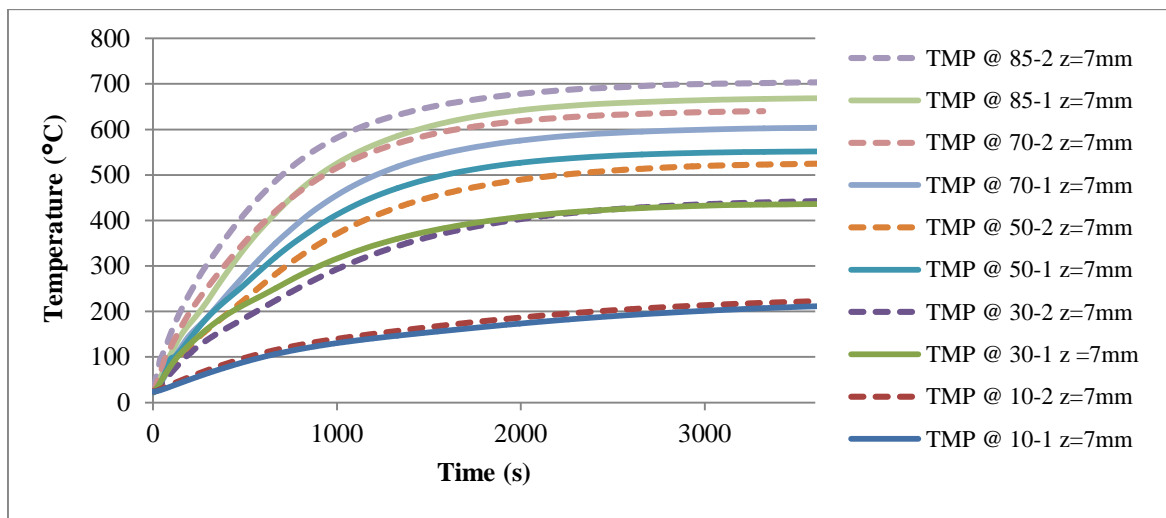


**Figure 17. Temperature measurements at 7mm from the surface for the replicate (broken) and the primary experiments (solid) during the first hour of heating: all the replicate experiments consistently indicate slightly higher temperatures than the primary experiments except the replicate experiment TMP@50-2 which crosses over its counterpart.**
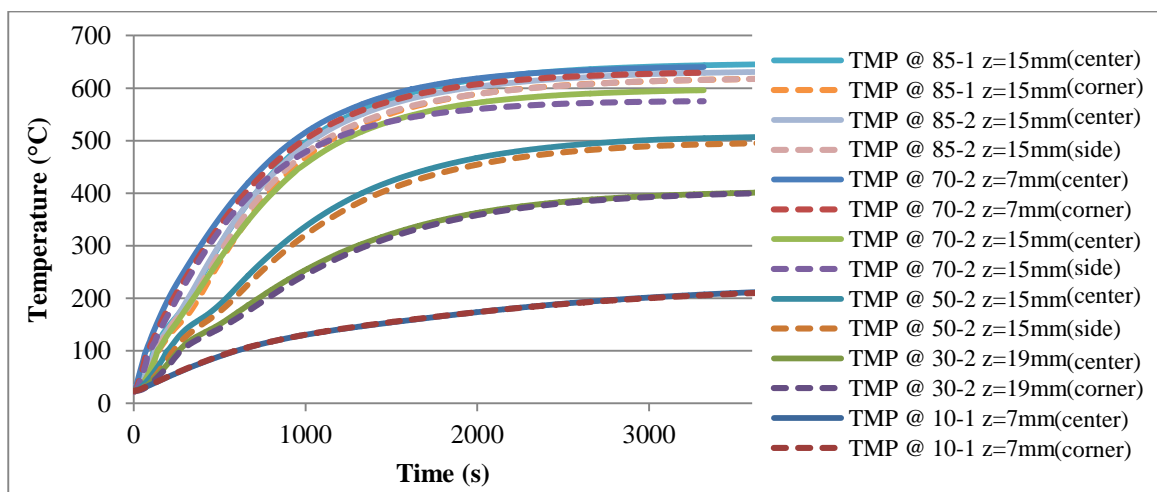


**Figure 18. Uniformity of temperature distributions at the sides and the corners compared to the center in various experiments: temperature distributions at the sides and at the corners (broken) match suitably with the corresponding distributions at the center (solid) thus 1D behavior prevails overall. The only outlier here is from TMP@85-1 at z = 15mm at the corner.**

The dimensionality of the temperature distributions within the samples proved majorly 1D. This was tested through comparison of the temperature distributions at the corners and the sides with the corresponding distributions established in the center at identical depths (shown in Figure 18 for various experiments); although in some cases the measurements were dubious and suggested crossover evolutions or temperature differences up to 20℃.

The additional sample which was also put in the oven to estimate the overall amount of free water, reached a steady mass after 7 days. Hence, the overall mass loss and thus the average amount of free water in the samples was estimated to be 1.82% (of original concrete mass) as illustrated in Table 7.

Table 7.  Mass loss of the oven-dried sample and the according lost free water

| Measurement in the test | Days in oven | | | |
|---|---|---|---|---|
| | Day 1 | Day 3 | Day 6 | Day7 |
| Lost free water (% of original mass) | 0% | 1.75% | 1.82% | 1.82% |

# 3.2. Inverse modeling results

Figure 19 depicts the typical evolution of different concrete phases as modelled in a simulation relating to experiments at 50 kW/m$^2$. First, original concrete (Phase 1) dries and dehydrates gradually to Dehydrated Concrete 1 (Phase 2); meanwhile at the surface this newly produced phase begins to dehydrate and transform to Dehydrate Concrete 2 (Phase 3). At some point, Phase 1 is fully transformed and its mass fraction becomes zero. Phase 2, however, dehydrates only partially in all the simulations except for the simulation of experiments at 50kW/m$^2$ which is shown in Figure 19.

All of the simulations follow a typical pattern. As shown in Figure 20, the simulations tend to underestimate the rapid rise and the peak of mass loss rates but overestimate the rates elsewhere. The cumulative mass losses are reproduced comparatively well (see Figure 21). Similarly, the temperature distributions were often reflected precisely as displayed in Figures 22 & 23 whereas the evolution of pressure and gaseous species could not reflect the

true physics of the problem as the moisture migration was not accounted for by the model (see Figures 24 to 26).

Using the optimized thermal properties at each heat flux level, the thermal behavior at other radiative heat fluxes was replicated. Figure 27 shows the cumulative losses of mass as replicated using the optimized thermal properties from the simulation of experiments at 85 kW/m$^2$. As it is displayed in this figure, the replicated mass loss has been reasonable for experiments down to 30 kW/m$^2$ while it has rendered ineffective at 10 kW/m$^2$.

Overall, the genetic algorithm converged reasonably well within the first 100 generations and took less than 15 hours to run on a quad-core laptop with a 2.4 GHz processor. Figure 28 illustrates an example of convergence by the algorithm. The main obtained optimized thermal properties have also been summarized in Table 8 along with the corresponding values from the literature.



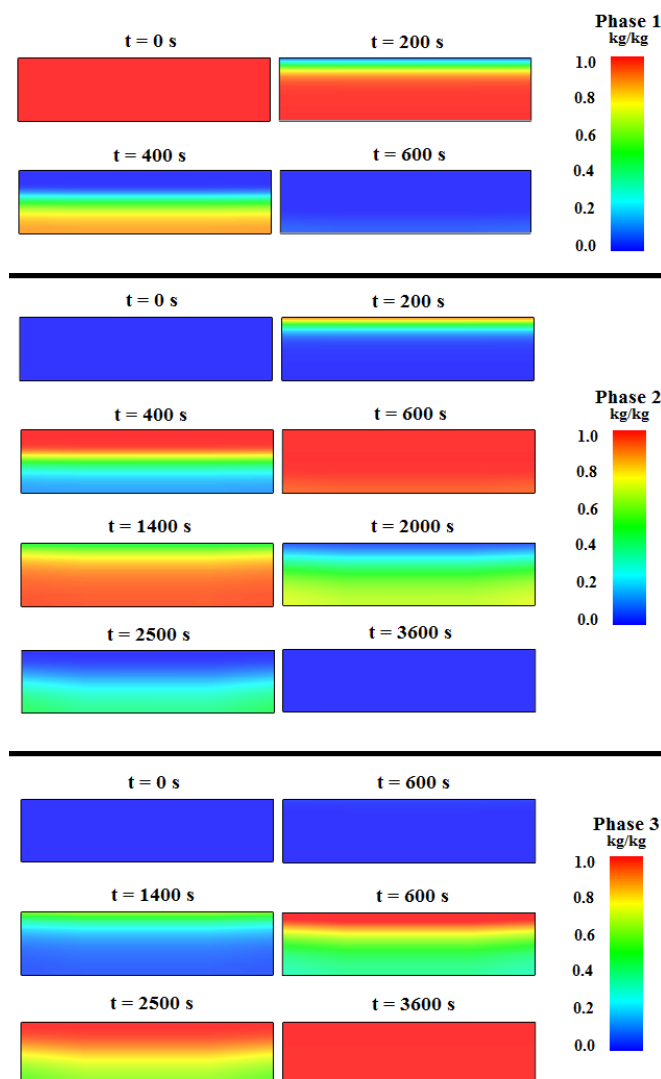**Figure 19.** The typical evolution of different concrete phases as modelled in a simulation relating to experiments at 50 kW/m$^2$: Phase 1 refers to 'Original Concrete', Phase 2 is 'Dehydrated Concrete 1' and Phase 3 is 'Dehydrated Concrete 2' as defined in reactions (1) and (2) in Section 2.2. Initially, Phase 1 dries and dehydrates to form Phase 2 then this phase gradually dehydrates for the second time to form Phase 3. At some point in all the simulations, Phase 1 was fully transformed; however Phase 2 was transformed completely only in this simulation (at 50 kW/m$^2$).
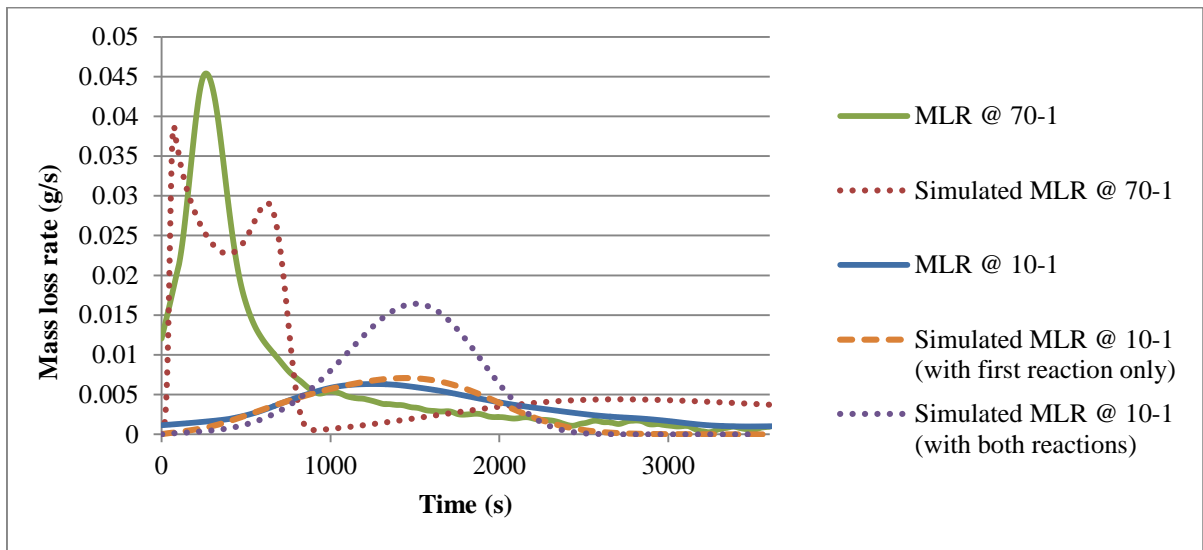
**Figure 20.** Simulated mass loss rates from the worst and the best optimizations along with their experimental counterparts (from @70-1 and @10-1, respectively): the optimized mass loss rate curves from all the simulations majorly follow the pattern observable for the curve of 'Simulation MLR @ 70-1'. As such, they majorly underestimate the rise and the peak of mass loss rates while they overestimate the rates elsewhere. The two different simulations at 10 kW/m² indicate that better results are achieved when the second reaction is omitted from the model.
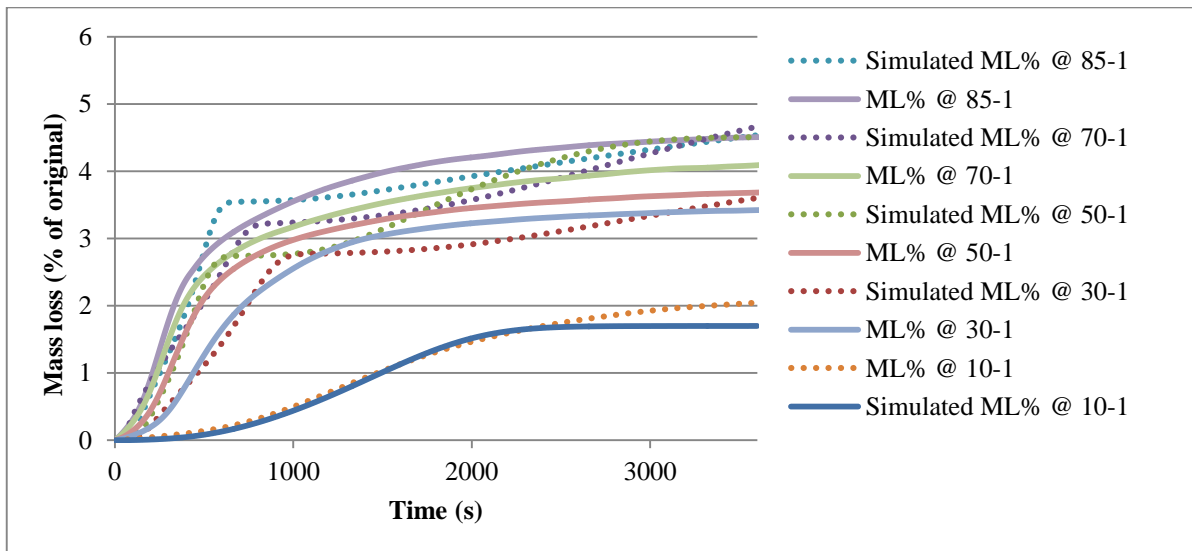


**Figure 21.** All the simulations of cumulative losses of mass along with their experimental counterparts: the disagreements in the cumulative losses of mass are much less pronounced than the mismatches that exist in the simulations of mass loss rates (see **Figure 20**). Typically, the ultimate cumulative mass losses have been overestimated while the overall agreement is satisfactory.
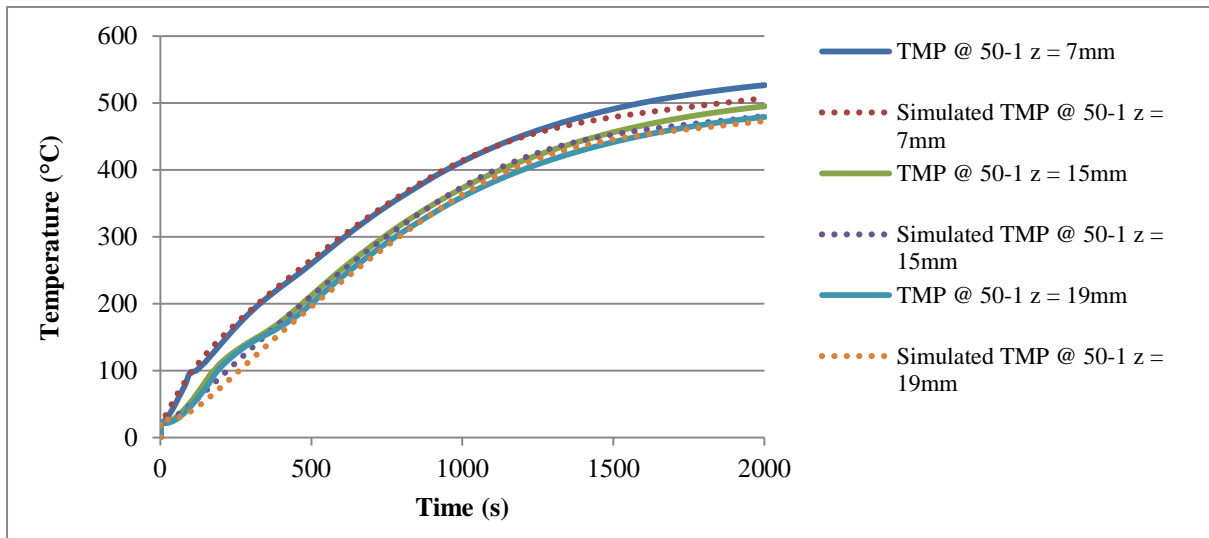
**Figure 22. Simulated temperatures for the experiments at 50 kW/m² (the best achieved agreement among the simulations): most of the simulations could replicate the temperature distributions as accurately as predicted in this simulation given that enough number of generations was allowed to be simulated by the optimizer.**
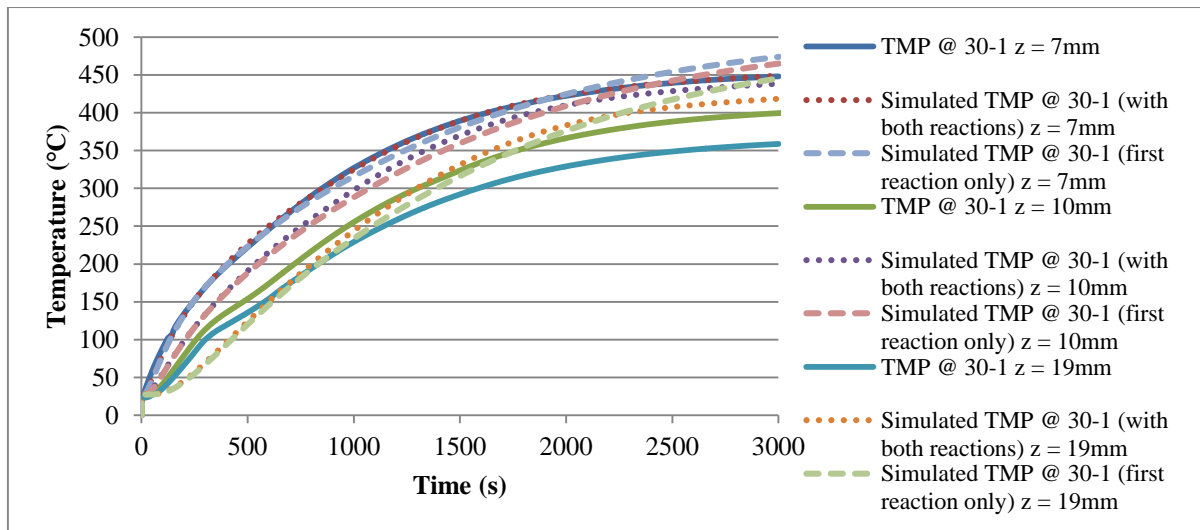


**Figure 23. Simulated temperatures for the experiments at 30 kW/m² (the worst achieved agreement among the simulations): the bottom temperature distribution curves (z = 19mm and 10mm) have mostly been overestimated while the upper curve (z = 7mm) has matched with the experimental results adequately. The simulation results have been improved when both the dehydration reactions have been implemented rather than only the first reaction. This was the other way around for simulations of experiments at 10 kW/m².**
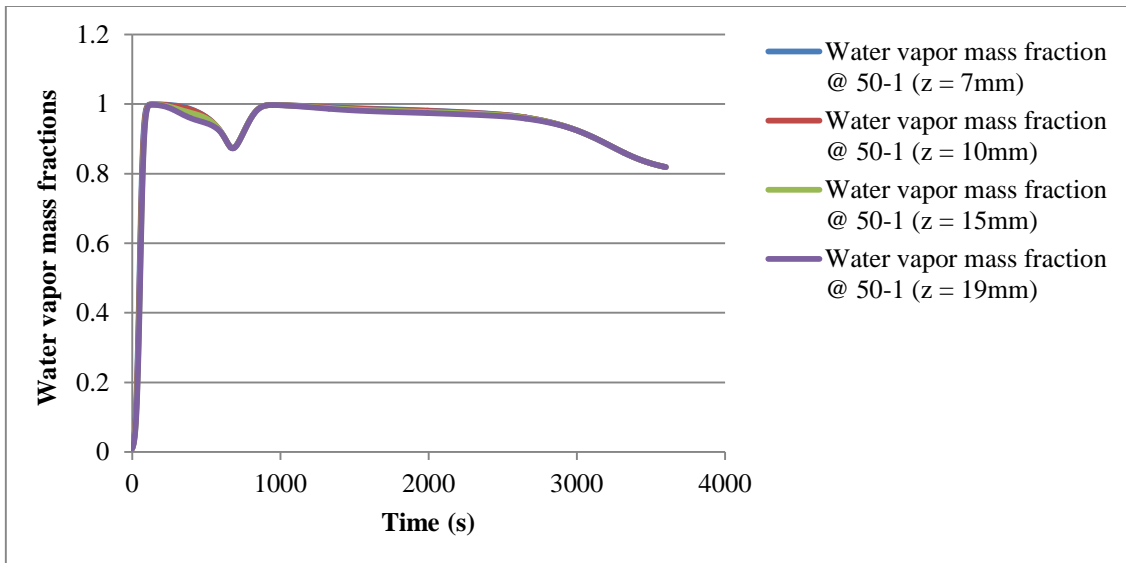
**Figure 24. An example of the simulated evolutions of water vapor mass fractions at different depths (as simulated in simulations of experiments @50-1): the evolution of water vapor mass fractions is more or less identical at every depths. Initially the mass fraction of water vapor increases very rapidly until it takes up the entire voids in the sample, then it is gradually liberated through the boundaries and decreases over time. Then again at some point, water vapor starts to gather and become dominant. Later on, the mass fraction of water vapor begins to dwindle again and air entrains to the concrete.**
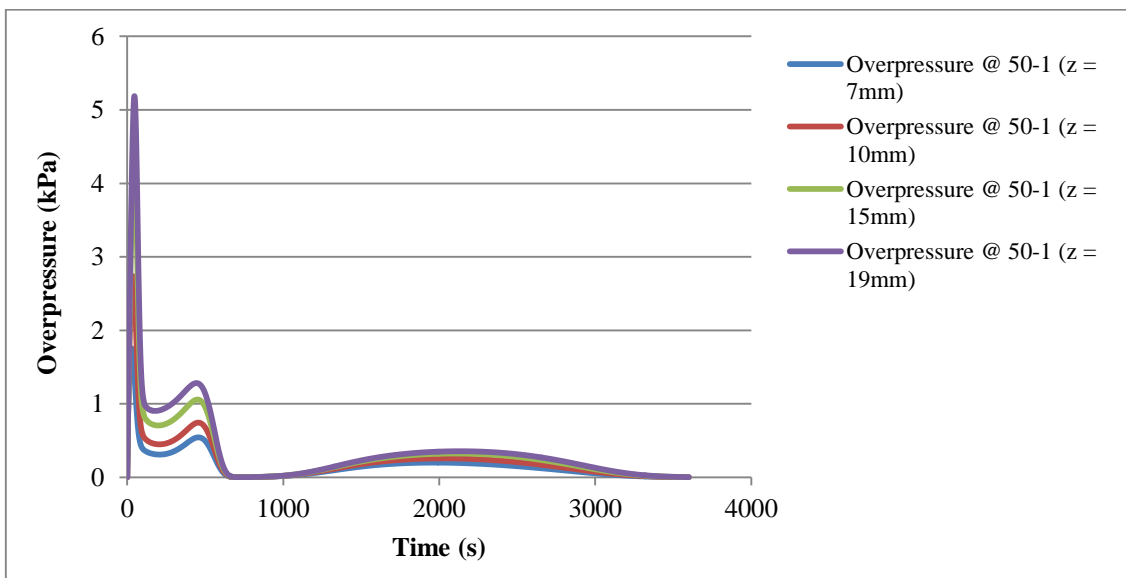


**Figure 25. An example of the simulated overpressure evolutions inside the concrete samples at different depths (as simulated in simulations of experiments @50-1): the overall pressure build-up was insignificant in all the simulations (< 50 kPa) and the evolution of pressure is somewhat similar at different depths. Initially water vapor builds up pressure very rapidly while this is relieved similarly quickly. Later on, a second build-up of pressure develops but it is relieved all fast again and it is diminished almost entirely afterwards.**
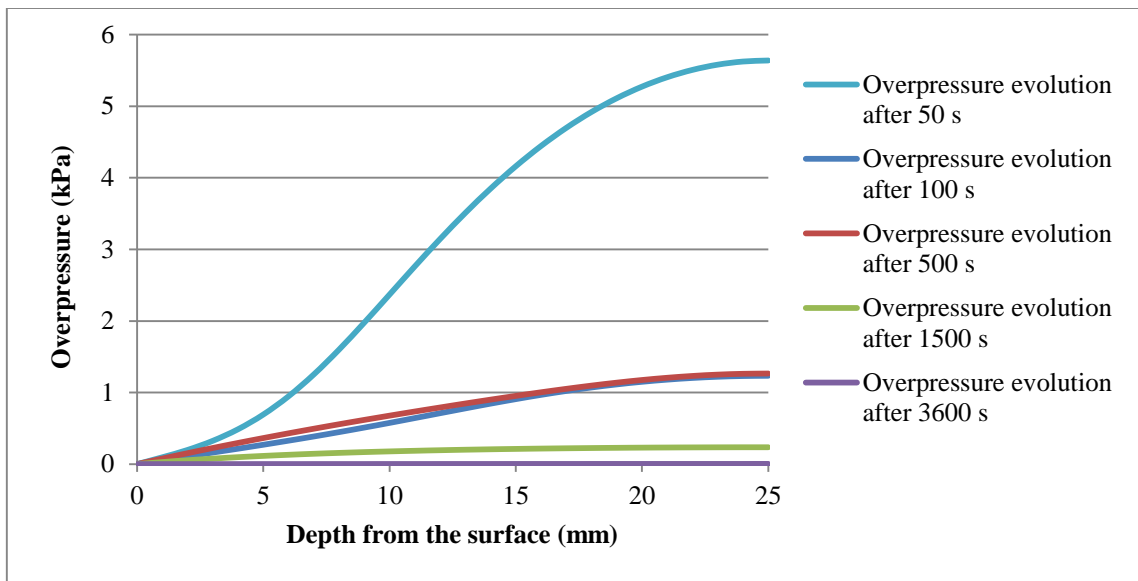
**Figure 26.** Simulated pressure evolutions at different times for experiments at 50 kW/m²: note that the x-axis is depth from the surface; therefore the shown pressure evolutions suggest higher pressures at the bottom of the sample which is <u>not</u> in agreement with the evolutions suggested in the literature (illustrated in Figure 7).
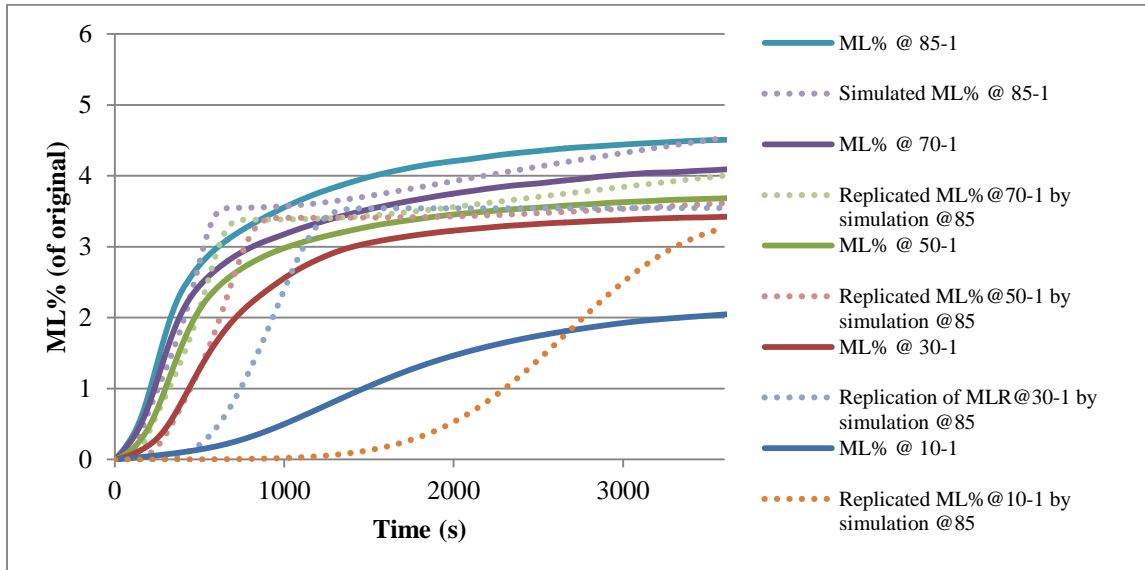


**Figure 27.** Replicated cumulative losses of mass from the simulation of experiments at 85 kW/m²: replications have been reasonable for experiments down to 30 kW/m² while the replicated mass loss evolution at 10 kW/m² greatly disagrees its experimental counterpart.
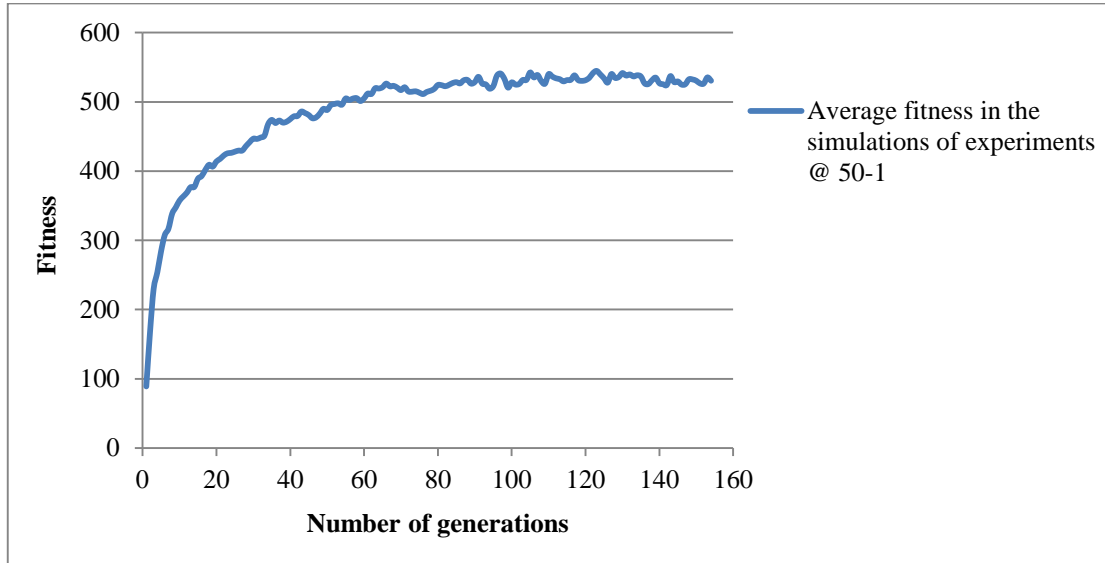
**Figure 28.** An example of the convergence of the genetic algorithm from the simulations of experiments at 50 kW/m$^2$: the average fitness has converged within the first 100 generations. The maximum fitness which could be achieved in these simulations, in theory, has been 1200; however this is the point where all the simulated values match the experimental data points. The maximum achievable fitness depends on the number of available experimental data sets and a few other model parameters (Lautenberger, 2009, *Gpyro Technical Reference*).

**Table 8. Ranges of the obtained optimized thermal properties in different simulations**

| Parameter | Range | | | | |
|---|---|---|---|---|---|
| | as optimized[*1] | | | as in the literature[*2] | |
| | min | average | max | min | max |
| Initial conductivity (W/m.K) | 0.97 | 1.64 | 2.9 | 0.5 | 3.6 |
| Initial bulk density (kg/m$^3$) | 2223 | 2265 | 2343 | 2250 kg/m$^3$ (as measured) | |
| Initial specific heat (J/kg.K) | 1134 | 1560 | 1820 | 800 | 1800 |
| Emissivity | 0.85 | 0.89 | 0.94 | 0.85 | 0.95 |
| Initial permeability (m$^2$) | $1\times10^{-16}$ | $5\times10^{-16}$ | $7\times10^{-16}$ | $10^{-22}$ | $10^{-14}$ |
| Initial pore diameter (m) | $5\times10^{-10}$ | $1\times10^{-5}$ | $7\times10^{-4}$ | $5\times10^{-10}$ | $3\times10^{-3}$ |
| Pre-exponential factor (first reaction) (s$^{-1}$) | $5\times10^{4}$ | $2\times10^{5}$ | $7\times10^{5}$ | $10^{8}$ | $10^{11}$ |
| Activation energy (first reaction) (kJ/mol) | 58 | 64 | 70 | 59 | 160 |
| Enthalpy (first reaction) (J/kg) | $1.6\times10^{3}$ | $1.8\times10^{4}$ | $5.6\times10^{4}$ | $1.3\times10^{6}$ | $1.4\times10^{6}$ |
| Pre-exponential factor (second reaction) (s$^{-1}$) | $1.5\times10^{5}$ | $3.2\times10^{6}$ | $1.3\times10^{7}$ | $10^{3}$ | $10^{17}$ |
| Activation energy (second reaction) (kJ/mol) | 129 | 145 | 180 | 83 | 372 |
| Enthalpy (second reaction) (J/kg) | $1.2\times10^{7}$ | $3.3\times10^{7}$ | $8.7\times10^{7}$ | $2.5\times10^{6}$ | $7.5\times10^{6}$ |

[*1] Optimized values correspond to the simulations @85-1, @70-1, @50-1, @30-1 with both reactions, and @10-1 with first reaction only.

[*2] References related to the upper and lower bounds of the parameters were already presented in Table 6.

# 4. Discussion

The repeatability of both the mass loss evolutions and the temperature distributions has proven satisfactory; although slightly higher values have been measured in almost all the replicate experiments (see Figures 16 & 17). This is mainly because most of the replicate experiments were performed after the primary experiments. As the initial ambient temperature in the cone was somewhat higher, this caused the replicate experiments to heat up the concrete samples slightly faster which in turn increased the rates of mass loss.

The evolution of temperatures within the samples has mainly been 1D as it can be inferred from Figure 18. The shown temperature distributions at the sides and at the corners have been well in uniformity with the evolutions measured at the center, except in a few cases. Apart from the effects of marginal 2D temperature evolutions and the inherent minor inaccuracies in functioning of the thermocouples themselves, the observable disagreements in the temperature evolutions measured by the thermocouples may have stem from drilling faults, ambient air temperature change, development of (micro-) cracks or presence of inborn faults between two adjacent thermocouple holes, inadvertent dispositioning of the thermocouples, imprecise levelling of the sample on the scale, or differences arisen from positioning of thermocouples inside an aggregate or inside the cement.

The experimentally obtained mass loss rates as shown in Figure 14 suggest progressively faster rates of mass loss at higher heat flux levels and all feature an inverse Gaussian distribution. More remarkably, the peaks of the mass loss rate curves tend to shift to earlier times as the heat flux level increases. As shown in Figure 29, these peaks seem to grow with a perfect exponential trend which can practically allow for replicating the mass loss rates at other radiative heat flux levels between and about 10 and 85 $kW/m^2$ with reasonable accuracy. This is possible by an exponential interpolation (or extrapolation) based on two adjacent heat fluxes and their peak times. After locating the desired peak, the mass loss rates can be established using an inverse Gaussian distribution. This is a marked advantage offered by experimenting based on 'heat flux levels' rather than based on 'heating rates' (℃/min) which is habitually done (e.g. according to the ISO standard fire as in Lim *et al*., 2004; or other various rates as in Debicki *et al*., 2012; or Kalifa *et al*., 2000).

0.8
0.7
Peak mass loss rate (g/s)
0.6
0.5
0.4
0.3
0.2
0.1
0

◆ MLR Peak @ 85-1
■ MLR Peak @ 70-1
▲ MLR Peak @ 50-1
✕ MLR Peak @ 30-1
✳ MLR Peak @ 10-1
— Trendline

$$\text{MLR Peak (g/s)} = 628.41\ t^{-1.289}$$
$$R^2 = 0.9985$$

0    500    1000    1500    2000
Time (s)
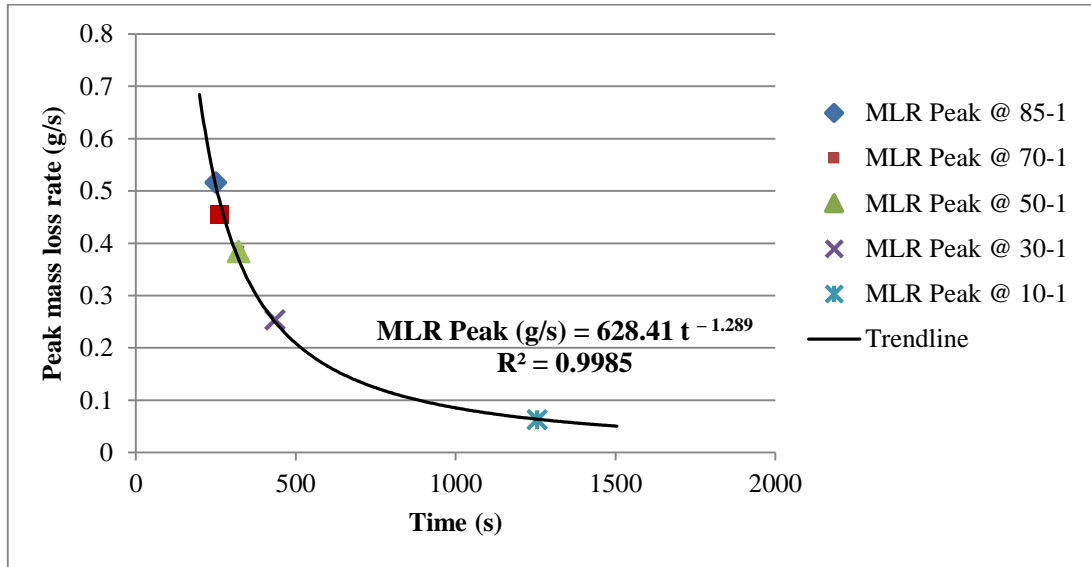
**Figure 29.** Peaks of the mass loss rates obtained from the primary experiments: the peaks perfectly follow an exponential trend (equation shown on the graph) which can be used to replicate the mass loss rates at other heat flux levels. It must be noted, nevertheless, that the obtained equation only provides the positioning of the peak versus time; i.e. in order to replicate the mass loss rate curves in other heat fluxes, it will be needed to perform an exponential interpolation (or extrapolation) based on two adjacent heat fluxes and their peak times to locate the desired peak. It would be possible afterwards to reproduce the rates using an inverse Gaussian distribution.

As it can be inferred from Figure 29 and also the cumulative mass losses presented in Figure 15, when the heat flux level is changed from 10 kW/m$^2$ to 30kW/m$^2$, the mass loss rates and the cumulative loss of mass increase substantially; whereas the corresponding increase by changing from 30 kW/m$^2$ to 50 kW/m2 is comparatively marginal. This is because calcium hydroxide starts to decompose just at about the temperatures achieved in the experiments at 30 kW/m$^2$, i.e. 400 ℃ (see Section 1.2.2); while the experiments at lower heat fluxes cause evaporation of capillary, gel and free waters only since they feature much lower temperatures (below 200 ℃ at 10 kW/m$^2$). Surprisingly, the incorporated carbonate aggregates did not indicate any significant decomposition during any of the experiments much in contrast with what is suggested in the literature (see Figure 2 and also Section 1.2.2).

The overall loss of mass has been less than 4.5% of the original mass of the concrete in all the experiments. Since the amount of free water was estimated from the oven-dried sample to be about 2% of the original mass (see Table 7), the considerable mass loss at the beginning of heating and thus the visible cloud water vapor in Figure 12 must correspond only to the

evaporation of free water. This also confirms that calcium hydroxide has not decomposed in the experiments performed at 10 kW/m$^2$ since they resulted in only up to 2% loss of mass.

The evolution of different concrete phases in the model is reflected as expected. The drying and the dehydration reactions evolve from the surface and the phases transform based on the considered reactions (see Figure 19). As calcium silicate hydroxides are known to decompose completely only above 900 ℃ (see Section 1.2.2), it was expected that the simulations suggest only partial transformation of the calcium hydroxide phase. All the simulations reflected this indeed except the simulation of the experiments at 50 kW/m$^2$ which suggested complete decomposition of both the calcium hydroxide and the calcium silicate hydroxide phases. This has accordingly caused overestimation of the cumulative mass loss in this simulation. It is expected that this simulation requires more number of generations in its optimization and it should be allowed to run until a better convergence, otherwise the nature of the simulation reflects the expected behavior.

The simulated mass loss rates as shown in Figure 20 (and more completely in Figure 41 in Appendix A.2.2) tend to majorly overestimate the rate; although the rapid rise and the peak of mass loss rates are mostly underestimated. This is largely due to the fact that the loss of mass has begun very suddenly from the very beginning of heating due to the rapid evaporation of free water. As the two different performed simulations of the experiments at 10 kW/m$^2$ suggest, it is possible to reflect the initial rise only when the drying is considered in one separate reaction. Among all the simulations, this is the only one to predict the growth of mass loss entirely correctly in fact. This suggests that the respective evaporation of capillary, gel and free waters must be accounted for by separate reactions so as to catch the described initial rise properly.

The predicted cumulative losses of mass are less affected by the mismatches in the mass loss rate simulations which is mainly due to the opposing effects of the discussed underestimations and overestimations (compare Figures 20 & 21). Accordingly, the rapid nature of evaporation and the slower growth of the dehydration processes have been reflected well but the ultimate losses of mass have been majorly overestimated. It is important to note, however, that the mass loss percentages should not be compared from experiment to experiment because the samples did not have the same original mass. Therefore, mass loss percentages could only be used to verify the accuracy of the simulations, and not the accuracy among the experiments themselves.

Most of the simulations could replicate the temperature distributions well as displayed in Figures 22 & 23 (and more thoroughly through Figures 46 to 49 in Appendix A.2.2); however sometimes some of the temperature distribution curves did not match as suitably as the others. These mismatches particularly caused wrong predictions of the growth rate of the temperatures while the ultimate reach of the curves was habitually accurate. Performing the simulation of experiments at 30 kW/m$^2$ once with both the dehydration reactions and once with the first reaction only (shown in Figure 23), indicated only slight improvement when the second reaction was present. This implies that the first dehydration reaction has been mostly sufficient to accurately reflect the ongoing decomposition, i.e. that of calcium hydroxide at temperatures above 400℃ which are achieved in this experiment. Overall, the temperature predictions are well satisfactory.

The overall pressure build-up was insignificant in all the simulations (< 50 kPa). A pressure build-up to instigate any explosive spalling would need to be as large as 3 MPa (Ozawa *et al*., 2012). Nevertheless, the simulated evoluiton of pressure and gaseous spceices suggested by Figures 24 to 26 did not follow the patterns suggested by the literature (see Figure 7). As suggested by Ozawa *et al*. (Ozawa *et al*., 2012), water moves to the inner part of the concrete and creates a humid front at which the pressure is the highest. Since neither the moisture condenstion nor the moisture migration were modelled in this study, the build-up of water vapor pressure near the surface was not predicted properly and thereore the evolution of pressure and gaseous species could not reflect the true physics of the problem. As summarized by Majorana (Majorana *et al*., 2010), the vapor pressure in partially saturated pores must be the saturation vapor pressure; in empty pores it must be the pressure of superheated steam, and in fully saturated pores it must be hydraulic pressure. These can only be modelled if condensation and migration of moisture are included in the model.

The use of the optimized thermal properties for replicating the behavior at other radiative heat fluxes proved promising; however it was discovered that the optimized thermal properties can predict the thermal behavior more reliably when they are used in the vicinity of the environment from which they have been extracted originally. In other words, results worsened as the target environment diverged from the originally optimized environment. As shown in Figure 27, the estimated properties from the simulations of the experiments at 85 kW/m$^2$ have been able to describe the cumulative losses of mass at other heat flux levels practically well; however this has only been true down to a heat flux level of 30 kW/m$^2$ (for the corresponding replicated temperatures see Figure 46 to 49 in Appendix A.2.2). The

replicated mass loss evolution at 10 kW/m$^2$ greatly disagrees its experimental counterpart and sugests that the estimated properties from the simulations at 85 kW/m$^2$ do not include the correct behavioral characteristics to replicate the response of concrete at 10 kW/m$^2$. This is mainly due to the fact that these estimated thermal properties have embedded the characteristics of dehydration reactions which occur only at high temperatures (i.e. the decomposition of the calcium hydroxides as well as the decomposition of calcium silicate hydroxides well above 400 ℃). The maximum temperatures measured during the experiments at 10 kW/m$^2$ were less than 200 ℃ which is too low to activate these dehydration reactions. Therefore, only the first reaction must be considered to account for the drying process, otherwise the mass loss rates will be overestimated. This was further verified by simulating these experiments once with both the dehydration reactions and once with the first reaction only. As shown in Figure 20, the simulation of experiments at 10 kW/m$^2$ has agreed with the experimentally measured mass loss rates accurately when only the first reaction has been implemented; whereas including the second reaction has introduced large overestimations.

Overall, the genetic algorithm has performed well and proved cost effective. As illustrated in Figure 28, convergence by the algorithm could be achieved in the first 100 generations and this is very time-efficient when one considers simulation run-times of 15 hours on a quad-core laptop with a 2.4 GHz processor.

The most sensitive parameters in the optimizations were permeability, activation energies, the pre-exponential factors and enthalpies, while the pore diameter and the emissivity values had the most marginal effects. Similarly as insignificant were the incorporated nonlinear temperature dependencies which had been considered. As it can be inferred from Table 8, the optimized parameters of the first reaction were largely different from the literature. This mainly originated from the fact that the drying process had been merged with the first dehydration reaction. The optimized conductivity, specific heat and pore diameter parameters featured the largest variations while permeability and density were the most stable parameters. Permeability was consistently of the magnitude $10^{-16}$ m$^2$ which is indeed in the right range for normal-strength concrete (Zhang & Davie, 2013). The average bulk density is also notably close to the measured value, i.e. 2265 versus 2250 kg/m$^3$.

# 5.  Conclusions

Testing the two-way reinforced concrete samples in the Cone Calorimeter yielded highly repeatable results and it was found that an accurate exponential pattern exists among the mass loss rate peaks from tests carried out at different heat flux levels which could allow replication of the mass loss rates at different heat flux levels with reasonable accuracy. Consequently, it was found that testing concrete samples in heating regimes based on heat fluxes rather than heating rates offers a marked advantage.

The implementation of genetic algorithm optimization proved invaluable in this work as it was found to be time efficient, cost effective and accurate for practical purposes. The method allowed pinpointing the thermal properties of different intermediate concrete phases which were unknown and thereby made it possible to predict the thermal behavior of concrete. Given the level of accuracy in the measurements and the complexity of the problem, the results were ideal for practical purposes; however it must also be recognized in this regard that the grand scheme of this project has been to only spotlight the competency of the implemented inverse modeling methodology and not merely acquiring optimal agreement with the experimental data obtained at this particular work.

The results from the genetic algorithm optimization scheme were shown to be useful only when they are used in a heating environment pertaining properly to the environment from which they have been extracted. In other words, essential behavioral characteristics must be embedded within the thermal properties, otherwise they will produce erroneous results. Similarly as important, the model may need to be adjusted so that it describes the desired environment more accurately, i.e. several phenomena might need to be added or omitted to account for the deviation from the optimized environment.

In spite of fulfilling its promise, the inverse modeling practice in this work has featured simplified modeling characteristics to only verify the usefulness of the applied methodology and to assess solely the basics of the thermal behavior of concrete. In view of this great scheme, it must be acknowledged that there are various ways to enhance the quality of this practice. The absence of condensation and moisture migration was the primary defect in the basic definition of the utilized Gpyro model which rendered the pressure and gaseous species

evolutions inadequate. Similarly, the inclined readers could further supplement this work by realizing the following modeling or experimental modifications:

➢ First and foremost, the respective evaporation of capillary, gel and free waters must each be accounted for by a separate physical process (or an analogous reaction in Gpyro). Although merging all these phenomena with the decomposition of calcium hydroxide was shown to be workable for a basic assessment, it will be necessary for a more reliable and comprehensive model to account for these processes separately. As it was discussed, this will help reducing the mismatches that are observable in the mass loss rate predictions. Particularly, it is expected that the first evaporation process would be very rapid to better reflect the nonzero nature of the mass loss rate at time t = 0 seconds which was observed in all the experiments (see Figure 14).

➢ The convective heat transfer coefficient changes as the sample gets hot. This could be modelled by several boundary condition lines in Gpyro and changing the heat transfer coefficient progressively.

➢ Thicker concrete samples will enable more comprehensive assessment of the behavior, e.g. 50 to 100mm would be ideal, as more non-uniform evolutions would develop inside the concrete. Larger samples will also make it easier to drill any necessary thermocouples from the sides rather than from the backside.

➢ Re-radiation from the sides needs to be taken into account if the sample is larger.

➢ Although only surface absorption of radiation was considered here, the effects of in-depth radiation absorption may need to be investigated particularly if the samples are thin. This has been found to have significant effects on the pyrolysis of materials which become thermally thin (e.g. for PMMA refer to Bal, 2012).

➢ Should any insulation be provided at the backside of the samples, the presence of thermocouples at the backside could reduce the effectiveness of the provided insulation; therefore it may be beneficial to introduce the thermocouples from the sides.

➢ Achieving more accurate solutions particularly for larger samples would require measurements from more points in the samples since the genetic algorithm optimization can pinpoint ideal solutions only when sufficient number of experimental data sets is available from the different points of the sample.

➢ The number of generations which were simulated here was relatively small as it was only desired to achieve a reasonable reflection; however the results obtained from the genetic algorithm will naturally be more optimal if the number of generations is increased.

➢ An initial time-step size[5] of 0.5 seconds was found to be sufficient to achieve reasonable results in this study; however more accurate solutions would require smaller time-step sizes. This, however, would directly increase the cost of the simulations.

➢ It needs to be assessed how well the cooling of concrete can be modelled using Gpyro.

➢ The different properties of water above its critical point need to be taken into account.

---

[5] Gpyro decreases the size of the time-step automatically if the solution does not converge; however implementation of a larger initial time-step size would decrease the run-times if the solutions converge well.

# References

ASCE. (1992). *ASCE, Structural Fire Protection.* New York, USA: ASCE Committee on Fire Protection, Structural Division, American Society of Civil Engineers.

ASHRAE_Handbook. (2009). Heat transfer (chapter 4, table 5). In *ASHRAE Handbook Fundamentals - IP Edition* (p. 4.13). Atlanta, Nebraska, USA: American Society of Heating, Refrigerating and Air-Conditioning Engineers, Inc.

Bal, N. (2012). *Uncertainty and complexity in pyrolysis modelling (PhD Thesis).* Edinburgh, UK: The University of Edinburgh.

Bažant, Z. P., & Kaplan, M. F. (1996). *Concrete at High Temperatures: Material Properties and Mathematical Models.* London, UK: Longman Group Limited, Essex.

Black box theory (2014, April 16). Retrieved from Wikipedia article *Black box theory*: http://en.wikipedia.org/wiki/Black_box_theory

Bordallo, N. H., Aldridge, L. P., & Desmedt, A. (2006). Water Dynamics in Hardened Ordinary Portland Cement Paste or Concrete: From Quasielastic Neutron Scattering. *The Journal of Physical Chemistry B, Volume 110, Number 36*, 17966-17976.

Campbell-Allen, D., & Thorne, C. P. (1963). The thermal conductivity of concrete. *Magazine of Concrete Research, Volume 15, Issue 43*, 39-48.

Chaube, R., Kishi, T., & Maekawa, K. (1999). Moisture transport in Cementitious materials (Chapter 4). In *Modelling of Concrete Performance: Hydration, Microstructure and Mass Transport* (p. 69). New York, USA: Routledge.

Chung, J. H., Consolazio, G. R., & McVay, M. C. (2006). Finite element stress analysis of a reinforced high-strength concrete column in severe fires. *Computers & Structures, Volume 84, Issue 21*, 1338–1352.

Davie, C. T., Pearce, C. J., & Bicanic, N. (2010). A fully generalised, coupled, multi-phase, hygro-thermo-mechanical model for concrete. *Materials and Structures, Volume 43, Issue 1 Supplement*, 13–33.

Debicki, G., Haniche, R., & Delhomme, F. (2012). An experimental method for assessing the spalling sensitivity of concrete mixture submitted to high temperature. *Cement & Concrete Composites, Volume 34, Issue 8*, 958–963.

Deeny, S., Stratford, T., Dhakal, R., Moss, P., & Buchanan, A. (2009). Spalling of Concrete: Implications for Structural Performance in Fire. *Proceedings of the International Conference Applications of Structural Fire Engineering* (pp. 202-207). Prague, Czech Republic: The University of Edinburgh.

Dougill, J. W. (1961). The effects of thermal incompatibility and shrinkage on the strength of concrete. *Magazine of Concrete Research, Volume 13, Issue 39*, 119–126.

Drysdale, D. (2011). Heat transfer (chapter 2, table 2.7). In D. Drysdale, *Introduction to Fire Dynamics, Third Edition* (p. 62). Scotland, UK: John Wiley & Sons, Ltd.

Dwaikat, M. B., & Kodur, V. K. (2009). Hydrothermal model for predicting fire-induced spalling in concrete structural systems. *Fire Safety Journal, Volume 44, Issue 3*, 425–434.

Ebensperger, L., & Torrent, R. (2010). Medición "in situ" de la permeabilidad al aire del hormigón: status quo. *Revista ingeniería de construcción, Volumen 24, número 3*, 371-382.

EFCAA. (2006). *Air Entraining Admixtures, EFCA Environmental Declaration, EFCA doc.301ETG.* European Federation of Concrete Admixture Associations (EFCAA).

EN1992-1-2. (2004). *EN 1992-1-2: design of concrete structures. Part 1-2: general rules—structural fire design, Eurocode 2.* Brussels, Belgium: European Committee for Standardization.

Feldman, R., & Sereda, P. (1970). A new model for hydrated Portland cement and its practical implications. *Engineering Journal, Volume 53, Issue 8/9*, 53–59.

Fletcher, I. A., Welch, S., Torero, J. L., & Carvel, R. U. (2007). *The Behaviour of Concrete Structures in Fire.* Edinburgh, UK: BRE Research Publications, BRE Centre for Fire Safety Engineering.

Flynn, D. R. (1999). *Response of high performance concrete to fire conditions: review of thermal property data and measurement techniques, NIST GCR 99-767.* Gaithersburg, Maryland, USA: National Institute of Standards and Technology.

Foster, J. A. (2001). Evolutionary computation. *Nature Reviews Genetics, Volume 2, Issue 6*, 428–36.

Franssen, J. M. (2005). SAFIR: a thermal/structural program modelling structures under fire. *Engineering Journal-American Institute of Steel Construction Inc., Volume 42, Issue 3*, 143–158.

Gawin, D., Majorana, C. E., & Schrefler, B. A. (1999). Numerical analysis of hygro-thermal behaviour and damage of concrete at high temperature. *Mechanics of Cohesive-frictional Materials, Volume 4, Issue 1*, 37–74.

Gawin, D., Pesavento, F., & Schrefler, B. A. (2011). What physical phenomena can be neglected when modelling concrete at high temperature? A comparative study. Part 1: Physical phenomena and mathematical model. *International Journal of Solids and Structures, Volume 48, Issue 13*, 1927-1944.

Gawin, D., Pesavento, F., & Schrefler, B. A. (2011). What physical phenomena can be neglected when modelling concrete at high temperature? A comparative study. Part 2: Comparison between models. *International Journal of Solids and Structures, Volume 48, Issue 13*, 1945–1961.

Goldberg, D. (1989). *Genetic Algorithms: In Search, Optimization and Machine Learning.* Boston, Massachusetts, USA: Addison-Wesley Longman Publishing Co., Inc.

Grasberger, S., & Meschke, G. (2000). A hygral-thermal-poroplastic damage model for the durability analyses of concrete structures. *CD-ROM Proceedings (Eds. Oniate, E.; Bugeda, G. & Suárez, G.; ECCOMAS), European Congress on Computational Methods in Applied Science Engineering* (p. 18). Barcelona, Spain: ECCOMAS.

Harada, T., Takeda, J., Yamane, S., & Furumura, F. (1972). Strength, elasticity and thermal properties of concrete subjected to elevated temperatures. *ACI Concrete For Nuclear Reactor SP, Volume 34, Issue 2*, 377–406.

Harmathy, T. Z. (1970). Thermal properties of concrete at elevated temperatures. *Journal of Materials, Volume 5, Issue 1*, 47-74.

Harmathy, T. Z., & Allen, L. (1973). Thermal properties of selected masonry unit concretes. *Journal American Concrete Institution, Voume 70, Issue 2*, 132–142.

Hawileh, R. A., Naser, M., Zaidan, W., & Rasheed, H. A. (2009). Modeling of insulated CFRP-strengthened reinforced concrete T-beam exposed to fire. *Engineering Structures, Volume 31, Issue 12*, 3072–3079.

Ichikawa, Y., & England, G. L. (2004). Prediction of moisture migration and pore pressure build-up in concrete at high temperatures. *Nuclear Engineering and Design, Volume 228, Issues 1–3*, 245–259.

ISO5660-1:2002(E). (2002). *Reaction-to-fire tests — Heat release, smoke production and mass loss rate — Part 1: Heat release rate (cone calorimeter method).* Geneva, Switzerland: International Organization for Standardization.

Kalifa, P., Menneteau, F.-D., & Quenard, D. (2000). Spalling and pore pressure in HPC at high temperatures. *Cement and Concrete Research, Volume 30, Issue 12*, 1915–1927.

Karhunen, K. (2013). *Electrical Resistance Tomography Imaging of Concrete (Ph.D. Thesis).* Kuopio, Finland: Dissertations in Forestry and Natural Sciences, Issue 122, the University of Eastern Finland.

Khaliq, W. (2012). *Performance characterization of high performance concretes under fire conditions (Ph.D. thesis).* Michigan, US: Michigan State University.

Khan, M. I. (2002). Factors affecting the thermal properties of concrete and applicability of its prediction models. *Building and Environment, Volume 37*, 607-614.

Khan, M. I., & Bhattacharjee, B. (1995). Relationship between thermal conductivities of aggregate and concrete. *In: Reddy RR, Editor, Civil engineering materials and structures, Osmania University Hyderabad, India*, 162-166.

Khoury, G. A. (2000). Effect of fire on concrete and concrete structures. *Progress in Structural Engineering and Materials, Volume 2, Issue 4*, 429-447.

Khoury, G. A. (2008). Polypropylene fibres in heated concrete. Part 2: Pressure relief mechanisms and modelling criteria. *Magazine of Concrete Research, Volume 60, Number 3*, 189–204.

Khoury, G. A., Majorana, C. E., Pesavento, F., & Schrefler, B. A. (2002). Modelling of heated concrete. *Magazine of Concrete Research, Volume 54, Issue 2*, 77–101.

Kodur, V. (2014). Review Article: Properties of Concrete at Elevated Temperatures. *ISRN Civil Engineering, Volume 2014, Article ID 468510, 15 pages*.

Kodur, V. R., & Harmathy, T. Z. (2008 ). Properties of building materials. In P. J. DiNenno, *SFPE Handbook of Fire Protection Engineering* (pp. 1–155 to 1–181). Quincy, Mass, USA: National Fire Protection Association.

Kodur, V. R., & Sultan, M. A. (1998). Thermal propeties of high strength concrete at elevated temperatures. *American Concrete Institute, Special Publication, SP-179*, 467–480.

Kumar, R., & Bhattacharjee, B. (2003). Porosity, pore size distribution and in situ strength of concrete. *Cement and Concrete Research, Volume 33, Issue 1*, 155–164.

Kurtis, D. K. (2010). *Cement and Hydration (Civil Engineering Notes).* Atlanta, Georgia, USA: School of Civil Engineering, Georgia Institute of Technology Atlanta.

Lautenberger, C. W. (2007). *A Generalized Pyrolysis Model for Combustible Solids (PhD Thesis).* Berkeley, California, USA: University of California, Berkeley.

Lautenberger, C. W. (2009). *Gpyro – A Generalized Pyrolysis Model for Combustible Solids (Technical Reference, Version 0.700).* Berkeley, California, USA: Chris Lautenberger, 63 Hesse Hall, Department of Mechanical Engineering, University of California, Berkeley.

Lautenberger, C. W. (2009). *Gpyro – A Generalized Pyrolysis Model for Combustible Solids (Users' Guide, Version 0.700).* Berkeley, California, USA: Chris Lautenberger, 63 Hesse Hall, Department of Mechanical Engineering, University of California, Berkeley.

Li, Z. (2011). In *Advanced Concrete Technology* (pp. 1-22). Hoboken, New Jersey: John Wiley & Sons, Inc.

Lie, T. T., & Kodur, V. K. (1996). Thermal and mechanical properties of steel-fibre-reinforced concrete at elevated temperatures. *Canadian Journal of Civil Engineering, Volume 23, Issue 2*, 511–517.

Lim, L., Buchanan, A., Moss, P., & Franssen, J.-M. (2004). Numerical modelling of two-way reinforced concrete slabs in fire. *Engineering Structures, Volume 26, Issue 8*, 1081–1091.

Lin, W.-M., Lin, T. D., & Powers-Couche, L. J. (1996). Microstructures of Fire-Damaged Concrete. *ACI Materials Journal, Volume 93, Issue 3*, 199–205.

Majorana, C., Salomoni, V., Mazzuccoa, G., & Khoury, G. (2010). An approach for modelling concrete spalling in finite strains. *Mathematics and Computers in Simulation, Volume 80, Issue 8*, 1694–1712.

Marshall, A. (1972). The thermal properties of concrete. *Building Science, Volume 7, Issue 3*, 167-174.

Mehta, P. K., & Monteiro, P. J. (2006). *Concrete: microstructure, properties, and materials.* McGraw-Hill.

Meyer-Ottens, C. (1974). *Abplatzversuche an Pruefkoerpern aus Beton, Stahlbeton, und Spannbeton bei verschiedenen Temperaturebeanspruchungen.* Berlin, Germany: Schriftenreihe des Deutschen Ausschusses fuer Stahlbeton.

Mikhail, R. S., Brunauer, S., & Copeland, L. E. (1965). Kinetics Of The Thermal Decomposition Of Calcium Hydroxide. *Journal of Colloid and Interface Science, Volume 9, Issue 1*, 394–404.

Nevile, A. (1995). *Properties of Concrete.* UK: Longman.

Ozawa, M., Uchida, S., Kamada, T., & Morimoto, H. (2012). Study of mechanisms of explosive spalling in high-strength concrete at high temperatures using acoustic emission. *Construction and Building Materials, Volume 37*, 621–628.

Peltier, J. (2014, April 18). *LOESS Utility.* Retrieved from Peltier Tech Blog, Peltier Tech Excel Charts and Programming (Peltier Technical Services, Inc.): http://peltiertech.com/WordPress/loess-utility-awesome-update/

Peng, G. F., Chan, S. Y., & Anson, M. (2001). Chemical kinetics of C-S-H decomposition in hardened cement paste subjected to elevated temperatures up to 800°C. *Advances in Cement Research, Volume 13, Issue 2*, 47–52.

Rein, G., Lautenberger, C. W., Fernandez-Pello, C., Torero, J. L., & Urban, D. L. (2006). Application of genetic algorithms and thermogravimetry to determine the kinetics of polyurethane foam in smoldering combustion. *Combustion and Flame, Volume 146, Issues 1–2*, 95–108.

Schroeder, R. A. (1999). *Post-Fire Analysis of Construction Materials (Ph.D. Thesis).* Berkeley, California: University of California, Berkeley.

Shin, K. Y., Kim, S. B., Kim, J. H., Chung, M., & Jung, P. S. (2002). Thermo-physical properties and transient heat transfer of concrete at elevated temperatures. *Nuclear Engineering and Design, Volume 212, Issue 1–3*, 233–241.

Stabler, J. T. (2000 ). *Computational modelling of thermo-mechanical damage and plasticity in concrete (Ph.D. thesis).* Brisbane, Australia: The University of Queensland.

Tenchev, R. T., & Purkiss, L. Y. (2001). Finite element analysis of coupled heatand moisture transfer in concrete subjected to fire. *Numerical Heat Transfer Applications, Volume 39, Issue 7*, 685–710.

Tenchev, R., & Purnell, P. (2005). An application of a damage constitutive model to concrete at high temperature and prediction of spalling. *International Journal of Solids and Structures, Volume 42, Issue 26*, 6550–6565.

The Secretary of State of United Kingdom. (2007). *Approved Document B, UK Building Regulations.* The Building Regulations 2000, England and Wales.

The_Engineering_ToolBox. (2014, April 21). *Emissivity Coefficients of some common Materials*. Retrieved from The Engineering ToolBox.com: http://www.engineeringtoolbox.com/emissivity-coefficients-d_447.html

Ulm, F., Coussy, O., & Bazant, Z. (1999). The "Chunnel" Fire. I: Chemoplastic Softening in Rapidly Heated Concrete. *Journal of Engineering Mechanics, Volume 125, Number 3*, 272–282.

USBR. (1940). *Thermal properties of concrete.* Boulder Canyon Project Report, Final Report by USBR, Bulletin Number 1, Part VII.

Vangeem, M. G., Holm, T. A., & Ries, J. P. (2013). Optimal Thermal Mass and R-value in Concrete. *First International Conference on Concrete Sustainability*, (pp. 411-418). Tokyo, Japan.

Wadsö, L., Karlsson, J., & Tammo, K. (2012). *Thermal properties of concrete with various aggregates.* Lund, Sweden: Manuscript draft to Elsevier Editorial System(tm) for Cement and Concrete Research, Lund University.

Zhang, H. L., & Davie, C. T. (2013). A numerical investigation of the influence of pore pressures and thermally induced stresses for spalling of concrete exposed to elevated temperatures. *Fire Safety Journal, Volume 59*, 102–110.

Zhang, Q., & Ye, G. (2012). Dehydration kinetics of Portland cement paste at high temperature. *Journal of Thermal Analysis and Calorimetry*, 153–158.

# Appendices

The following appendices comprise, respectively, the Gpyro issues which were addressed or still persisted after this work, an organized assembly of all the obtained experimental and modeling results, and ultimately the template of the ASCII input files which were used in the simulation practices.

## A.1. Addressed and persisting Gpyro issues

The main addressed issues can be summarized as follows[6]:

- ➢ 2D optimization of mass loss rates (MLR) and the corresponding cumulative mass loss (CML) was enabled.
- ➢ The definitions of MLR and CML were corrected for 2D and the extraction of these quantities was improved in accord with the functioning of the pressure solver for 1D to 3D simulations.
- ➢ Optimization of conductivity and permeability as well as their nonlinear temperature dependency were enabled in y- and z- directions for different condensed phases.
- ➢ A more systematic optimization routine was introduced to enable isotropic optimization of conductivity and permeability as well as their nonlinear temperature dependency for different condensed phases.
- ➢ The handling of mass transfer coefficients and gaseous species diffusion were upgraded.
- ➢ The definition of profile outputs as well as 2D Smokeview output slices was improved and made consistent to enable easier dumping.
- ➢ More constructive error messages were made available in order for easier diagnosis of the existing mismatches in the boundary conditions, the optimization coordinates, the output dump locations, as well as other under-/over-specifications of the model.

---

[6] The details of these issues and how they evolved can be tracked via the ticket system built into the REAXEngineering wiki at http://reaxengineering.com/trac/gpyro/report.

The main persisting issues can also be summarized as follows:

➢ Condensation remains fragile as there is a need for systematic implementation of reaction CHI values and densities of the involved condensed phases in order to conserve the mass. Liquid mass transfer has been also mostly overlooked and needs more serious advancements.

➢ A more systematic optimization of the density of the condensed phases and their nonlinear temperature dependency is needed to enable the optimizer to zero in on the optimal solution more efficiently.

➢ Designation of surface geometries and their according boundary conditions needs to be made consistent. Such designations implement inconsistent definitions of z-direction which needs to be harmonized with the conventional direction of 'z' (i.e. increasing by elevation from the ground surface). This has to do with the coupling between Gpyro and FDS.

# A.2. Complete results

## A.2.1. Experimental results

Overall, the experimental findings consist of the mass loss rates, the cumulative mass losses and the distributions of through-thickness temperatures which were obtained via the primary and replicate experiments. First, the mass loss rates and the cumulative mass losses are presented through Figures 30 to 33 then the temperature evolutions are presented through Figures 34 to 38.

Although the key results were already presented in Section 3.1, they are repeated here for the sake of completeness (apart from the findings about the free water content of the oven-dried sample which was presented in Table 7).
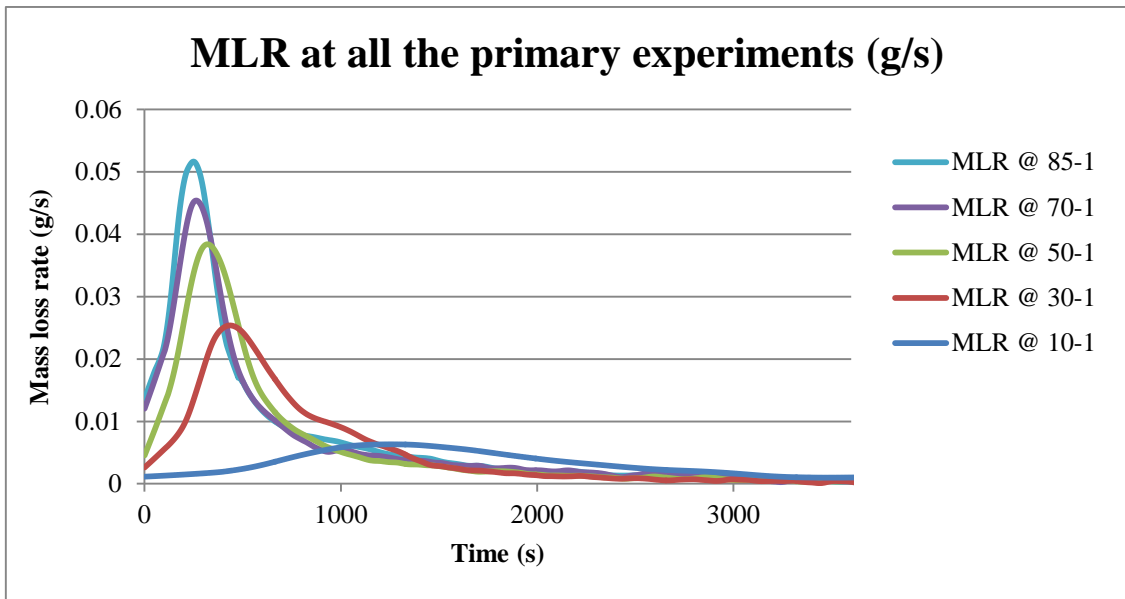
**Figure 30.** Mass loss rates measured at different heat flux levels during the primary experiments: the mass loss rates have been determined using the five-point numerical differentiation method suggested by ISO 5660-1 document for cone calorimetry (ISO5660-1:2002(E), 2002) and were normalized using LOESS Utility (Peltier, 2014). The overall loss of mass in each experiment was calibrated so that it matched the value measured in the experiment.
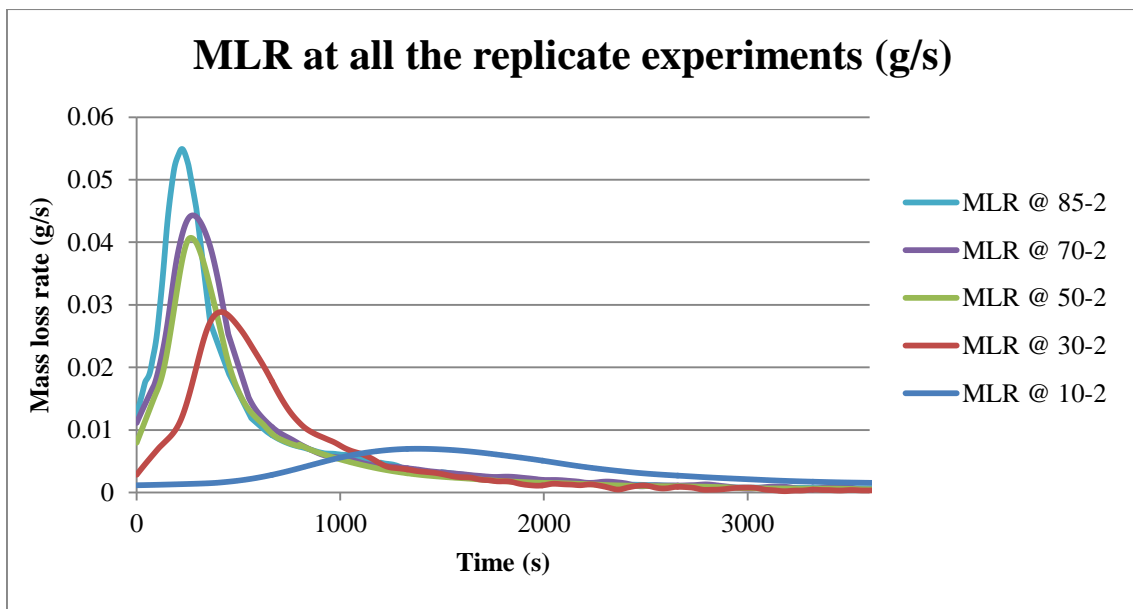


**Figure 31.** Mass loss rates measured at different heat flux levels during the replicate experiments: the mass loss rates have been determined using the five-point numerical differentiation method suggested by ISO 5660-1 document for cone calorimetry (ISO5660-1:2002(E), 2002) and were normalized using LOESS Utility (Peltier, 2014). The overall loss of mass in each experiment was calibrated so that it matched the value measured in the experiment. The worst repeatability corresponds to the replicate experiment at 50 kW/m² (i.e. MLR@50-2).
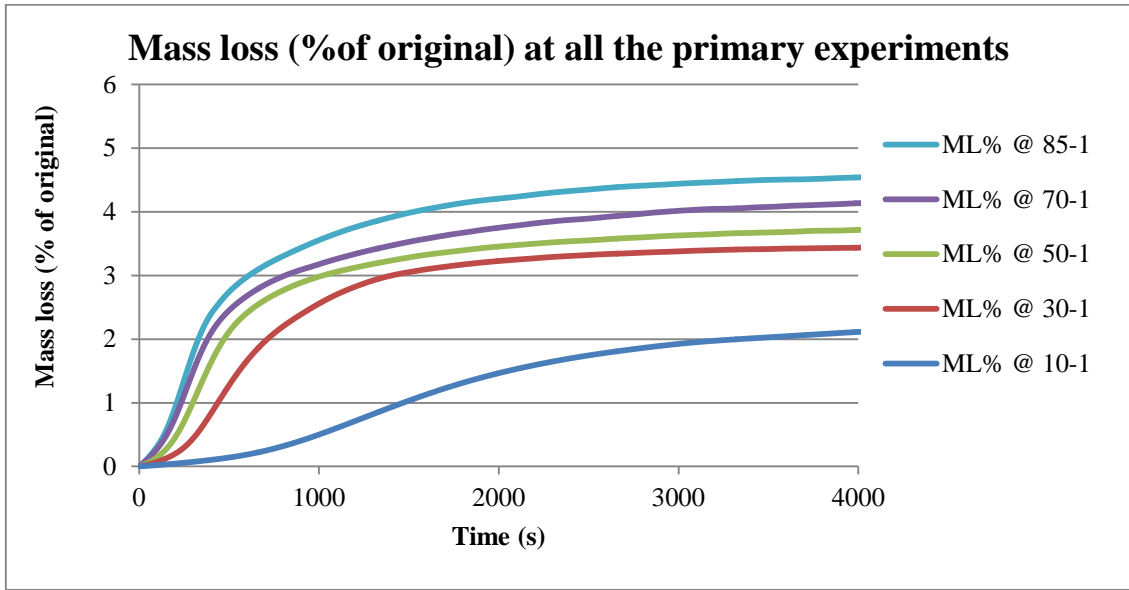
**Figure 32. Mass loss (% of original) at different heat flux levels during the primary experiments: the cumulative mass loss has been calculated from the normalized mass loss rate data.**
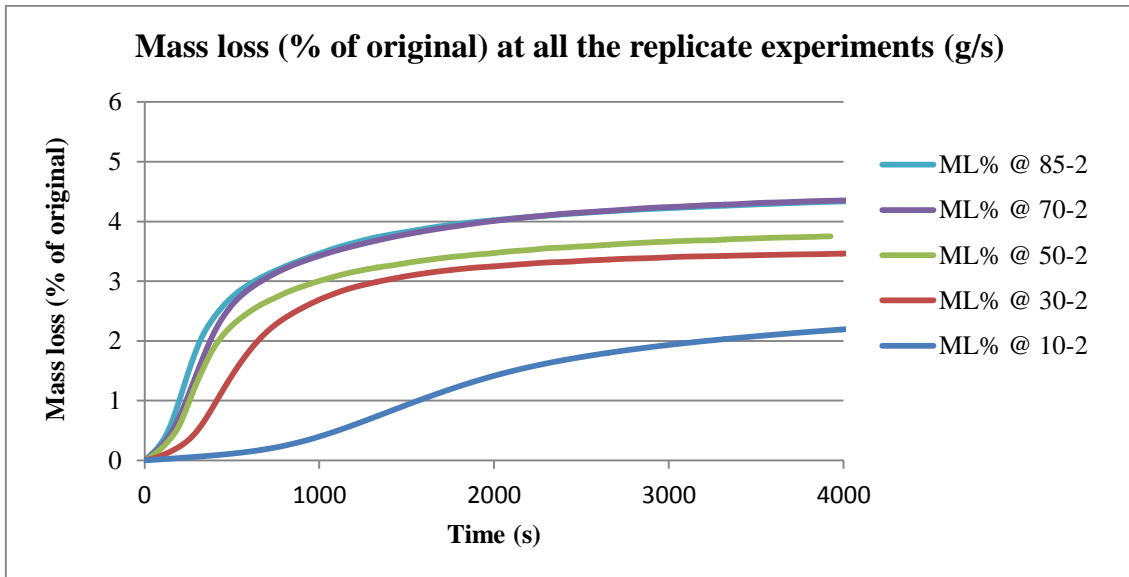


**Figure 33. Mass loss (% of original) at different heat flux levels during the replicate experiments: the cumulative mass loss has been calculated from the normalized mass loss rate data. Note that here the ML% @ 85-2 curve has matched the ML% @ 70-2 curve. This is because the original mass of the specimen at MLR@85-2 was higher than the other specimen.**
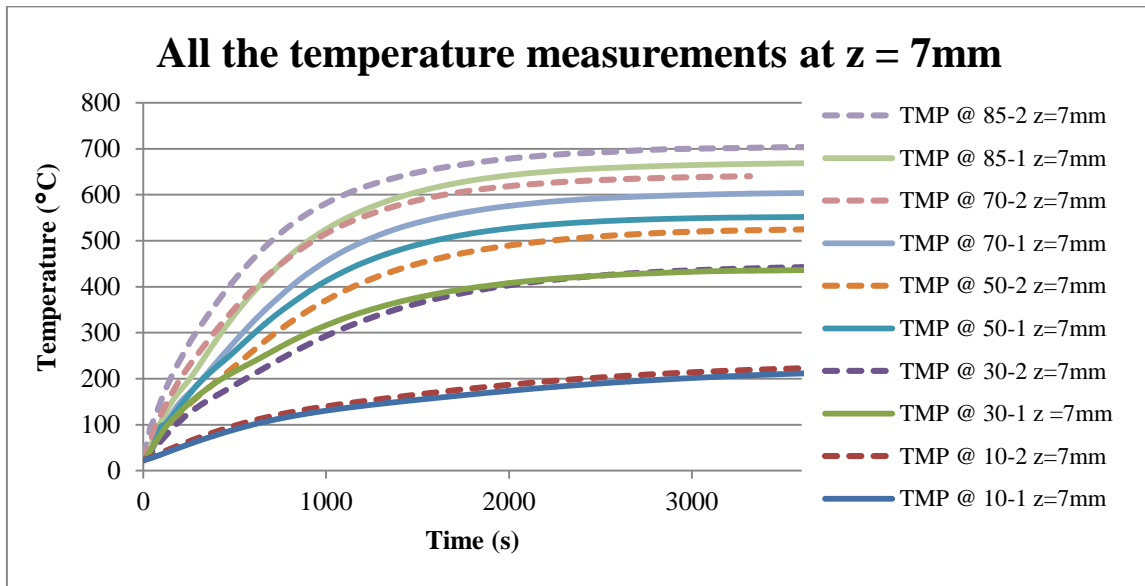
**Figure 34.** Temperature measurements at 7mm from the surface for the replicate (broken) and the primary experiments (solid) during the first hour of heating: all the replicate experiments consistently indicate slightly higher temperatures than the primary experiments except the replicate experiment TMP@50-2 which crosses over its counterpart.
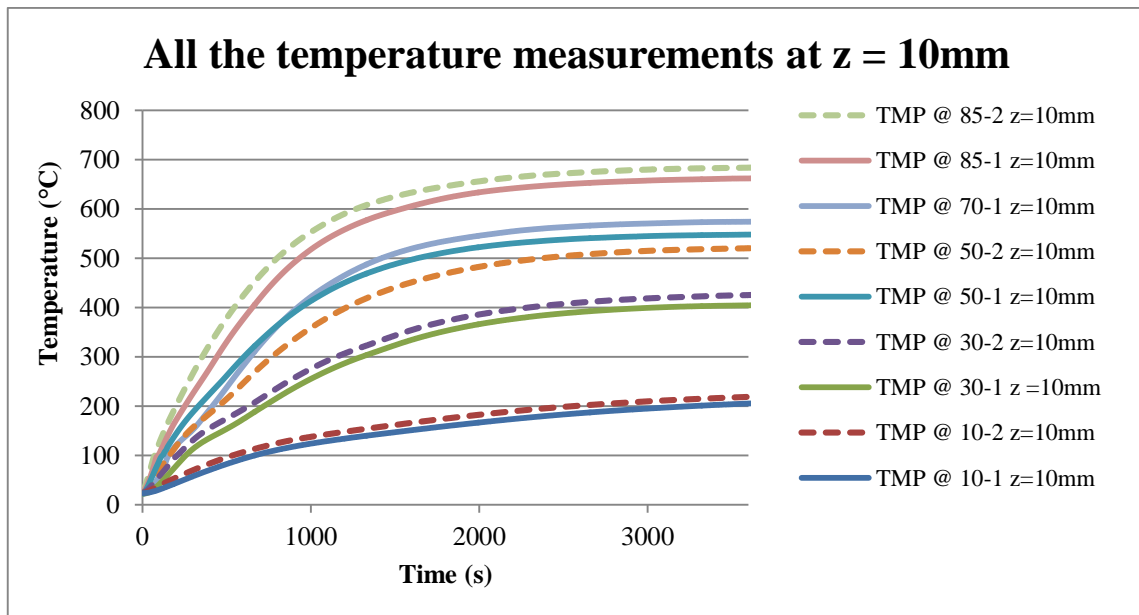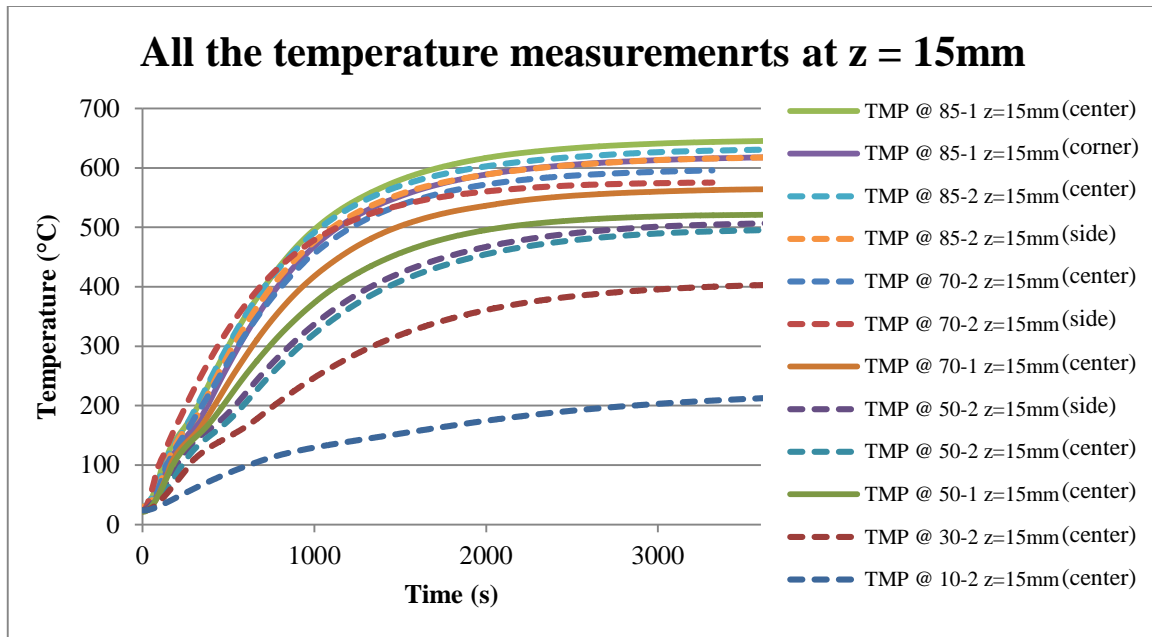


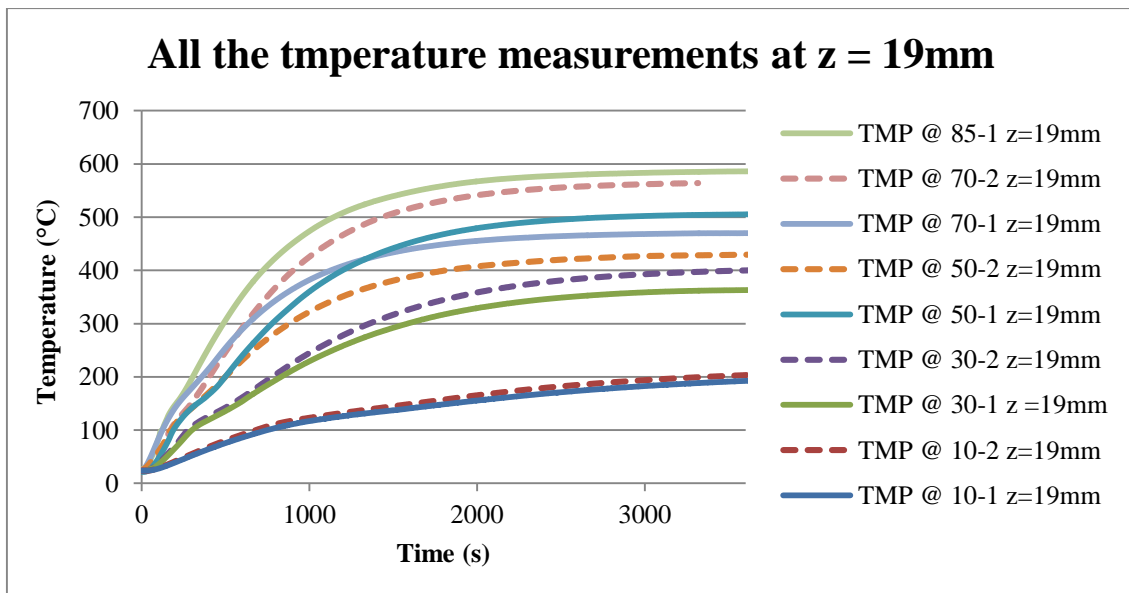**Figure 35.** Temperature measurements at 10mm from the surface for the replicate (broken) and the primary experiments (solid) during the first hour of heating: all the replicate experiments consistently reveal slightly higher temperatures than the primary experiments except the replicate experiment TMP@50-2 which crosses over its counterpart. Temperature at z = 10mm was not measured at the replicate experiment TMP@70-2.

**Figure 36. Temperature measurements at 15mm from the surface for the replicate (broken) and the primary experiments (solid) during the first hour of heating.**



**Figure 37. Temperature measurements at 19mm from the surface for the replicate (broken) and the primary experiments (solid) during the first hour of heating: the replicate experiments habitually indicate slightly higher temperatures than the primary experiments; although two outliers exist at this particular depths (z = 19mm), namely the readings from the replicate experiment TMP@50-2 and the primary experiment TMP@70-1 which not only cross over their counterparts but also do not accord with the temperature evolution of the lower heat fluxes. The temperature at z = 19mm was not measured at the replicate experiment TMP@85-2.**
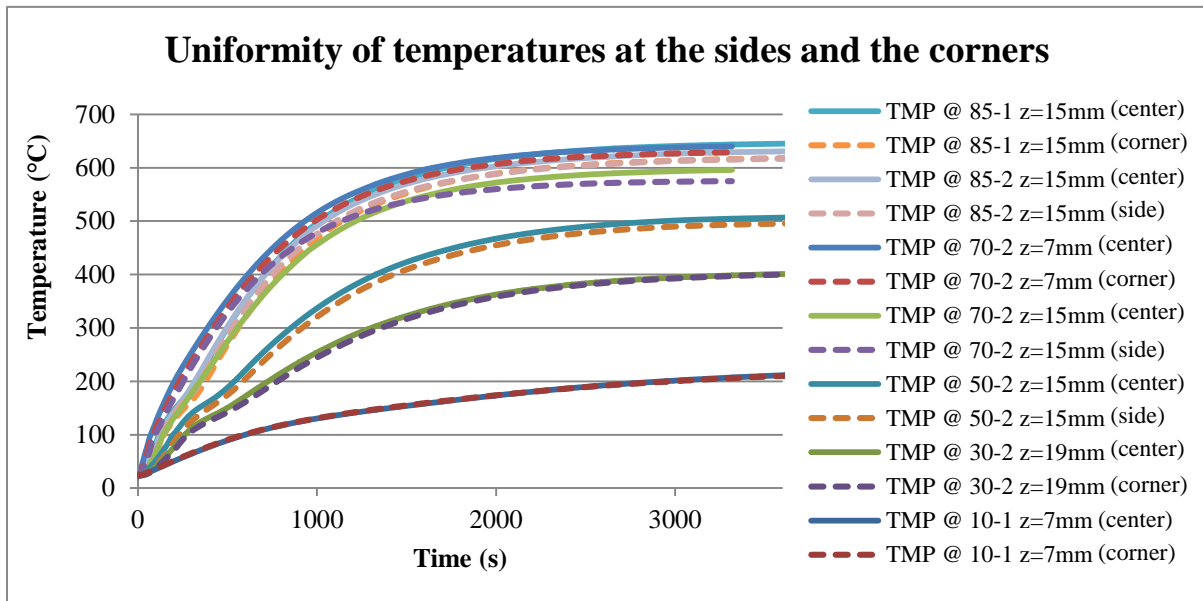
**Figure 38.** Uniformity of temperature distributions at the sides and at the corners compared to the center for various experiments: temperature distributions at the sides and at the corners (broken) match suitably with the corresponding distributions at the center (solid) thus majorly 1D behavior prevails.

# A.2.2. Modeling results

The findings from the modeling and the inverse modeling simulations consist of the simulated mass loss rates, the cumulative mass losses, the distributions of through-thickness temperatures, as well as the evolutions of pressure and gaseous species for each primary experiment. Additionally, optimized simulation results from each experiment were used to replicate the experiments at other heat flux levels. Moreover, simulations of experiments at 10 and 30 kW/m$^2$ were performed once with the first dehydration reaction only and once with both of the dehydration reactions.

As the inclusive scope of the modeling results is exhaustive and too much to be included in this document, only examples of the characteristic parts of the modeling results are presented here and the comprehensive scope is covered in the CD accompanying this thesis. Hence, an example of the simulated temperature evolutions is first provided in Figure 39 then the mass loss rates and the cumulative mass losses are presented through Figures 40 to 41. Ultimately, all the main simulated temperature distributions are presented through Figures 42 to 49.
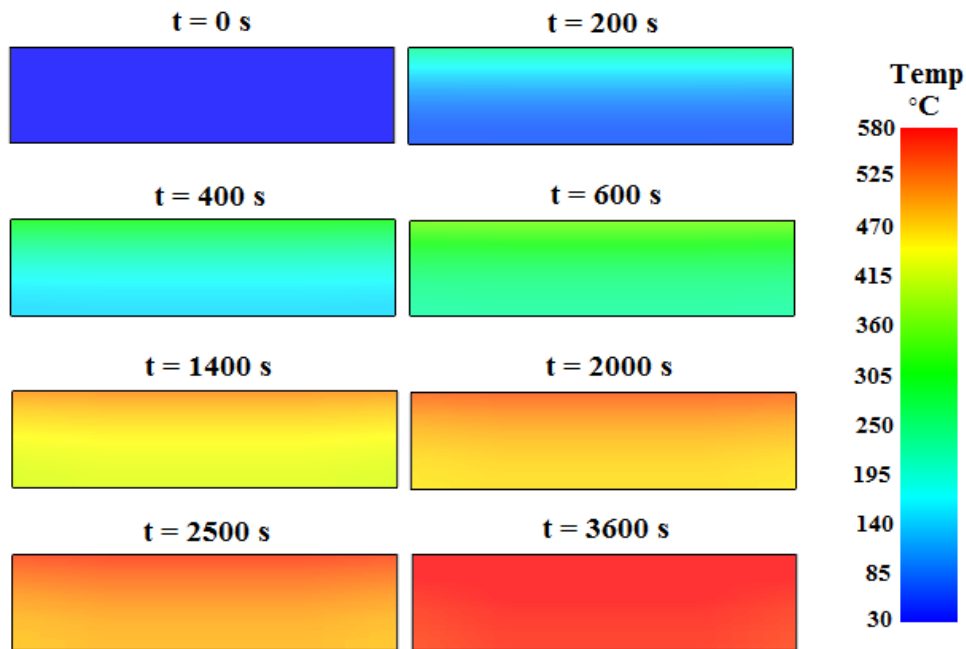
**Figure 39. An example of the simulated temperature evolution within the concrete samples (from the simulation of experiments at 50 kW/m²): as the sample is heated from above, the temperatures begin to rise from the surface downwards until they eventually become more or less uniform. The nature of the distributions is only slightly 2D since the difference between the convective heat transfer coefficient at the sides and at the top of the sample was not substantial, i.e. 8 versus 11 kW/m².K. Even so, the upper center part of the sample is always hotter than any other locations in the sample which verifies that the 2D evolution of temperatures is modelled correctly.**
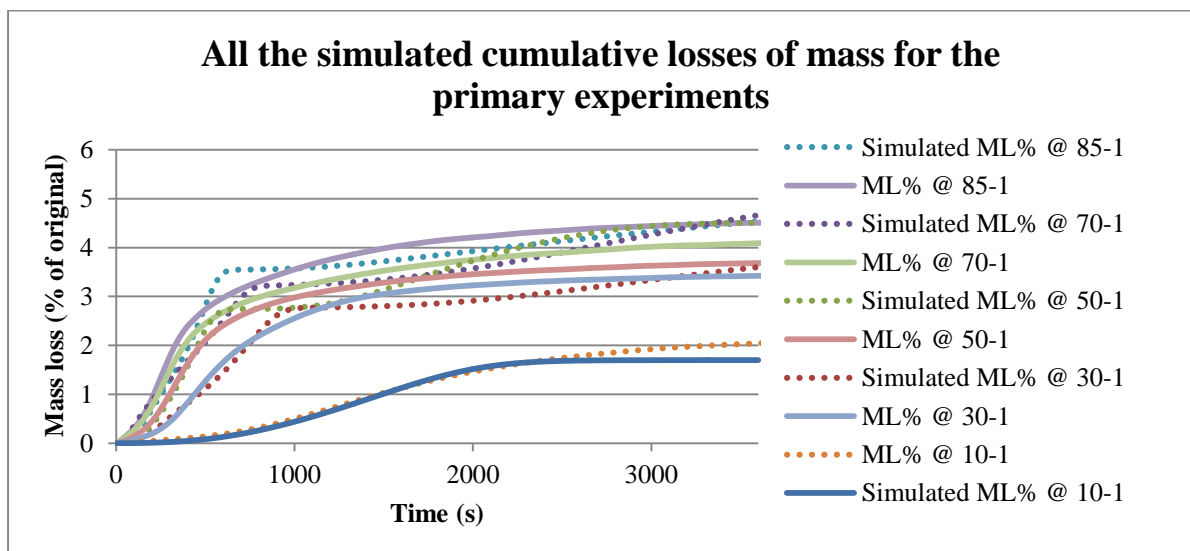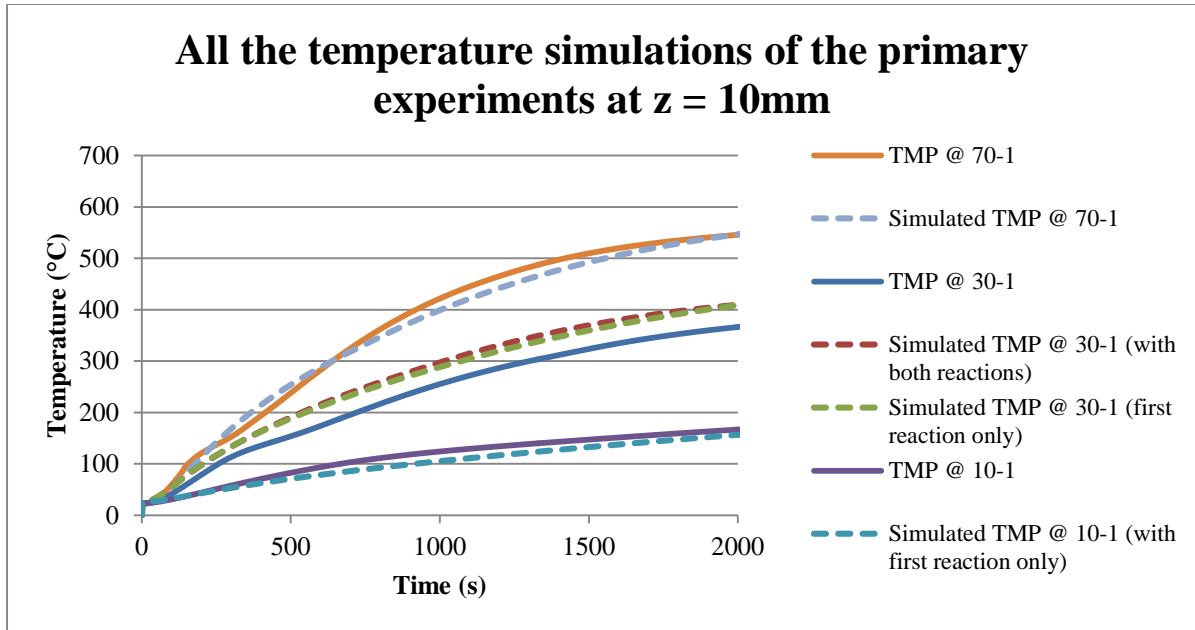


**Figure 40. All the simulations of cumulative losses of mass along with their experimental counterparts: the disagreements in the cumulative losses of mass are much less pronounced than the mismatches that exist in the simulations of mass loss rates (see Figure 41). Typically, the ultimate cumulative mass losses have been overestimated while the overall agreement is satisfactory.**
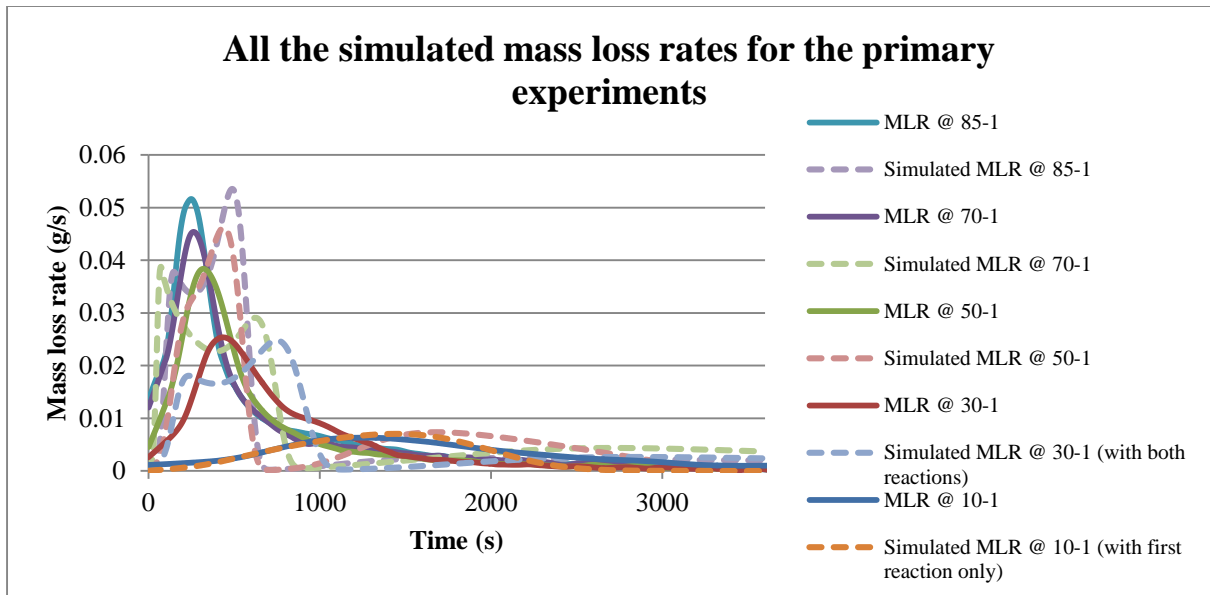
**Figure 41. Simulated mass loss rates for all the primary experiments along with their experimental counterparts: solid curves display the experiments and the broken curves indicate the corresponding simulations. The optimized mass loss rate curves from all the simulations majorly underestimate the rise and the peak of mass loss rates while they overestimate the rates elsewhere. Only the simulation of experiments at 50 kW/m² overestimates the peak mass loss rate from the corresponding experiment.**
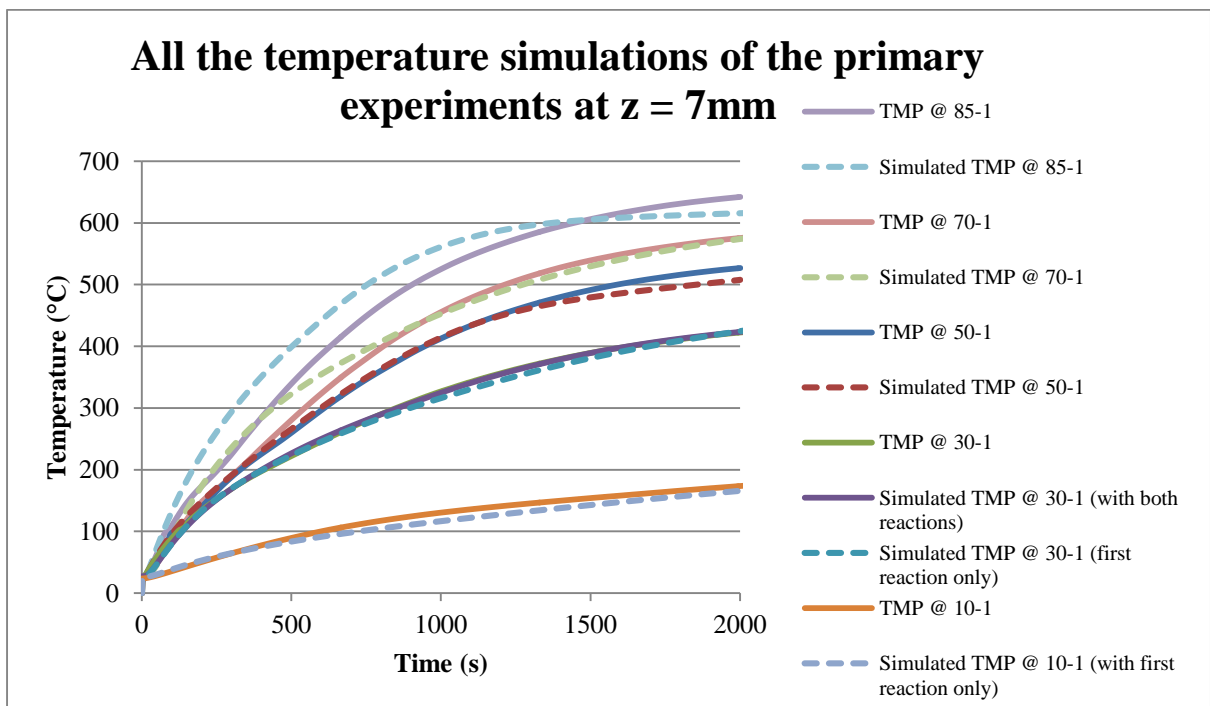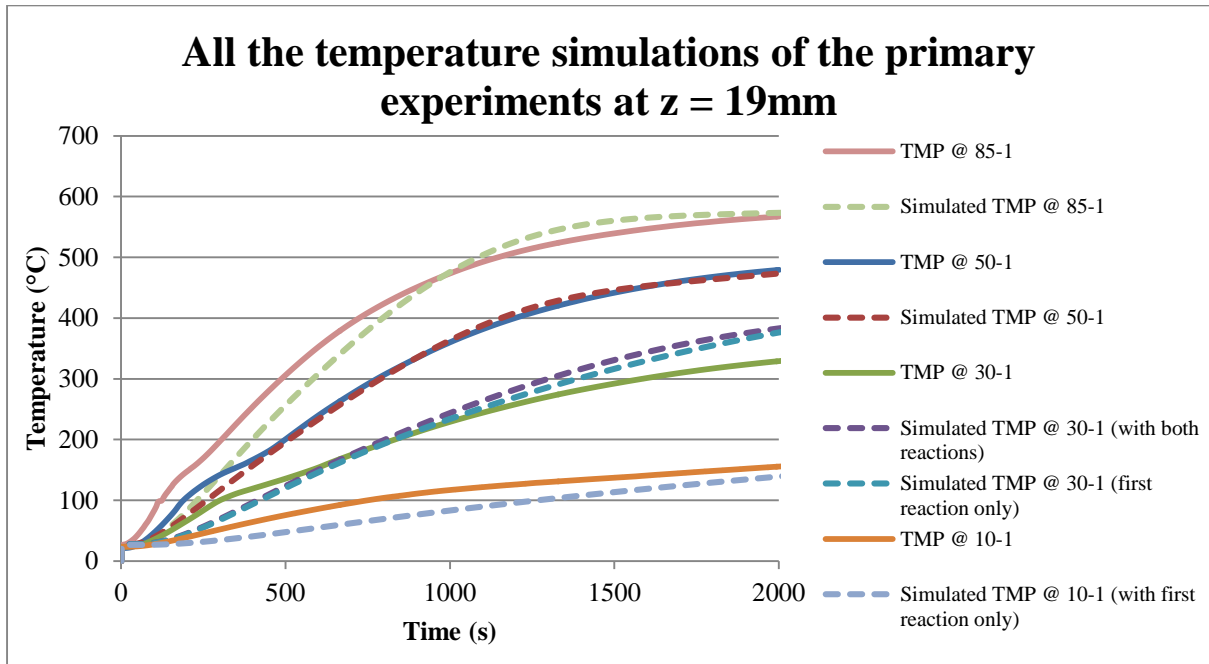


**Figure 42. The temperature simulations of all the primary experiments at z = 7mm along with their experimental counterparts: temperature distributions are satisfactory; although a better optimization would naturally be possible using higher numbers of generations.**
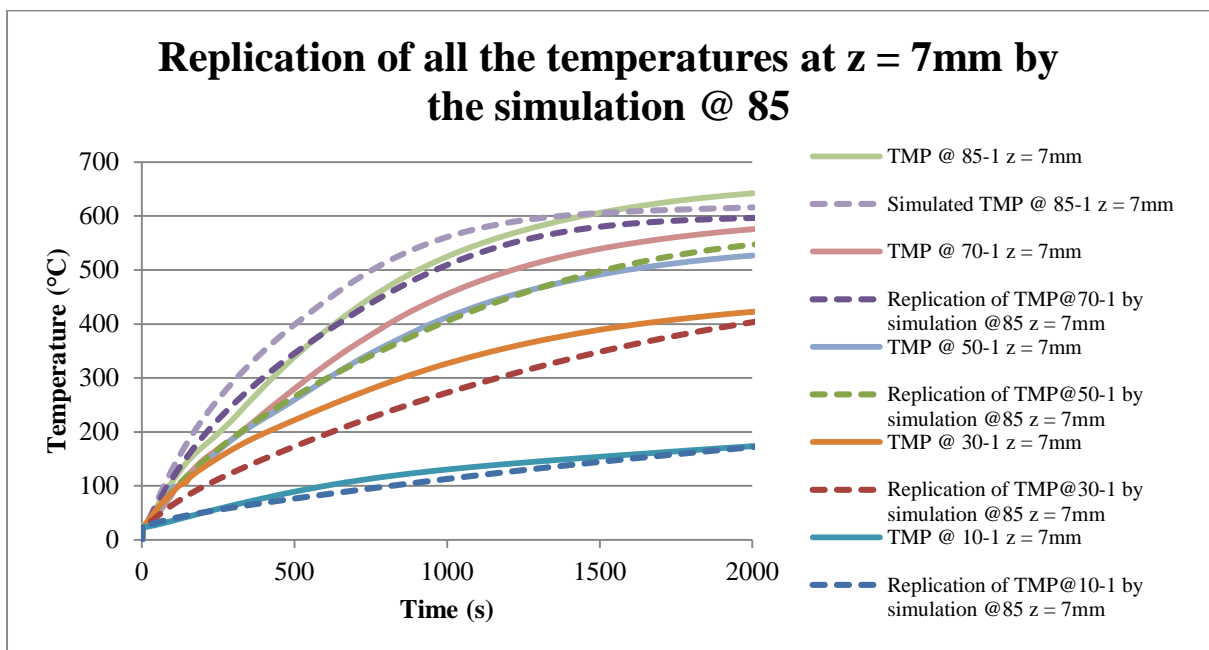
**Figure 43.** The temperature simulations of all the primary experiments at z = 10mm along with their experimental counterparts: the simulated distributions match the experimental measurements adequately except the simulation of experiments at 30 kW/m² which overestimates the corresponding experimentally measured values. Temperature at z = 10mm from experiment TMP@50-1 had been recognized as outlier earlier and it was not used.
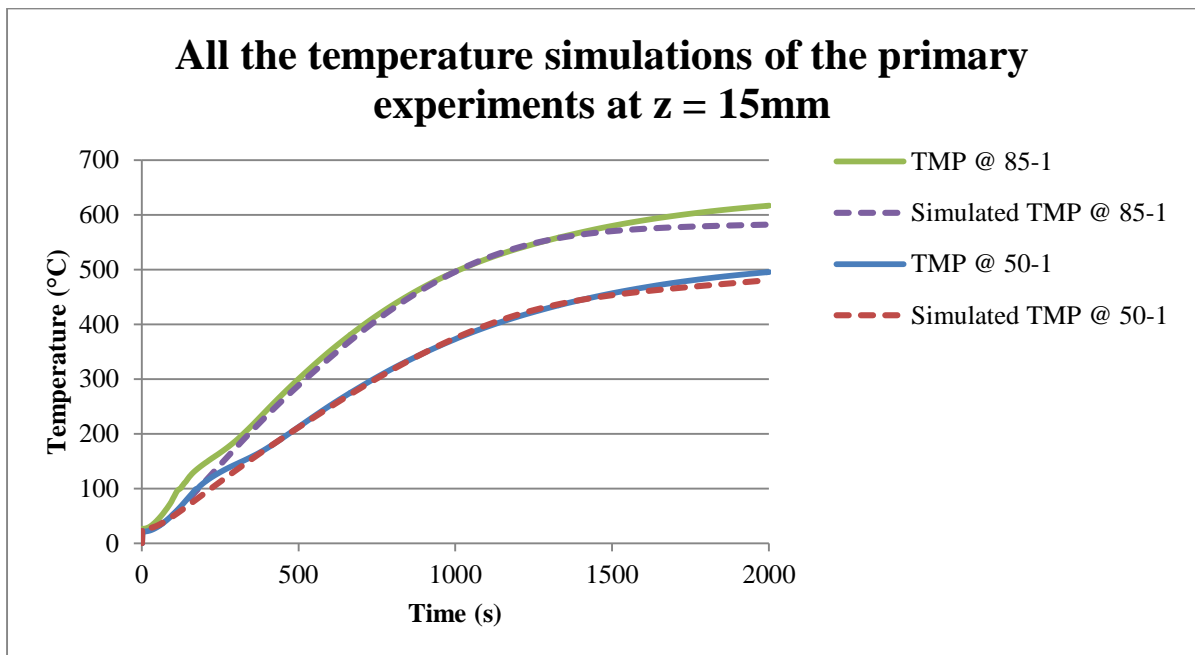


**Figure 44.** The temperature simulations of all the primary experiments at z = 15mm along with their experimental counterparts: although the overall trend is reflected accurately, the ultimate trend has diverged from the experimentally obtained distributions. This is mainly because the optimization was performed with the expressive portion of the distributions only, i.e. if the optimizer is provided with the full distribution, the ultimate trend would be reflected accurately. Temperature at z = 15mm from experiment TMP@70-1 had been recognized as outlier earlier and it was not used. Temperature at this depth was also not measured in experiments TMP@30-1 and TMP@10-1.
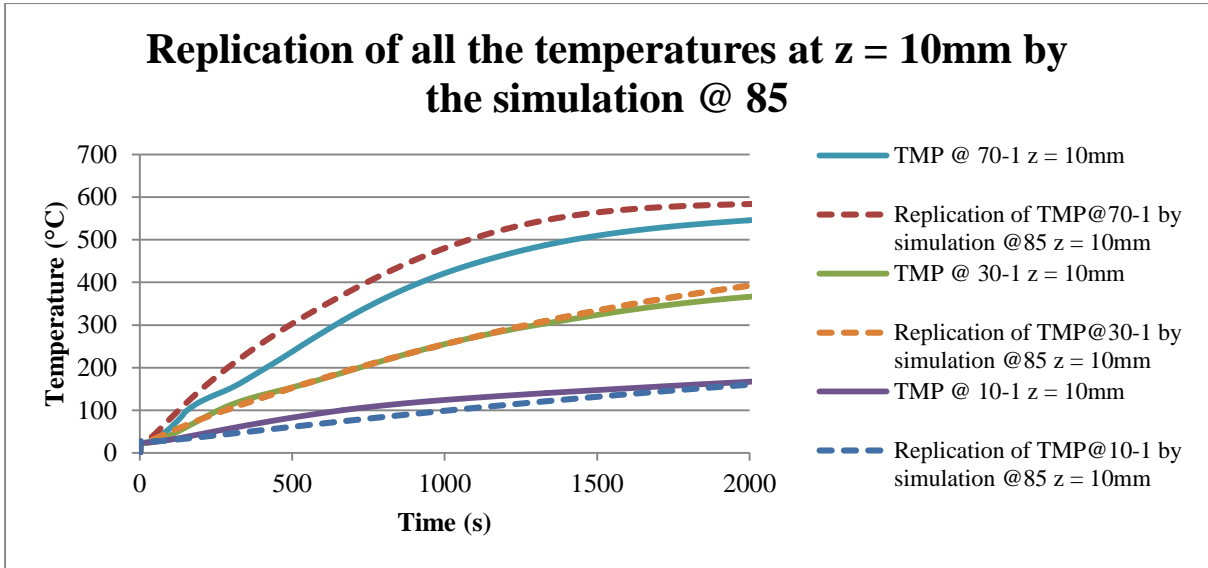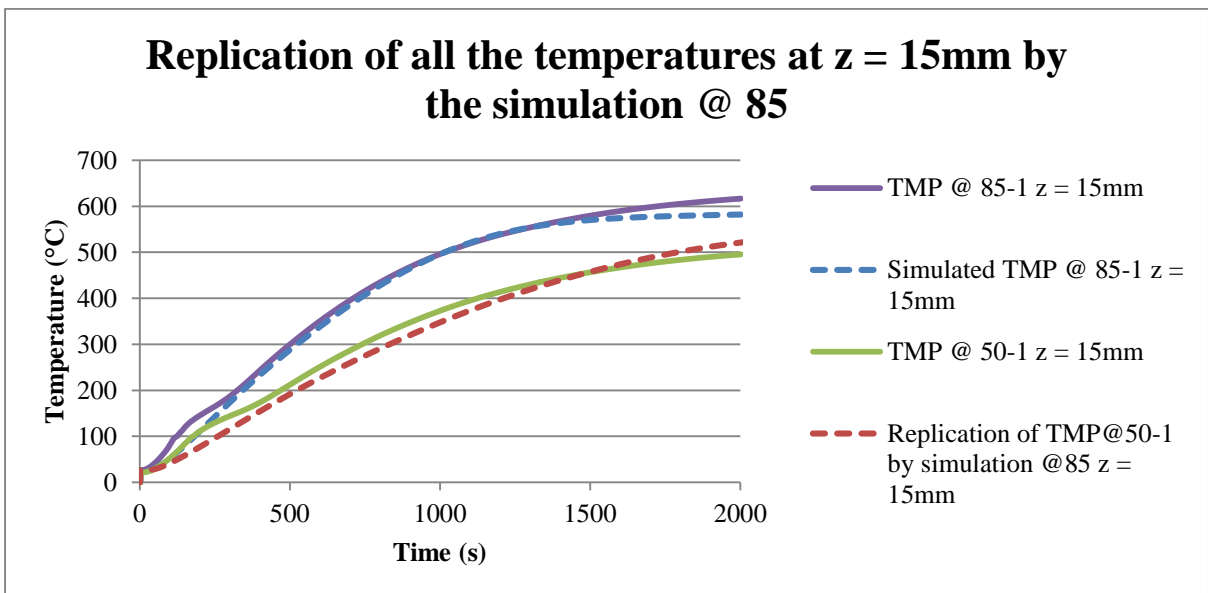
**Figure 45.** The temperature simulations of all the primary experiments at z = 19mm along with their experimental counterparts: the overall reflection is satisfactory; although the simulations of experiments at 10 and 30 kW/m² need better convergence. Temperature at z = 19mm from experiment TMP@70-1 had been recognized as outlier earlier and it was not used.



**Figure 46.** Replicated temperature evolutions at z = 7mm for all the primary experiments obtained using the simulation of experiments at 85 kW/m² along with the corresponding experimental measurements: much opposed to the replicated mass loss rates (as shown in **Figure 27** from the same simulation), the accuracy of the temperature distributions do not generally worsen in replications at low heat flux levels. The predicted temperature distributions for experiments at 50 and 10 kW/m² are almost ideal in fact.

**Figure 47.** Replicated temperature evolutions at z = 10mm for all the primary experiments obtained using the simulation of experiments at 85 kW/m² along with the corresponding experimental measurements: temperature evolutions have mostly been replicated well; although a better convergence is needed in case of the distribution predicted for the TMP@70-1. Temperature at z = 10mm from experiment TMP@50-1 had been recognized as outlier earlier and it was not used.



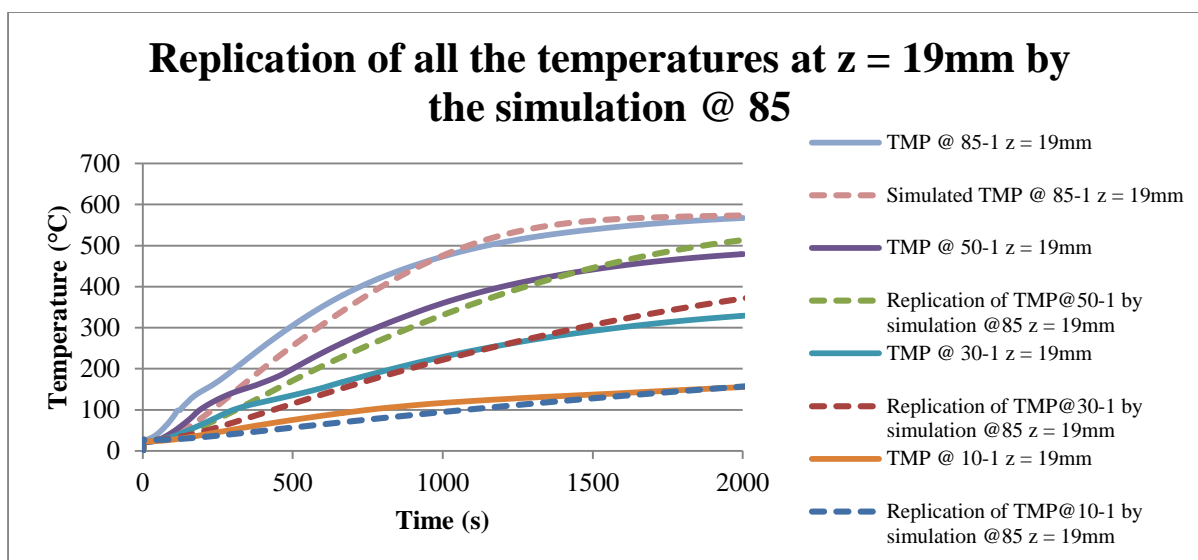**Figure 48.** Replicated temperature evolutions at z = 15mm for all the primary experiments obtained using the simulation of experiments at 85 kW/m² along with the corresponding experimental measurements: the replicated distribution for TMP@50-1 has been impressive; although the ultimate trend needs better accuracy (refer to the explanations for Figure 44). Temperature at z = 15mm from experiment TMP@70-1 had been recognized as outlier earlier and it was not used. Temperature at this depth was also not measured in experiments TMP@30-1 and TMP@10-1.

**Figure 49. Replicated temperature evolutions at z = 19mm for all the primary experiments obtained using the simulation of experiments at 85 kW/m² along with the corresponding experimental measurements: temperature evolutions have mostly been replicated reasonably; although a the ultimate trends of the distributions corresponding to TMP@50-1 and TMP@30-1 need better reflection (refer to the explanations for Figure 44). Temperature at z = 19mm from experiment TMP@70-1 had been recognized as outlier earlier and it was not used.**

# A.3. Template of the ASCII input files

The main modeling assumptions and characteristics have already been explained in Section 2.2 and also in Table 1; nevertheless, the following template script presents inner details of the models as outlined in the ASCII input files. This script is the input file for modelings relating to experiments at 85 kW/m² and is identical to the input files used for the other experiments except in a few places, namely the radiative heat flux level in the boundary conditions patch (&GPYRO_ALLBC); the periods of simulations in the cases patch (&GPYRO_CASES); and the location and the number of optimization points in the &GPYRO_PHI patch. In the simulations relating to experiments at 10 and 30 kW/m², the number of reactions and condensed phases were changed as well to investigate the effects of including/excluding the decomposition of calcium silicate hydroxides phase. The experimental data files which accompanied the ASCII input files in the simulations were also specific to the experiment which was simulated.

The template script is as followed below:

```
&GPYRO_GENERAL
DT0 = 0.5,
TAMB = 300,
TREF = 300,
P0 = 101300,
GX = 0,
GZ = 0,
GY = 0,
THERMAL_EQUILIBRIUM = .TRUE.,
VHLC = 0,
HCV = 1000000,
NU_A = 2,
NU_B = 1,
NU_C = 0.5,
NTDMA_ITERATIONS = 500,
NSSPECIESITERNS = 1,
NCONTINUITYITERNS = 1,
ALPHA = 1,
TMPTOL = 0.01,
HTOL = 0.00000001,
YITOL = 0.001,
PTOL = 0.01,
YJTOL = 0.001,
HGTOL = 0.1,
EXPLICIT_T = .FALSE.,
SOLVE_GAS_YJ = .TRUE.,
SOLVE_GAS_ENERGY = .FALSE.,
SOLVE_PRESSURE = .TRUE.,
USE_TOFH_NEWTON = .FALSE.,
SHYI_CORRECTION = .TRUE.,
NCOEFF_UPDATE_SKIP = 1,
FDSMODE = .FALSE.,
CONVENTIONAL_RXN_ORDER = .FALSE.,
NOCONSUMPTION = .FALSE.,
EPS = 0.0000000001,
BLOWING = .FALSE.,
MINIMUM_CONDUCTIVITY = 0,
CONSTANT_DHVOL = .TRUE.,
FULL_QSG = .FALSE.,
GASES_PRODUCED_AT_TSOLID = .FALSE.,
 /

&GPYRO_OUTPUT
CASENAME = 'gpyro',
N_POINT_QUANTITIES = 1,
N_PROFILE_QUANTITIES = 8,
N_SMOKEVIEW_QUANTITIES = 8,
DTDUMP_GA = 1,
DTDUMP_POINT = 1,
DTDUMP_PROFILE = 1,
DTDUMP_SMOKEVIEW = 1,
TMP_REDUCED_DTDUMP = 5000,
REDUCED_DTDUMP = 0.0001,
DTMIN_KILL = 0.0000001,
POINT_QUANTITY(1) = 'MLR',
POINT_QUANTITY_INDEX(1) = 0,
POINT_IMESH(1) = 0,
POINT_Z(1) = 0,
POINT_X(1) = 0,
POINT_Y(1) = 0,
PROFILE_QUANTITY(1) = 'TEMPERATURE',
PROFILE_QUANTITY_INDEX(1) = 0,
PROFILE_DIRECTION(1) = 'z',
PROFILE_IMESH(1) = 1,
PROFILE_COORD1(1) = 0.05,
PROFILE_COORD2(1) = 0,
PROFILE_ISKIP(1) = 1,
PROFILE_QUANTITY(2) = 'PRESSURE',
PROFILE_QUANTITY_INDEX(2) = 0,
PROFILE_DIRECTION(2) = 'z',
PROFILE_IMESH(2) = 1,
```

```
PROFILE_COORD1(2) = 0.05,
PROFILE_COORD2(2) = 0,
PROFILE_ISKIP(2) = 1,
PROFILE_QUANTITY(3) = 'YI',
PROFILE_QUANTITY_INDEX(3) = 1,
PROFILE_DIRECTION(3) = 'z',
PROFILE_IMESH(3) = 1,
PROFILE_COORD1(3) = 0.05,
PROFILE_COORD2(3) = 0,
PROFILE_ISKIP(3) = 1,
PROFILE_QUANTITY(4) = 'YI',
PROFILE_QUANTITY_INDEX(4) = 2,
PROFILE_DIRECTION(4) = 'z',
PROFILE_IMESH(4) = 1,
PROFILE_COORD1(4) = 0.05,
PROFILE_COORD2(4) = 0,
PROFILE_ISKIP(4) = 1,
PROFILE_QUANTITY(5) = 'YI',
PROFILE_QUANTITY_INDEX(5) = 3,
PROFILE_DIRECTION(5) = 'z',
PROFILE_IMESH(5) = 1,
PROFILE_COORD1(5) = 0.05,
PROFILE_COORD2(5) = 0,
PROFILE_ISKIP(5) = 1,
PROFILE_QUANTITY(6) = 'YJ',
PROFILE_QUANTITY_INDEX(6) = 1,
PROFILE_DIRECTION(6) = 'z',
PROFILE_IMESH(6) = 1,
PROFILE_COORD1(6) = 0.05,
PROFILE_COORD2(6) = 0,
PROFILE_ISKIP(6) = 1,
PROFILE_QUANTITY(7) = 'YJ',
PROFILE_QUANTITY_INDEX(7) = 2,
PROFILE_DIRECTION(7) = 'z',
PROFILE_IMESH(7) = 1,
PROFILE_COORD1(7) = 0.05,
PROFILE_COORD2(7) = 0,
PROFILE_ISKIP(7) = 1,
PROFILE_QUANTITY(8) = 'YJ',
PROFILE_QUANTITY_INDEX(8) = 3,
PROFILE_DIRECTION(8) = 'z',
PROFILE_IMESH(8) = 1,
PROFILE_COORD1(8) = 0.05,
PROFILE_COORD2(8) = 0,
PROFILE_ISKIP(8) = 1,
SMOKEVIEW_QUANTITY(1) = 'TEMPERATURE',
SMOKEVIEW_QUANTITY_INDEX(1) = 0,
SMOKEVIEW_PLANE(1) = 'xz',
SMOKEVIEW_IMESH(1) = 1,
SMOKEVIEW_LOCATION(1) = 0,
SMOKEVIEW_QUANTITY(2) = 'PRESSURE',
SMOKEVIEW_QUANTITY_INDEX(2) = 0,
SMOKEVIEW_PLANE(2) = 'xz',
SMOKEVIEW_IMESH(2) = 1,
SMOKEVIEW_LOCATION(2) = 0,
SMOKEVIEW_QUANTITY(3) = 'YI',
SMOKEVIEW_QUANTITY_INDEX(3) = 1,
SMOKEVIEW_PLANE(3) = 'xz',
SMOKEVIEW_IMESH(3) = 1,
SMOKEVIEW_LOCATION(3) = 0,
SMOKEVIEW_QUANTITY(4) = 'YI',
SMOKEVIEW_QUANTITY_INDEX(4) = 2,
SMOKEVIEW_PLANE(4) = 'xz',
SMOKEVIEW_IMESH(4) = 1,
SMOKEVIEW_LOCATION(4) = 0,
SMOKEVIEW_QUANTITY(5) = 'YI',
SMOKEVIEW_QUANTITY_INDEX(5) = 3,
SMOKEVIEW_PLANE(5) = 'xz',
SMOKEVIEW_IMESH(5) = 1,
SMOKEVIEW_LOCATION(5) = 0,
SMOKEVIEW_QUANTITY(6) = 'YJ',
```

SMOKEVIEW_QUANTITY_INDEX(6) = 1,
SMOKEVIEW_PLANE(6) = 'xz',
SMOKEVIEW_IMESH(6) = 1,
SMOKEVIEW_LOCATION(6) = 0,
SMOKEVIEW_QUANTITY(7) = 'YJ',
SMOKEVIEW_QUANTITY_INDEX(7) = 2,
SMOKEVIEW_PLANE(7) = 'xz',
SMOKEVIEW_IMESH(7) = 1,
SMOKEVIEW_LOCATION(7) = 0,
SMOKEVIEW_QUANTITY(8) = 'YJ',
SMOKEVIEW_QUANTITY_INDEX(8) = 3,
SMOKEVIEW_PLANE(8) = 'xz',
SMOKEVIEW_IMESH(8) = 1,
SMOKEVIEW_LOCATION(8) = 0,
 /

&GPYRO_SPROPS
NSSPEC = 3,
NAME(1) = 'original_concrete',
K0Z(1) = 2.20440812,
NKZ(1) = -0.0251434789,
R0(1) = 2264.77966,
NR(1) = -0.0118217046,
C0(1) = 1644.63637,
NC(1) = 0.0241430933,
EMIS(1) = 0.867174735,
KAPPA(1) = 9D9,
TMELT(1) = 3000,
DHMELT(1) = 0,
SIGMA2MELT(1) = 0,
GAMMA(1) = 0,
PERMZ(1) = 6.62286537E-16,
RS0(1) = 2787.17259,
PORE_DIAMETER(1) = 0.0000690205273,
K0X(1) = 2.20440812,
NKX(1) = -0.0251434789,
PERMX(1) = 6.62286537E-16,
K0Y(1) = 2.20440812,
NKY(1) = -0.0251434789,
PERMY(1) = 6.62286537E-16,
NAME(2) = 'dehydrated_concrete1',
K0Z(2) = 2.15188992399533,
NKZ(2) = 0,
R0(2) = 2186.25917619855,
NR(2) = -0.017124054,
C0(2) = 1738.67506589296,
NC(2) = 0.028883995,
EMIS(2) = 0.909624578,
KAPPA(2) = 9D9,
TMELT(2) = 3000,
DHMELT(2) = 0,
SIGMA2MELT(2) = 0,
GAMMA(2) = 0,
PERMZ(2) = 3.56470811724999E-12,
RS0(2) = 2688.77719492407,
PORE_DIAMETER(2) = 7.13106925849044E-05,
K0X(2) = 2.15188992399533,
NKX(2) = 0,
PERMX(2) = 3.56470811724999E-12,
K0Y(2) = 2.15188992399533,
NKY(2) = 0,
PERMY(2) = 3.56470811724999E-12,
NAME(3) = 'dehydrated_concrete2',
K0Z(3) = 2.08411773247819,
NKZ(3) = -0.0271600907,
R0(3) = 2154.89200850007,
NR(3) = -0.0281708649,
C0(3) = 1841.05301774242,
NC(3) = 0.0204723536,
EMIS(3) = 0.830100882,
KAPPA(3) = 9D9,

```
TMELT(3) = 3000,
DHMELT(3) = 0,
SIGMA2MELT(3) = 0,
GAMMA(3) = 0,
PERMZ(3) = 4.49509216516389E-12,
RS0(3) = 2613.78104703541,
PORE_DIAMETER(3) = 7.33732024761475E-05,
K0X(3) = 2.08411773247819,
NKX(3) = -0.0271600907,
PERMX(3) = 4.49509216516389E-12,
K0Y(3) = 2.08411773247819,
NKY(3) = -0.0271600907,
PERMY(3) = 4.49509216516389E-12,
 /

&GPYRO_RXNS
NRXNS = 2,
CFROM(1) = 'original_concrete' ,
CTO(1) = 'dehydrated_concrete1' ,
Z(1) = 97016.9126404737 ,
E(1) = 69.7535675 ,
DHS(1) = 0 ,
DHV(1) = 100 ,
CHI(1) = 1 ,
ORDER(1) = 0.991800922 ,
ORDERO2(1) = 0 ,
IKINETICMODEL(1) = 0 ,
IO2TYPE(1) = 0 ,
M(1) = 0 ,
KCAT(1) = 0 ,
ICAT(1) = 0 ,
CFROM(2) = 'dehydrated_concrete1' ,
CTO(2) = 'dehydrated_concrete2' ,
Z(2) = 12659229.9870956 ,
E(2) = 180 ,
DHS(2) = 0 ,
DHV(2) = 86885154.9561017 ,
CHI(2) = 1 ,
ORDER(2) = 1.15351022 ,
ORDERO2(2) = 0 ,
IKINETICMODEL(2) = 0 ,
IO2TYPE(2) = 0 ,
M(2) = 0 ,
KCAT(2) = 0 ,
ICAT(2) = 0 ,
 /

&GPYRO_HGRXNS
NHGRXNS = 0,
 /

&GPYRO_GPROPS
NGSPEC = 3,
IBG = 1,
IO2 = 2,
CPG = 1860,
NAME(1) = 'water_vapor' ,
M(1) = 18 ,
SIGMA(1) = 3 ,
EPSOK(1) = 144 ,
C0(1) = 1000 ,
NC(1) = 0 ,
NAME(2) = 'oxygen' ,
M(2) = 32 ,
SIGMA(2) = 3.464 ,
EPSOK(2) = 106.7 ,
C0(2) = 1000 ,
NC(2) = 0 ,
NAME(3) = 'nitrogen' ,
M(3) = 28 ,
SIGMA(3) = 3.798 ,
```

```
EPSOK(3) = 71.4 ,
C0(3) = 1000 ,
NC(3) = 0 ,
 /

&GPYRO_GYIELDS
GYIELDS(1,1) = 1,
GYIELDS(1,2) = 1,
GYIELDS(2,1) = 0,
GYIELDS(2,2) = 0,
GYIELDS(3,1) = 0,
GYIELDS(3,2) = 0,
 /

&GPYRO_HGYIELDS
 /

&GPYRO_CASES
NCASES = 1,
IMESH(1) = 1,
TSTOP(1) = 3600,
ZEROD(1) = .FALSE.,
BETA(1) = 5,
 /

&GA_GENINPUT NGEN = 200,
NINDIV = 1000,
MAXCOPIES = 10,
SIMULATED_EXPERIMENTAL_DATA = .FALSE.,
RESTART = .FALSE.,
FITMIN = 0,
FITCLIP = 0,
FITEXPONENT = 2,
WHOLEGENEFRAC = 0.8,
BRUTE_FORCE = .FALSE.,
KILL_NONCONVERGED_SOLNS = .TRUE.,
ASA = 1,
BSA = 20,
OPTIMIZATION_TYPE = 'GA',
ISOTROPIC_THERMAL_CONDUCTIVITY = .TRUE.,
ISOTROPIC_PERMEABILITY = .TRUE.,
DUMP_INTERMEDIATE_TRIALS = .FALSE.,
DUMP_ALL_RESULTS_BEST = .TRUE.,
MAXN = 1000000,
KSTOP = 100,
PCENTO = 0.00001,
NGS = 16,
ISEED = 1969,
NPG = 39,
NPS = 20,
NSPL = 39,
MINGS = 16,
NOPT = 19,
 /
&GPYRO_IC
NIC = 1,
TMP_INITIAL(1) = 300,
TMPG_INITIAL(1) = 300,
P_INITIAL(1) = 101300,
YI0(1,1) = 1,
YI0(1,2) = 0,
YI0(1,3) = 0,
YJ0(1,1) = 0.01,
YJ0(1,2) = 0.23,
YJ0(1,3) = 0.76,
 /

&GPYRO_ALLBC
NSURF_IDX = 4,
SURF_IDX(1) = 1,
T(1) = 0,
```

```
QE(1) = 0,
HC(1) = 8,
NHC(1) = 0,
TINF(1) = 300,
RERADIATION(1) = .FALSE.,
TFIXED(1) = -1,
MDOTPP(1) = 0,
PRES(1) = -1000,
QEG(1) = 0,
HCG(1) = 8,
TINFG(1) = 300,
TFIXEDG(1) = -1000,
HM(1) = 0,
YJINF(1,1) = 0,
YJINF(1,2) = 0.23,
YJINF(1,3) = 0.77,
SURF_IDX(2) = 2,
T(2) = 0,
QE(2) = 0,
HC(2) = 8,
NHC(2) = 0,
TINF(2) = 300,
RERADIATION(2) = .FALSE.,
TFIXED(2) = -1,
MDOTPP(2) = 0,
PRES(2) = -1000,
QEG(2) = 0,
HCG(2) = 8,
TINFG(2) = 300,
TFIXEDG(2) = -1000,
HM(2) = 0,
YJINF(2,1) = 0,
YJINF(2,2) = 0.23,
YJINF(2,3) = 0.77,
SURF_IDX(3) = 3,
T(3) = 0,
QE(3) = 0,
HC(3) = 1,
NHC(3) = 0,
TINF(3) = 300,
RERADIATION(3) = .FALSE.,
TFIXED(3) = -1,
MDOTPP(3) = 0,
PRES(3) = -1000,
QEG(3) = 0,
HCG(3) = 1,
TINFG(3) = 300,
TFIXEDG(3) = -1000,
HM(3) = 0,
YJINF(3,1) = 0,
YJINF(3,2) = 0.23,
YJINF(3,3) = 0.77,
SURF_IDX(4) = 4,
T(4) = 0,
QE(4) = 85000,
HC(4) = 11,
NHC(4) = 0,
TINF(4) = 300,
RERADIATION(4) = .TRUE.,
TFIXED(4) = -1,
MDOTPP(4) = 0,
PRES(4) = 101300,
QEG(4) = 85000,
HCG(4) = 11,
TINFG(4) = 300,
TFIXEDG(4) = -1000,
HM(4) = 0,
YJINF(4,1) = 1,
YJINF(4,2) = 0,
YJINF(4,3) = 0,
 /
```

```
&GPYRO_GEOM
NMESH = 1,
NOBST = 0,
ZDIM(1) = 0.025,
NCELLZ(1) = 26,
XDIM(1) = 0.1,
NCELLX(1) = 3,
YDIM(1) = 0.1,
NCELLY(1) = 1,
GEOMETRY_FILE(1) = 'null',
DEFAULT_SURF_IDX(1,1) = 1,
DEFAULT_SURF_IDX(1,2) = 2,
DEFAULT_SURF_IDX(1,3) = 0,
DEFAULT_SURF_IDX(1,4) = 0,
DEFAULT_SURF_IDX(1,5) = 4,
DEFAULT_SURF_IDX(1,6) = 3,
DEFAULT_IC(1) = 1,
OFFSETZ(1) = 0,
OFFSETX(1) = 0,
OFFSETY(1) = 0,
 /

&GA_PHI
NPHI = 5,
ICASE(1) = 1,
CTYPE(1) = 'TMP',
XT(1) = 0.05,
YT(1) = 0,
ZT(1) = 0.007,
TSTOP(1) = 3600,
PHI(1) = 1,
EPS(1) = 0.05,
ICASE(2) = 1,
CTYPE(2) = 'TMP',
XT(2) = 0.05,
YT(2) = 0,
ZT(2) = 0.015,
TSTOP(2) = 3600,
PHI(2) = 1,
EPS(2) = 0.05,
ICASE(3) = 1,
CTYPE(3) = 'TMP',
XT(3) = 0.05,
YT(3) = 0,
ZT(3) = 0.019,
TSTOP(3) = 3600,
PHI(3) = 1,
EPS(3) = 0.05,
ICASE(4) = 1,
CTYPE(4) = 'MLR',
XT(4) = 0,
YT(4) = 0,
ZT(4) = 0,
TSTOP(4) = 3600,
PHI(4) = 1,
EPS(4) = 0.05,
ICASE(5) = 1,
CTYPE(5) = 'CML',
XT(5) = 0,
YT(5) = 0,
ZT(5) = 0,
TSTOP(5) = 3600,
PHI(5) = 1,
EPS(5) = 0.05,
 /

&GA_VARS
NGENE = 47,
SHEET_NAME(1) = 'sprops',
I1(1) = 1,
```

```
I2(1) = 0,
VAR_TYPE(1) = 'K0Z',
MINVAL(1) = 0.5,
MAXVAL(1) = 3,
USE_LOG(1) = .FALSE.,
PMUT(1) = 0.03,
VMUTMAX(1) = 1,
IVARPAIR(1) = 0,
SHEET_NAME(2) = 'sprops',
I1(2) = 1,
I2(2) = 0,
VAR_TYPE(2) = 'NKZ',
MINVAL(2) = -0.05,
MAXVAL(2) = 0,
USE_LOG(2) = .FALSE.,
PMUT(2) = 0.03,
VMUTMAX(2) = 1,
IVARPAIR(2) = 0,
SHEET_NAME(3) = 'sprops',
I1(3) = 1,
I2(3) = 0,
VAR_TYPE(3) = 'K0X',
MINVAL(3) = -1,
MAXVAL(3) = -1,
USE_LOG(3) = .FALSE.,
PMUT(3) = 0.03,
VMUTMAX(3) = 1,
IVARPAIR(3) = 0,
SHEET_NAME(4) = 'sprops',
I1(4) = 1,
I2(4) = 0,
VAR_TYPE(4) = 'NKX',
MINVAL(4) = -1,
MAXVAL(4) = -1,
USE_LOG(4) = .FALSE.,
PMUT(4) = 0.03,
VMUTMAX(4) = 1,
IVARPAIR(4) = 0,
SHEET_NAME(5) = 'sprops',
I1(5) = 1,
I2(5) = 0,
VAR_TYPE(5) = 'R0',
MINVAL(5) = 2100,
MAXVAL(5) = 2400,
USE_LOG(5) = .FALSE.,
PMUT(5) = 0.03,
VMUTMAX(5) = 1,
IVARPAIR(5) = 0,
SHEET_NAME(6) = 'sprops',
I1(6) = 1,
I2(6) = 0,
VAR_TYPE(6) = 'NR',
MINVAL(6) = -0.05,
MAXVAL(6) = 0,
USE_LOG(6) = .FALSE.,
PMUT(6) = 0.03,
VMUTMAX(6) = 1,
IVARPAIR(6) = 0,
SHEET_NAME(7) = 'sprops',
I1(7) = 1,
I2(7) = 0,
VAR_TYPE(7) = 'C0',
MINVAL(7) = 1000,
MAXVAL(7) = 2000,
USE_LOG(7) = .FALSE.,
PMUT(7) = 0.03,
VMUTMAX(7) = 1,
IVARPAIR(7) = 0,
SHEET_NAME(8) = 'sprops',
I1(8) = 1,
I2(8) = 0,
```

```
VAR_TYPE(8) = 'NC',
MINVAL(8) = 0,
MAXVAL(8) = 0.05,
USE_LOG(8) = .FALSE.,
PMUT(8) = 0.03,
VMUTMAX(8) = 1,
IVARPAIR(8) = 0,
SHEET_NAME(9) = 'sprops',
I1(9) = 1,
I2(9) = 0,
VAR_TYPE(9) = 'EMIS',
MINVAL(9) = 0.8,
MAXVAL(9) = 0.95,
USE_LOG(9) = .FALSE.,
PMUT(9) = 0.03,
VMUTMAX(9) = 1,
IVARPAIR(9) = 0,
SHEET_NAME(10) = 'sprops',
I1(10) = 1,
I2(10) = 0,
VAR_TYPE(10) = 'PERMZ',
MINVAL(10) = 1E-18,
MAXVAL(10) = 0.000000000000001,
USE_LOG(10) = .FALSE.,
PMUT(10) = 0.03,
VMUTMAX(10) = 1,
IVARPAIR(10) = 0,
SHEET_NAME(11) = 'sprops',
I1(11) = 1,
I2(11) = 0,
VAR_TYPE(11) = 'PERMX',
MINVAL(11) = -1,
MAXVAL(11) = -1,
USE_LOG(11) = .FALSE.,
PMUT(11) = 0.03,
VMUTMAX(11) = 1,
IVARPAIR(11) = 0,
SHEET_NAME(12) = 'sprops',
I1(12) = 1,
I2(12) = 0,
VAR_TYPE(12) = 'RS0',
MINVAL(12) = 2600,
MAXVAL(12) = 3000,
USE_LOG(12) = .FALSE.,
PMUT(12) = 0.03,
VMUTMAX(12) = 1,
IVARPAIR(12) = 0,
SHEET_NAME(13) = 'sprops',
I1(13) = 1,
I2(13) = 0,
VAR_TYPE(13) = 'PORE_DIAMETER',
MINVAL(13) = 0.00000000001,
MAXVAL(13) = 0.0001,
USE_LOG(13) = .FALSE.,
PMUT(13) = 0.03,
VMUTMAX(13) = 1,
IVARPAIR(13) = 0,
SHEET_NAME(14) = 'sprops',
I1(14) = 2,
I2(14) = 1,
VAR_TYPE(14) = 'K0Z',
MINVAL(14) = -0.99,
MAXVAL(14) = -0.95,
USE_LOG(14) = .FALSE.,
PMUT(14) = 0.03,
VMUTMAX(14) = 1,
IVARPAIR(14) = 0,
SHEET_NAME(15) = 'sprops',
I1(15) = 2,
I2(15) = 0,
VAR_TYPE(15) = 'NKZ',
```

MINVAL(15) = -0.05,
MAXVAL(15) = 0,
USE_LOG(15) = .FALSE.,
PMUT(15) = 0.03,
VMUTMAX(15) = 1,
IVARPAIR(15) = 0,
SHEET_NAME(16) = 'sprops',
I1(16) = 2,
I2(16) = 0,
VAR_TYPE(16) = 'K0X',
MINVAL(16) = -1,
MAXVAL(16) = -1,
USE_LOG(16) = .FALSE.,
PMUT(16) = 0.03,
VMUTMAX(16) = 1,
IVARPAIR(16) = 0,
SHEET_NAME(17) = 'sprops',
I1(17) = 2,
I2(17) = 0,
VAR_TYPE(17) = 'NKX',
MINVAL(17) = -1,
MAXVAL(17) = -1,
USE_LOG(17) = .FALSE.,
PMUT(17) = 0.03,
VMUTMAX(17) = 1,
IVARPAIR(17) = 0,
SHEET_NAME(18) = 'sprops',
I1(18) = 2,
I2(18) = 1,
VAR_TYPE(18) = 'R0',
MINVAL(18) = -0.99,
MAXVAL(18) = -0.95,
USE_LOG(18) = .FALSE.,
PMUT(18) = 0.03,
VMUTMAX(18) = 1,
IVARPAIR(18) = 0,
SHEET_NAME(19) = 'sprops',
I1(19) = 2,
I2(19) = 0,
VAR_TYPE(19) = 'NR',
MINVAL(19) = -0.05,
MAXVAL(19) = 0,
USE_LOG(19) = .FALSE.,
PMUT(19) = 0.03,
VMUTMAX(19) = 1,
IVARPAIR(19) = 0,
SHEET_NAME(20) = 'sprops',
I1(20) = 2,
I2(20) = 1,
VAR_TYPE(20) = 'C0',
MINVAL(20) = -1.1,
MAXVAL(20) = -1.01,
USE_LOG(20) = .FALSE.,
PMUT(20) = 0.03,
VMUTMAX(20) = 1,
IVARPAIR(20) = 0,
SHEET_NAME(21) = 'sprops',
I1(21) = 2,
I2(21) = 0,
VAR_TYPE(21) = 'NC',
MINVAL(21) = 0,
MAXVAL(21) = 0.05,
USE_LOG(21) = .FALSE.,
PMUT(21) = 0.03,
VMUTMAX(21) = 1,
IVARPAIR(21) = 0,
SHEET_NAME(22) = 'sprops',
I1(22) = 2,
I2(22) = 0,
VAR_TYPE(22) = 'EMIS',
MINVAL(22) = 0.8,

```
MAXVAL(22) = 0.95,
USE_LOG(22) = .FALSE.,
PMUT(22) = 0.03,
VMUTMAX(22) = 1,
IVARPAIR(22) = 0,
SHEET_NAME(23) = 'sprops',
I1(23) = 2,
I2(23) = 1,
VAR_TYPE(23) = 'PERMZ',
MINVAL(23) = -10000,
MAXVAL(23) = -1,
USE_LOG(23) = .FALSE.,
PMUT(23) = 0.03,
VMUTMAX(23) = 1,
IVARPAIR(23) = 0,
SHEET_NAME(24) = 'sprops',
I1(24) = 2,
I2(24) = 0,
VAR_TYPE(24) = 'PERMX',
MINVAL(24) = -1,
MAXVAL(24) = -1,
USE_LOG(24) = .FALSE.,
PMUT(24) = 0.03,
VMUTMAX(24) = 1,
IVARPAIR(24) = 0,
SHEET_NAME(25) = 'sprops',
I1(25) = 2,
I2(25) = 1,
VAR_TYPE(25) = 'RS0',
MINVAL(25) = -0.99,
MAXVAL(25) = -0.95,
USE_LOG(25) = .FALSE.,
PMUT(25) = 0.03,
VMUTMAX(25) = 1,
IVARPAIR(25) = 0,
SHEET_NAME(26) = 'sprops',
I1(26) = 2,
I2(26) = 1,
VAR_TYPE(26) = 'PORE_DIAMETER',
MINVAL(26) = -1.05,
MAXVAL(26) = -1,
USE_LOG(26) = .FALSE.,
PMUT(26) = 0.03,
VMUTMAX(26) = 1,
IVARPAIR(26) = 0,
SHEET_NAME(27) = 'sprops',
I1(27) = 3,
I2(27) = 2,
VAR_TYPE(27) = 'K0Z',
MINVAL(27) = -0.99,
MAXVAL(27) = -0.95,
USE_LOG(27) = .FALSE.,
PMUT(27) = 0.03,
VMUTMAX(27) = 1,
IVARPAIR(27) = 0,
SHEET_NAME(28) = 'sprops',
I1(28) = 3,
I2(28) = 0,
VAR_TYPE(28) = 'NKZ',
MINVAL(28) = -0.05,
MAXVAL(28) = 0,
USE_LOG(28) = .FALSE.,
PMUT(28) = 0.03,
VMUTMAX(28) = 1,
IVARPAIR(28) = 0,
SHEET_NAME(29) = 'sprops',
I1(29) = 3,
I2(29) = 0,
VAR_TYPE(29) = 'K0X',
MINVAL(29) = -1,
MAXVAL(29) = -1,
```

```
USE_LOG(29) = .FALSE.,
PMUT(29) = 0.03,
VMUTMAX(29) = 1,
IVARPAIR(29) = 0,
SHEET_NAME(30) = 'sprops',
I1(30) = 3,
I2(30) = 0,
VAR_TYPE(30) = 'NKX',
MINVAL(30) = -1,
MAXVAL(30) = -1,
USE_LOG(30) = .FALSE.,
PMUT(30) = 0.03,
VMUTMAX(30) = 1,
IVARPAIR(30) = 0,
SHEET_NAME(31) = 'sprops',
I1(31) = 3,
I2(31) = 2,
VAR_TYPE(31) = 'R0',
MINVAL(31) = -0.99,
MAXVAL(31) = -0.95,
USE_LOG(31) = .FALSE.,
PMUT(31) = 0.03,
VMUTMAX(31) = 1,
IVARPAIR(31) = 0,
SHEET_NAME(32) = 'sprops',
I1(32) = 3,
I2(32) = 0,
VAR_TYPE(32) = 'NR',
MINVAL(32) = -0.05,
MAXVAL(32) = 0,
USE_LOG(32) = .FALSE.,
PMUT(32) = 0.03,
VMUTMAX(32) = 1,
IVARPAIR(32) = 0,
SHEET_NAME(33) = 'sprops',
I1(33) = 3,
I2(33) = 2,
VAR_TYPE(33) = 'C0',
MINVAL(33) = -1.1,
MAXVAL(33) = -1.01,
USE_LOG(33) = .FALSE.,
PMUT(33) = 0.03,
VMUTMAX(33) = 1,
IVARPAIR(33) = 0,
SHEET_NAME(34) = 'sprops',
I1(34) = 3,
I2(34) = 0,
VAR_TYPE(34) = 'NC',
MINVAL(34) = 0,
MAXVAL(34) = 0.05,
USE_LOG(34) = .FALSE.,
PMUT(34) = 0.03,
VMUTMAX(34) = 1,
IVARPAIR(34) = 0,
SHEET_NAME(35) = 'sprops',
I1(35) = 3,
I2(35) = 0,
VAR_TYPE(35) = 'EMIS',
MINVAL(35) = 0.8,
MAXVAL(35) = 0.95,
USE_LOG(35) = .FALSE.,
PMUT(35) = 0.03,
VMUTMAX(35) = 1,
IVARPAIR(35) = 0,
SHEET_NAME(36) = 'sprops',
I1(36) = 3,
I2(36) = 1,
VAR_TYPE(36) = 'PERMZ',
MINVAL(36) = -10000,
MAXVAL(36) = -1,
USE_LOG(36) = .FALSE.,
```

PMUT(36) = 0.03,
VMUTMAX(36) = 1,
IVARPAIR(36) = 0,
SHEET_NAME(37) = 'sprops',
I1(37) = 3,
I2(37) = 0,
VAR_TYPE(37) = 'PERMX',
MINVAL(37) = -1,
MAXVAL(37) = -1,
USE_LOG(37) = .FALSE.,
PMUT(37) = 0.03,
VMUTMAX(37) = 1,
IVARPAIR(37) = 0,
SHEET_NAME(38) = 'sprops',
I1(38) = 3,
I2(38) = 2,
VAR_TYPE(38) = 'RS0',
MINVAL(38) = -0.99,
MAXVAL(38) = -0.95,
USE_LOG(38) = .FALSE.,
PMUT(38) = 0.03,
VMUTMAX(38) = 1,
IVARPAIR(38) = 0,
SHEET_NAME(39) = 'sprops',
I1(39) = 3,
I2(39) = 2,
VAR_TYPE(39) = 'PORE_DIAMETER',
MINVAL(39) = -1.05,
MAXVAL(39) = -1,
USE_LOG(39) = .FALSE.,
PMUT(39) = 0.03,
VMUTMAX(39) = 1,
IVARPAIR(39) = 0,
SHEET_NAME(40) = 'rxns',
I1(40) = 1,
I2(40) = 0,
VAR_TYPE(40) = 'Z',
MINVAL(40) = 1,
MAXVAL(40) = 9,
USE_LOG(40) = .TRUE.,
PMUT(40) = 0.03,
VMUTMAX(40) = 1,
IVARPAIR(40) = 0,
SHEET_NAME(41) = 'rxns',
I1(41) = 1,
I2(41) = 0,
VAR_TYPE(41) = 'E',
MINVAL(41) = 20,
MAXVAL(41) = 150,
USE_LOG(41) = .FALSE.,
PMUT(41) = 0.03,
VMUTMAX(41) = 1,
IVARPAIR(41) = 0,
SHEET_NAME(42) = 'rxns',
I1(42) = 1,
I2(42) = 0,
VAR_TYPE(42) = 'DHV',
MINVAL(42) = 2,
MAXVAL(42) = 7,
USE_LOG(42) = .TRUE.,
PMUT(42) = 0.03,
VMUTMAX(42) = 1,
IVARPAIR(42) = 0,
SHEET_NAME(43) = 'rxns',
I1(43) = 1,
I2(43) = 0,
VAR_TYPE(43) = 'ORDER',
MINVAL(43) = 0.9,
MAXVAL(43) = 1.1,
USE_LOG(43) = .FALSE.,
PMUT(43) = 0.03,

```
VMUTMAX(43) = 1,
IVARPAIR(43) = 0,
SHEET_NAME(44) = 'rxns',
I1(44) = 2,
I2(44) = 0,
VAR_TYPE(44) = 'Z',
MINVAL(44) = 7,
MAXVAL(44) = 8,
USE_LOG(44) = .TRUE.,
PMUT(44) = 0.03,
VMUTMAX(44) = 1,
IVARPAIR(44) = 0,
SHEET_NAME(45) = 'rxns',
I1(45) = 2,
I2(45) = 0,
VAR_TYPE(45) = 'E',
MINVAL(45) = 100,
MAXVAL(45) = 180,
USE_LOG(45) = .FALSE.,
PMUT(45) = 0.03,
VMUTMAX(45) = 1,
IVARPAIR(45) = 0,
SHEET_NAME(46) = 'rxns',
I1(46) = 2,
I2(46) = 0,
VAR_TYPE(46) = 'DHV',
MINVAL(46) = 5,
MAXVAL(46) = 8,
USE_LOG(46) = .TRUE.,
PMUT(46) = 0.03,
VMUTMAX(46) = 1,
IVARPAIR(46) = 0,
SHEET_NAME(47) = 'rxns',
I1(47) = 2,
I2(47) = 0,
VAR_TYPE(47) = 'ORDER',
MINVAL(47) = 0.7,
MAXVAL(47) = 1.3,
USE_LOG(47) = .FALSE.,
PMUT(47) = 0.03,
VMUTMAX(47) = 1,
IVARPAIR(47) = 0,
 /
```